

**School of Earth and Planetary Sciences
Applied Geology**

**Short Wave Infrared Alteration Maps of a Volcanogenic Massive
Sulphide Deposit: A case study of the Bentley Deposit, Western
Australia**

Robert Connelly

**This thesis is presented for the Degree of
Master of Philosophy (Geology)
of
Curtin University**

August 2020

Declaration

To the best of my knowledge and belief this thesis contains no material previously published by any other person except where due acknowledgment has been made.

This thesis contains no material which has been accepted for the award of any other degree or diploma in any university.

(Include where applicable)

Human Ethics (For projects involving human participants/tissue, etc) The research presented and reported in this thesis was conducted in accordance with the National Health and Medical Research Council National Statement on Ethical Conduct in Human Research (2007) – updated March 2014. The proposed research study received human research ethics approval from the Curtin University Human Research Ethics Committee (EC00262), Approval Number #.....

or

Animal Ethics (For projects involving animal use) The research presented and reported in this thesis was conducted in compliance with the National Health and Medical Research Council Australian code for the care and use of animals for scientific purposes 8th edition (2013). The proposed research study received animal ethics approval from the Curtin University Animal Ethics Committee, Approval Number #.....

Signature: ... 

Date: 18/8/2020

To the best of my knowledge and belief, this thesis contains no material previously published by any other person except where due acknowledgement has been made. This thesis contains no material which has been accepted for the award of any other degree or diploma in any university.

Robert Connelly

Date 18/08/2020

Abstract

The Bentley Volcanogenic massive sulphide (VMS) Zn–Cu deposit is located within the Teutonic Bore mining camp in the Gindalbie Terrane, Eastern Goldfields Superterrane, Western Australia. Massive sulphides formed within felsic volcanoclastic and sulphidic shale horizons with an andesite hangingwall and rhyolitic footwall. Dolerites cut the mineralisation to form multiple ore bodies. A significant chalcopyrite stringer is present within the footwall. The deposit is interpreted to have formed below the seafloor, based on an absence of sulphide chimney breccias and the presence of sulphides within consolidated volcanoclastics and shales.

Isotopic dating of monazite and zircon from the Bentley footwall yield an age of 2729 ± 24 Ma for the rhyolite, which is older than other published ages for the Gindalbie Terrane. Further work is needed to explain this discrepancy. The ages of monazite grains associated with hydrothermal alteration are constrained to 2730–2200 Ma.

Shortwave Infrared Spectroscopy (SWIR) enables rapid identification of fine-grained alteration assemblages and their compositional variation, so portable SWIR spectrometers provide a powerful tool for mineral exploration. At the Bentley deposit, large volumes of SWIR data were collected that were not used in a substantial or meaningful way prior to this study. The historic data were collected primarily from diamond drill core. These data were augmented by spectral data from rock samples from the mine and additional analyses of newer diamond drill core. The final dataset consists of 5600 analyses and was used to investigate the hydrothermal alteration of the rhyolite footwall.

The SWIR data analysis focussed on two minerals that are commonly associated with alteration within a typical VMS footwall: (1) Chlorite was investigated using wavelengths around 2250 nm; (2) White mica was investigated using wavelengths around 2200 nm. Data from these wavelengths were interpreted to provide information on the abundance and compositions of the minerals. SWIR results indicate a broad shortening of white mica wavelength with increased proximity to mineralization which indicates a general reduction in white mica silica content. The chlorite wavelengths lengthened with increasing ore proximity, indicating chlorite is enriched in Fe near to mineralization with Mg-rich chlorite present further away. The relative abundance of chlorite to white mica indicates that chlorite is dominant in areas that were directly below the deposit at formation. These higher ratios show strong correlation with a known zone of economic stringer sulphide mineralization and likely indicate the location of major hydrothermal feeder zones.

A three-dimensional model was created using the Leapfrog geological software, and cross sections were created and interpreted. The cross sections were used to define five alteration zones. The temperature and redox state of mineralising fluids were estimated, based on the characteristics of the alteration assemblages and comparisons with the literature. The orientation and other characteristics of faults associated with mineralisation were established from the alteration and geometry of mineralisation. Conceptual models were derived that can be used to determine potential vectors to mineralization at the regional and mine scale. The results of the study were integrated to produce a model that describes the evolution of the Bentley VMS host lithologies, structural controls, and sulphide mineralisation. The results provide a framework for the interpretation of SWIR data associated with VMS deposits in the Gindalbie Terrane and elsewhere.

Acknowledgements

I would like to thank my supervisors, Dr Kirsten Rempel and particularly Dr Katy Evans, both of Curtin University for their guidance, support and patience to allow me to complete this project. I genuinely appreciate the opportunity and will never be able to thank them enough.

Thank you to Dr Chris Kirkland for undertaking the LA-ICP-MS test work.

Thank you to Graham Sweetman, formerly the Chief Geologist at Jaguar Mine, for his support, time, and resources during sampling and data collection.

Table of Contents

Abstract.....	4
Acknowledgements	7
Table of Contents.....	8
List of Figures	11
List of Tables.....	14
1. Introduction	15
1.1 Location and Access.....	18
1.2 Objectives.....	18
1.3 Methodology	19
1.3.1 Short Wave Infrared	19
1.3.2 Modelling.....	22
1.3.3 Laser Ablation–Inductively Coupled Plasma–Mass Spectrometry	22
1.3.4 U–Pb–Th Geochronology	23
1.3.5 Scanning Electron Microscope Energy Dispersive Spectrometer (SEM–EDS)	25
1.3.6 Transmitted Light Spectroscopy	26
2. Geology of the Bentley Deposit	27
2.1 Regional Geology	27
2.2 Local Geology of the Bentley Deposit	30
2.2.1 Footwall Rhyolite	31
2.2.2 Host Lithologies.....	33
2.2.3. Mafic Intrusive Rocks	34
2.3. Bentley VMS Mineralisation and Classification	34
3. Petrography	39
3.1 Objectives.....	39
3.2 Petrographic Results	39
3.3 Interpretation	43
3.3.1 Least–altered rocks	43
3.3.2 White mica–rich rocks	44
3.3.3 Chlorite–rich rocks	44
4. SWIR Data	46
4.1 Objectives of SWIR data processing.....	46
4.2 Results	46
4.3 Interpretation	52

4.3.1 White Mica Wavelength.....	52
4.3.2 Chlorite Wavelengths	53
4.3.3 Chlorite/White Mica Hull Quotient Depth Ratio	53
5. Ages of Igneous and Hydrothermal Activity	54
5.1 Objectives.....	54
5.2 Results	55
5.2.1. Zircon	55
5.3 Interpretation	56
6. Discussion.....	60
6.1 Model Cross Sections based on SWIR data	60
6.1.1 Modelled Alteration on 4145 RL	61
6.1.2 Modelled Alteration on 3870 RL and 3750 RL	64
6.1.3 Modelled Alteration Line of Lode	67
6.2 Alteration Summary	71
6.2.1 Alteration Zone 1	71
6.2.2 Alteration Zone 2.....	73
6.2.3 Alteration Zone 3.....	74
6.2.4 Alteration Zone 4.....	76
6.2.5 Alteration Zone 5.....	77
6.2.6 Further Work	78
6.3 Structural Control of Fluid Flow.....	79
6.4 A Genetic Model for the Bentley Deposit	83
6.4.1 Footwall Rhyolite.....	84
6.4.2 Normal Faulting.....	86
6.4.3 First Volcaniclastics.....	87
6.4.4 First Black Shale	87
6.4.5 Second Volcaniclastic	87
6.4.6 Second Black Shale	87
6.4.7 Andesite	87
6.4.8 Mineralisation	88
6.4.9 Intrusion of Dolerites	88
7. Conclusions	89
8. List of References	91
Appendix 1. Petrographic Descriptions.....	97
Appendix 2. SEM–EDS Observations	104
Appendix 3. Laser Ablation Inductively Coupled Plasma Mass Spectrometry (LA–ICPMS)109	

Appendix 4. Rock Descriptions and Location of Samples for Figure 5.5..... 111
Appendix 5. Short Wave Infrared Data Sample 113

List of Figures

Figure 1.1. A schematic composite section through a VMS alteration system in the Bathurst mining camp. (Modified from Galley et al, 2007).	16
Figure 1.2. Location of the Bentley VMS deposit, Teutonic Bore, and Jaguar (Stevenson, 2015).....	18
Figure 1.3. Depiction of the hull correction technique (Pontual, 2005).	21
Figure 1.4. A U–Pb concordia diagram,	24
Figure 1.5. Backscattered electron (BSE) zircon image.	25
Figure 2.1. Geologic map of the Teutonic Bore volcanic complex, Yilgarn Craton, Western Australia, showing the locations of the Teutonic Bore, Jaguar, and Bentley VMS deposits (modified from Chen et al, 2015).	28
Figure 2.2. Geological map showing the location of the Bentley VMS deposit within the Gindalbie Terrane (Australian Map Grid Zone 51) (modified from Krapež and Barley 2008).	27
Figure 2.3. Pseudo–breccias within chlorite–altered footwall rhyolite (14BUDD033 70.5–75.05m).....	32
Figure 2.4. Quartz–sericite altered footwall rhyolite (14BUDD005 244.75–248.85m)	32
Figure 2.5. Relatively unaltered rhyolite with euhedral feldspar and quartz phenocrysts. (15TRDD013 740.3– 744.8m).....	31
Figure 2.6. Chalcopyrite–pyrite stringer mineralisation within intensely chlorite–altered rhyolite in the Azure Lens (13BUDD077 58.3–62.7m).....	33
Figure 2.7. The Brooklands ore lens on the 4000 RL (relative level), looking north.	35
Figure 2.8. The Arnage ore lens on the 3940RL, looking south.	36
Figure 2.9. The Azure orebody on the 4140 RL access drive.	37
Figure 2.10. The Mulsanne lens. Looking north on the 4100 RL.	38
Figure 3.1. Sample A8: Subhedral quartz, sanidine and plagioclase phenocrysts in a quartz–sericite matrix. (XPL)	40
Figure 3.2. Sample A9: Twinned subhedral feldspar (sanidine) crystals with chlorite in a quartz–sericite matrix (XPL).....	40
Figure 3.3. Sample A4: Relict feldspars within sericite alteration in a carbonate–bearing quartz–sericite groundmass. (XPL).	41

Figure 3.4. Sample A7: Fine bright sericite veins define a metamorphic foliation.	41
Figure 3.5. Sample A5: Fine carbonate veins (white) within chlorite-rich groundmass (XPL).	42
Figure 3.6. Sample A6: Chlorite within a quartz matrix. (PPL).	42
Figure 3.7. <i>Thin Section Sample Points looking southwest.</i>	43
Figure 4.1. Histogram of Al-OH white mica wavelengths (2180–2228 nm) for chlorite and white mica– dominant samples, showing the diagnostic wavelength ranges for mineral types (Pontual, 2005)...	48
Figure 4.2. Oblique section looking southwest displaying 2200 nm (white-mica wavelength) SWIR spectra heat range in the footwall rhyolite with massive sulphide lenses (red) and Azure stringer lens (yellow). .	48
Figure 4.3. Histogram of Fe-OH chlorite wavelengths (2240–2265 nm) for chlorite and white mica–dominant samples, showing the diagnostic wavelength ranges for chlorite compositions (Pontual, 2005).	50
Figure 4.4. Oblique section looking southwest displaying 2250 nm (Fe– chlorite wavelength) SWIR spectra range in the footwall rhyolite with massive sulphide lenses (red) and Azure stringer lens (yellow). .	51
Figure 4.5. Histogram of hull quotient depth ratios, representing the ratio of chlorite to white mica.	
Figure 4.6. Oblique Oblique section looking southwest displaying 2250/2200 hull quotient depth ratio in the footwall rhyolite with massive sulphide lenses (red) and Azure stringer lens (yellow).	53
Figure 5.1. SEM–EDS Electron Image of zircon (A9).	54
Figure 5.2. SEM–EDS Electron Image of skeletal monazite (Sample A5).	55
Figure 5.3. U–Pb concordia diagram of zircon analyses..	56
Figure 5.4. Composite sequence stratigraphy of the Gindalbie–Kurnalpi terranes (modified from Krapez and Pickard, 2016).	57
Figure 5.5. Terranes of the Eastern Goldfields Superterrane, and sample locations (modified from Kositcin et al, 2008), showing the Teutonic Bore data (Belford et al, 2015) and the new data from this study for Bentley.	58
Figure 6.1. Three dimensional visualisation of the locations of the cross sections at 4145 RL, 3870 RL and 3750 RL and along the line of lode. Looking northwest. The main massive sulphide lens (Arnage) is shown in red.	60
Figure 6.2. Plan section of alteration on 4145 RL. Black squares indicate drill–hole pierce points. (A) White mica absorption. (B) Chlorite absorption. (C) Chlorite:white mica ratios.	62

Figure 6.3. Plan Section of alteration on 3870 RL. Black squares indicate drill–hole pierce points. (A) White mica absorption. (B) Chlorite absorption. C) Chlorite:white mica ratios. 65

Figure 6.4. Plan Section of alteration on 3750 RL. Black squares indicate drill–hole pierce points. (A) White mica absorption. (B) Chlorite absorption. C) Chlorite:white mica ratios. 66

Figure 6.5. Plan Section of alteration on the line of lode. Black squares indicate drill–hole pierce points. (A) White mica absorption. (B) Chlorite absorption. C) Chlorite:white mica ratios..... 69

Figure 6.6. Model of alteration at the Bentley Deposit 4145 rL (cross–section)..... 78

Figure 6.7. Conceptual model of the propagation of a normal fault to the surface (in basalt). (modified from Martel and Langley, 2006) 80

Figure 6.8. Structural map of the northern fork of the Hopena Fault showing the approximate width of the Bentley deposit. Modified from Kaven and Martel (2007). 81

Figure 6.9. Cross section of the Bentley deposit cross–section looking east. 82

Figure 6.10. Alteration zones in plan section at the Bentley deposit on 4145 RL, with interpreted fault structures. 83

Figure 6.11. Conceptual model of the formation of the Bentley Volcanogenic Massive Sulphide deposit (4145 RL). 85

Figure 6.12. Variable grained volcanoclastics (fine grained within coarse grained) interpreted to have fractured pre-mineralization. Diamond drill–hole BUDD078 @ 61.1m.. 86

List of Tables

Table 1.1. Short Wave Infrared Detection Bands, after Pontual (2011).....	20
Table 3.1. Details of samples selected for petrography.....	39

1. Introduction

Volcanogenic massive sulphide (VMS) deposits form at or below the ocean floor from metal-enriched fluids formed from seawater modified through chemical interaction with footwall rock and a variable contribution from magmatic fluids (Galley et al, 2007; Shanks and Thurston, 2012). They are commonly characterised by well-developed hydrothermal alteration zones that have been used in mineral exploration targeting (e.g., Hutchison, 1972; Solomon, 1976; Franklin et al, 1981; Large, 1992; Barley, 1998; Franklin et al, 2005; Gifkins et al, 2005; Galley et al, 2007; Huston et al, 2010). However, the intensity and extent of the alteration zones vary as a function of the deposit morphology; alteration can form relatively narrow pipes or laterally extensive stratabound zones. The alteration mineralogy depends on the composition of the host rock and ore fluids, so the alteration patterns vary subtly among deposits. The alteration zones present a large exploration target, but are difficult to use as a vector towards the ore unless the details of mineralogical or chemical zonation are recognised and understood.

Volcanogenic massive sulphide deposits consist of one or more of three types of ore zone, each with its own characteristic alteration: stratiform lenses of massive sulphide deposited on the seafloor; stockwork feeder zones; and stratabound replacement zones below the seafloor (Large, 1992). Intense hydrothermal alteration of the footwall below a massive sulphide lens (Figure 1.1) is common and typically consists of zones of albite, sericite, chlorite, carbonate, and quartz, although not all zones are present at all deposits (Barley, 1998; Gifkins et al, 2005; Relvas and Barriga, 2006; Shanks and Thurston, 2012). Commonly, mineralised feeder zones below massive sulphide lenses are surrounded by pipes of extensively altered rock; the alteration is caused by hydrothermal ore fluids that upwell through the feeder pathway, and comprises a siliceous core with concentric zones of proximal chlorite grading to distal sericite, with carbonates and/or albite (Sangster, 1972; Large, 1992) (Figure 1.1). However, it is estimated that around 50% of VMS deposits do not have footwall alteration pipes, but are instead underlain by stratabound or semi-conformable alteration zones focussed on permeable strata; these zones may extend for several kilometres horizontally and several hundred metres vertically below the stratabound ore (Gifkins et al, 2005; Gibson et al, 2007). The alteration mineralogy of the stratabound zones is similar to that of the pipe-style zones, and includes chlorite, quartz, sericite, sulphides, and minor carbonates. Hangingwall alteration may also be present, particularly if the hangingwall was emplaced prior to mineralisation.

Despite the variety in possible alteration assemblages, alteration zones at VMS deposits are dominated by fine-grained white mica (sericite) and chlorite phyllosilicates (Jones et al, 2005;

Shanks and Thurston, 2012; Laakso et al, 2016). The composition of white mica has been investigated at a number of massive sulphides–related hydrothermal systems, although few studies were of a sufficient scale to fully evaluate its usefulness as an exploration tool.

Chlorite is a diagnostic mineral that commonly occurs as veins or bands associated with chalcopyrite mineralisation (Large, 1992). Chlorite zones are typically dominated by chlorite (>50 wt.% and commonly >80 wt.%), with subordinate amounts of quartz, pyrite, and sericite, with or without carbonate (Gifkins et al, 2005). At the Bathurst mining camp, Canada, chlorite composition varies systematically from Fe–rich chlorite at the core of the feeder zone to Mg–rich chlorite near the outer sericite zone (Galley et al, 2007; Figure 1.1). However, the reverse trend has also been observed (e.g., at the Hellyer deposit, Tasmania: Large et al, 1998). Other workers have suggested that zones of Fe–rich chlorite are a product of interaction between undiluted magmatic fluid and the host rocks in feeder zones isolated from seawater, and that zones of Mg–chlorite record entrainment of seawater into the feeder zone (Shanks and Thurston, 2012).

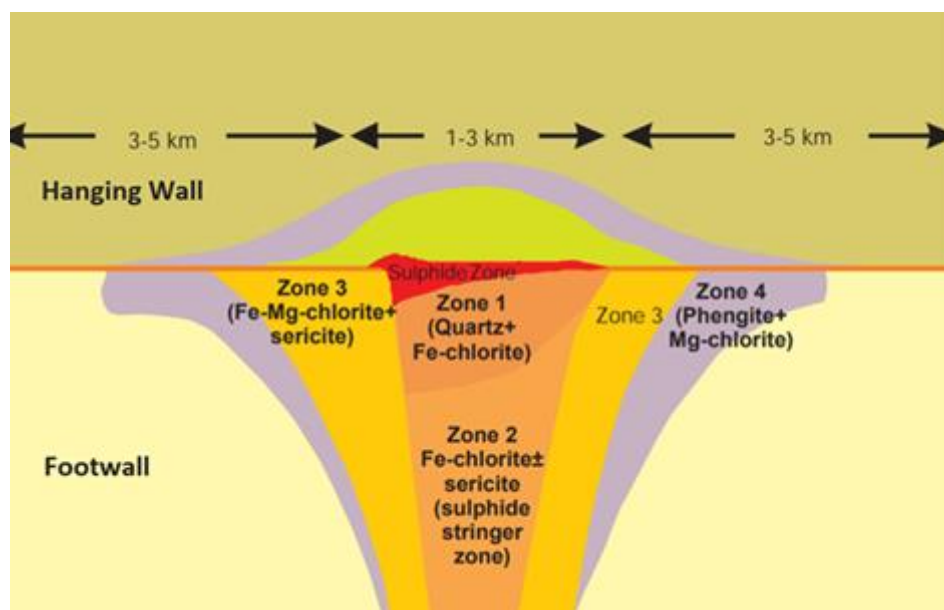


Figure 1.1. A schematic composite section through a VMS alteration system in the Bathurst mining camp. This example exemplifies proximal VMS alteration metamorphosed to greenschist facies mineral assemblages. (Modified from Galley et al, 2007).

Subtle mineralogical changes within VMS alteration halos are difficult to recognise in the field, but handheld shortwave infrared spectroscopy (SWIR) scanners can be used to identify hydrous alteration minerals, obtain compositional information, and determine the relative abundances of minerals (Herrmann et al, 2001; Jones et al, 2005; Laakso, et al, 2016). SWIR

detects inter-molecular vibrations caused by bending and stretching of molecular bonds involving element groups that include OH^- , H_2O , CO_3^{2-} and NH_4^+ (Pontual, 2011).

The hydroxyl anion (OH^-) produces diagnostic absorption features, because its crystallographic position and environment vary significantly among minerals (Pontual, 2011). These features reflect differences in lattice vibrations and absorption between Al–OH, Fe–OH and Mg–OH bonds, and enable differentiation among some of the phyllosilicate minerals that are characteristic of VMS alteration zones. The position of a wavelength within these bands can identify the alteration minerals and differentiate between mineral species such as high-Al white micas (such as paragonite), muscovite, and phengite. Absorption wavelengths associated with Fe–OH and Mg–OH bonds can record the Mg to Fe ratio of chlorite within a VMS feeder zone.

The Bentley VMS deposit is located in the Teutonic Bore VMS camp, Western Australia. Here, the alteration zones are exposed on the mine drives, which provides an opportunity for a detailed study of the composition of the alteration minerals and an assessment of the mineralogical vectors toward mineralised feeder zones. Insights derived from such a study could be used on a broader scale within the camp to find new deposits. Furthermore, techniques developed in the present study could be applied to the large amounts of diamond core and rock chips available from previous drilling programs within and around the camp. The results could be used to target, better define, and potentially expand the current Teutonic Bore and Jaguar mine resources.

Previous applications of SWIR include those of Herrmann et al (2001); Jones et al (2005); Canet et al (2010); Laakso et al (2016); Huang et al (2017); Ross et al (2019). These works have developed and documented SWIR methods and validated SWIR against other methods. However, there are few studies of large datasets. Ross et al (2019) based their work on “tens of thousands” of spectral samples from 22 diamond drill holes and Huang et al (2017), used 520 samples. In the present study, approximately 5600 spectral samples were collected from the footwall of the Bentley deposit from drill-holes and underground mine excavations along approximately 3 kilometres along strike, 1 kilometre down dip and within 200 m of the mineralized horizon. This spatially extensive collection of samples provides a deposit scale view of a VMS hydrothermal system.

The techniques used in this work could be applied to other deposits worldwide. Chlorite and white mica are common minerals in footwall alteration in the majority of VMS deposits, so SWIR methods provide a quick and convenient way to derive new information from old drill core and drill chips and to gain new insights into the alteration at a VMS deposit.

1.1 Location and Access

The Bentley Deposit is located about 65 km north of Leonora by road. Access to the area is via the Goldfields Highway. The Bentley Deposit is about 4 km south of the Jaguar mine (closed) and 6 km south of the historic Teutonic Bore mine; all three mines are owned by the Independence Group (Figure 1.2).

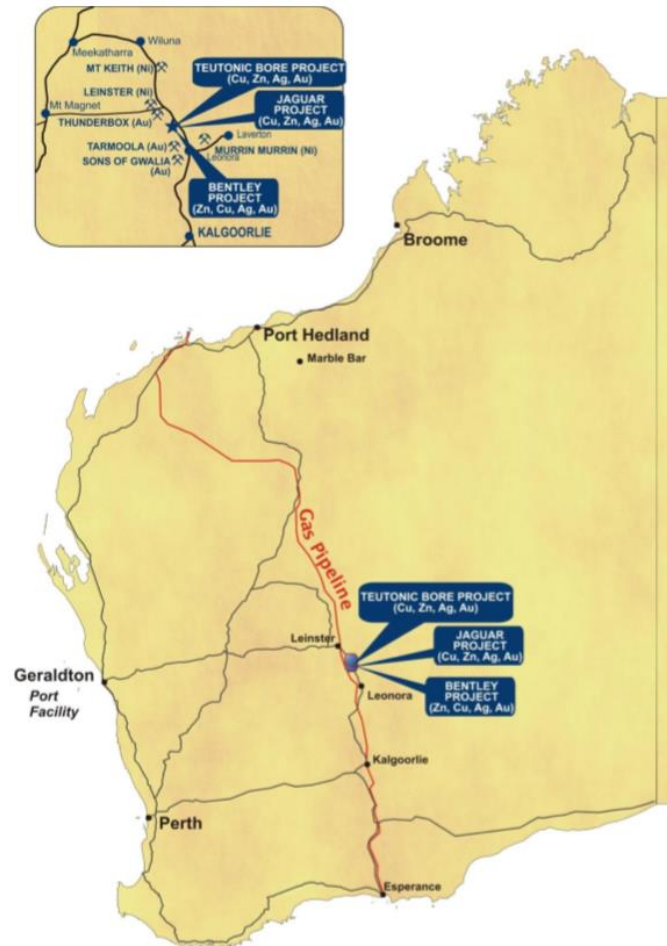


Figure 1.2. Location of the Bentley VMS deposit, Teutonic Bore, and Jaguar (Stevenson, 2015).

1.2 Objectives

The objectives of this thesis are to:

- (1) Create a three-dimensional model of the footwall hydrothermal alteration zone at the Bentley VMS deposit using Short Wave Infrared Spectrometry;
- (2) Derive constraints on the timing of host-rock formation and Laser Ablation Inductively Coupled Plasma Mass Spectrometry (LA-ICPMS) U-Pb analysis; and
- (3) Use insights gained from the large SWIR dataset and model to improve our understanding of the processes that create alteration within VMS footwall zones.

1.3 Methodology

Rhyolites in the footwall were sampled at the Bentley mine between 2013 and 2015. Spectral scanning was conducted on rock chip samples collected at 4 m intervals from the decline and access walls within the footwall rhyolite unit. Chips were washed, placed in chip trays, and allowed to dry for a week in a hot dry area prior to scanning. Footwall rhyolite sections in the production core were scanned at 4 m intervals. Previously collected data from exploration holes that had been scanned at variable spacing (mainly 1–2 m intervals), were also incorporated into the project dataset.

1.3.1 Short Wave Infrared

Shortwave infrared (SWIR) spectrometry was used to determine the spectral absorption features of the alteration assemblages of the Bentley rhyolites. Chip samples and production core were scanned using an ASD TerraSpec 2 spectral scanner. Prior to scanning, the spectrometer was optimised for the target wavelengths, and calibrated with a white reference and secondary standard. White referencing refers to a measurement of a white reference material made of polytetrafluoroethylene (PTFE) and sintered halon that has a near zero level of absorption. The scanning software used the spectrum of this material to calibrate the baseline. The secondary standard was an altered rock sample with a known chlorite and sericite spectral signature (rhyolite half-core sample). Optimisation, white referencing, and standardisation were repeated every hour during analysis, following the methods of Lau and Thapar (2014).

This project focussed on absorption features around 2200 nm (white mica Al–OH) and 2250 nm (chlorite) because these minerals are common in VMS feeder zones, as discussed above. Other characteristic wavelength bands of interest are OH ~1400 nm, H₂O ~1400 nm and ~1900 nm, Al–OH ~2180–2228 nm, Fe–OH ~2240–2265 nm, Mg–OH ~2300–2370 nm, CO₃²⁻ ~2300–2370 nm, 1870 nm, 1990 nm and 2155 nm (Table 1.1) (Pontual, 2011).

Table 1.1. Short Wave Infrared Detection Bands, after Pontual (2011)

	Wavelength
Al–OH	2180–2228 nm
Fe–OH	2240–2265 nm
Mg–OH	~2300–2370 nm
CO ₃ ²⁻	~2300–2370 nm, 1870 nm, 1990 nm, 2155 nm
OH ⁻	~1400 nm, ~1550 nm, ~1750–1850 nm
H ₂ O	~1400 nm and ~1900 nm

The Al–OH bonds within the crystal lattice of white micas absorb light between 2180 and 2228 nm. The Fe–OH and Mg–OH bonds absorb light at 2240–2265 nm and 2320–2360 nm, respectively. The Mg–OH absorption feature overlaps with the absorption features of secondary white mica and carbonate, so its use for chlorite composition determination is limited to cases where latter mineral groups are absent. Biotite also absorbs light at 2250 nm, and this feature can be used to recognise metamorphosed VMS deposits (Shanks and Thurston, 2012). The Fe–OH absorption feature is considered diagnostic of the presence of chlorite, and variations in the position of this feature can be used to estimate the proportions of Mg and Fe. The Fe–OH feature occurs at longer wavelengths when the chlorite is Fe–rich (2257–2265 nm), and at shorter wavelengths when the chlorite is Mg–rich (2240–2249 nm). Intermediate compositions absorb at wavelengths between the two endmembers (2250–2256 nm: Pontual, 2011).

The SWIR spectra were processed using the hull correction technique to facilitate mineral identification. Hull correction facilitates recognition of the spectral signature of minerals, and reveals absorption features that are not visible in the uncorrected spectrum (Pontual, 2005).

Pontual (2011) describes the hull line as a convex baseline that passes through the maximum possible number of points on the measured reflectance spectrum without crossing it (Figure 1.3). The hull quotient is defined as the calculated ratio of the reflectance on the hull line to the reflectance on the measured spectrum at a specified wavelength and is calculated by dividing the raw spectral absorption percentage value by the hull line absorption spectral percentage, and multiplying it by 100. The hull difference is calculated by subtracting the hull line absorption spectral percentage from the raw spectral absorption percentage (Figure 1.3).

The hull line touches the measured spectrum at the first and last data points (for SWIR: 3500 nm and 2500 nm, respectively). Thus, the hull–corrected spectrum has reflectance values of

100% at the beginning and end of the spectrum (Figure 1.3). However, variations in hull correction algorithms and the plotting capabilities of the software mean that the beginning and end points on the corrected spectrum may not plot at 100%.

For this project, the TSG (The Spectral Geologist) Pro software (The Spectral Geologist, 2017) was used to process the data and calculate the absorption of white mica (hqd2200), and chlorite (hqd2250). The ratio of hqd2250 to hqd2200 provides a measure of the relative abundances of chlorite and white micas, and is referred to below as the chlorite:white mica ratio.

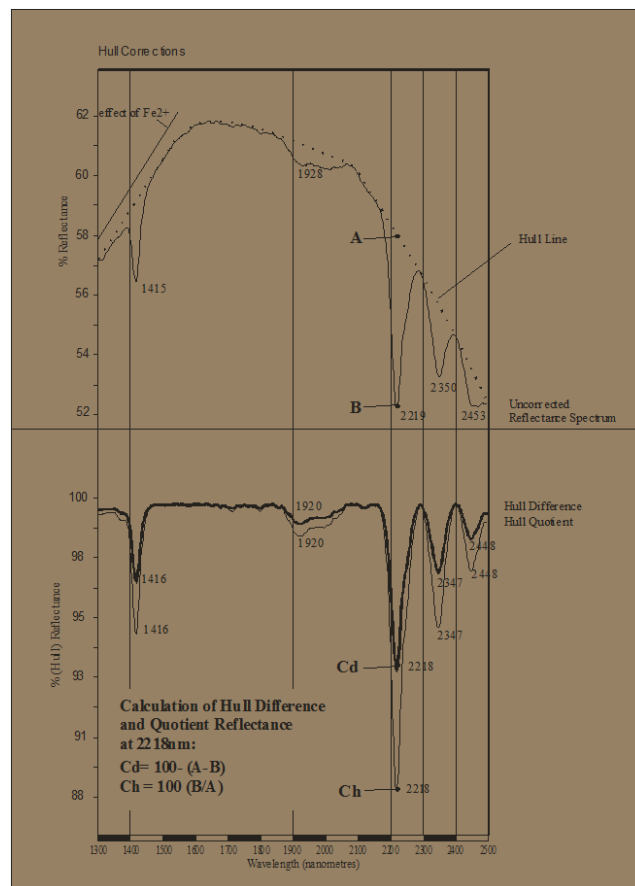


Figure 1.3. Depiction of the hull correction technique (Pontual, 2005).

The TSG Pro software was also used for mineral identification, but the results were used with caution, because some combinations of minerals can lead to spurious results (e.g., sericite, carbonate, and Mg-OH absorb at the same wavelengths).

Any spectra that showed evidence of contamination (e.g., from paint from the mine or hydrocarbons) or were noisy with narrow (<4 nm), weak, random, sharp features were removed from the dataset, following the method of Pontual (2011). Only ~1% of the 5600 data

points were excluded. The majority of these appear to record operator error during collection; inspection of the spectra inspection during collection usually identifies poor reflectance data.

1.3.2 Modelling

The Surpac geological software package (Geovia, 2017) was used to determine the spatial coordinates of the sampling locations. These coordinates were entered into a spreadsheet to create a drill-hole trace of the decline that was used as input into the Leapfrog Mine software (Leapfrog 3D, 1996), in conjunction with existing geological wireframe models of the Bentley mine resource. These models show the limits of economic massive sulphide and stringer mineralisation within the deposit.

1.3.3 Laser Ablation–Inductively Coupled Plasma–Mass Spectrometry

Zircon and monazite grains were identified in two thin sections using a petrographic microscope. The U–Pb isotope ratios were measured by laser ablation–inductively coupled plasma–mass spectrometry (LA–ICPMS) at the John de Laeter Centre, Western Australian School of Mines, Curtin University.

Qualitative mineral mapping of thin sections A5 and A9 was first performed using a TESCAN Integrated Mineral Analyser (TIMA). This instrument combines a high–resolution Field Emission Scanning Electron Microscope (FESEM) with four fully integrated Energy Dispersive Spectroscopy (EDS) detectors. This system enables the location of zircons and monazite to be mapped rapidly by back–scattered electron (BSE) imaging and a liberation mode designed for metallurgical test work.

Selected zircon and monazite grains were ablated using a Resonetics RESOLUTION M-50A-LR system, incorporating a Compex 102 193 nm excimer UV laser, with a 15 µm diameter laser spot, 4 Hz laser repetition rate, and laser energy of about 1.0 J/cm². Isotopic intensities were measured using an Agilent 7700s quadrupole ICP–MS, with high purity Ar as the plasma gas (0.98 L min⁻¹). Following a ten second period of background analysis, samples were spot ablated for 30 s. The sample cell was flushed by ultrahigh purity He (0.68 L min⁻¹) and N (2.8 mL min⁻¹). The mass spectra were reduced using Iolite and in–house Excel macros. The LA–ICP–MS U–Pb data are provided in Appendix 3.

1.3.4 U–Pb–Th Geochronology

Zircon and monazite incorporate radioactive U, Th and Pb. These elements are used as the benchmark for dating geological materials because the decay constants for ^{235}U to ^{207}Pb , ^{238}U to ^{206}Pb , and ^{232}Th to ^{208}Pb are well known (Kirkland and Wingate, 2012). Over a known time period the concentrations of the radioactive parent isotopes, U and Th, decrease and the concentration of the daughter Pb isotopes increase. Therefore, the ratios of radioactive U and Th and their respective daughter Pb isotopes in minerals such as zircon and monazite can be used to estimate their age (Blatt et al, 2006).

Three radioactive decay chains can be used independently to determine age. However, they rarely give the same result (Blatt et al, 2006). Uranium can be mobile during hydrothermal alteration or weathering. Radiogenic Pb can be lost by diffusion through a crystallized but still hot rock and $^{207}\text{Pb}/^{204}\text{Pb}$ ages are generally older than $^{206}\text{Pb}/^{204}\text{Pb}$ isochron ages because ^{238}U is naturally more abundant than ^{235}U . Furthermore, mineral grains may incorporate ^{206}Pb , ^{207}Pb and ^{208}Pb during crystallization. This “initial” Pb must be taken into account because it is not produced by radioactive decay. The initial amount of radiogenic Pb is estimated from the amount of non–radiogenic ^{204}Pb . The higher the amount of ^{204}Pb present the higher the amount of initial radiogenic Pb. By applying a general model for terrestrial Pb evolution to estimate the $^{206}\text{Pb}/^{204}\text{Pb}$ and $^{207}\text{Pb}/^{204}\text{Pb}$ ratios through time, the proportion of ^{206}Pb and ^{207}Pb which is initial, or common, can be estimated (Kirkland and Wingate, 2012). The estimated initial radiogenic Pb can then be subtracted from the measured Pb. The use of two independent age chronometer schemes allows loss of radiogenic Pb to be detected.

The ratios of $^{207}\text{Pb}/^{206}\text{Pb}$ and $^{238}\text{U}/^{206}\text{Pb}$ system were used to date the Bentley samples. The $^{207}\text{Pb}/^{206}\text{Pb}$ system is sensitive because ^{238}U is more abundant, and decays more rapidly than ^{235}U (Kirkland and Wingate, 2012). Furthermore, errors are minimized when the ratio of interest involves two isotopes of the same element. The $^{238}\text{U}/^{206}\text{Pb}$ system was used as check to recognise loss of radiogenic Pb during any geological event (e.g., hydrothermal alteration, metamorphism) after the initial crystallization of zircon and monazite. The results were plotted on concordia diagrams of $^{207}\text{Pb}/^{206}\text{Pb}$ versus $^{238}\text{U}/^{206}\text{Pb}$ (Fig. 1.4).

Analyses can be concordant or discordant. The concordia line itself represents the expected relationship between the ratios of $^{207}\text{Pb}/^{206}\text{Pb}$ versus $^{238}\text{U}/^{206}\text{Pb}$ at any given time after mineral crystallization. The age is shown on the concordia in millions (Figure 1.4) or billions of years. In a closed system, without loss or gain of the parent and daughter isotopes, analyses should plot close to the concordia and provide an accurate indication of age (e.g., top red circles, Figure 1.4). If metamorphism induces later growth of zircon or monazite, then rims will form on the original crystal, and if the rims are analysed then the measured age will be younger

than that of the core of the mineral grain, but will plot on the concordia (Figure 1.4). In an open system, the amount of radiogenic isotopes is altered by processes other than natural radioactive decay (e.g., Pb loss), and analyses plot off the concordia. Ancient Pb loss is recognized by analyses that plot along a discordia line (Figure 1.4) that lies between the time of formation and the time of Pb loss. Recent Pb loss occurs when fractures within grains enable Pb to be removed rapidly from the grain. Such analyses plot right of the lower intercept of the discordia (Figure 1.4); these analyses are considered discordant and of no use for age determination.

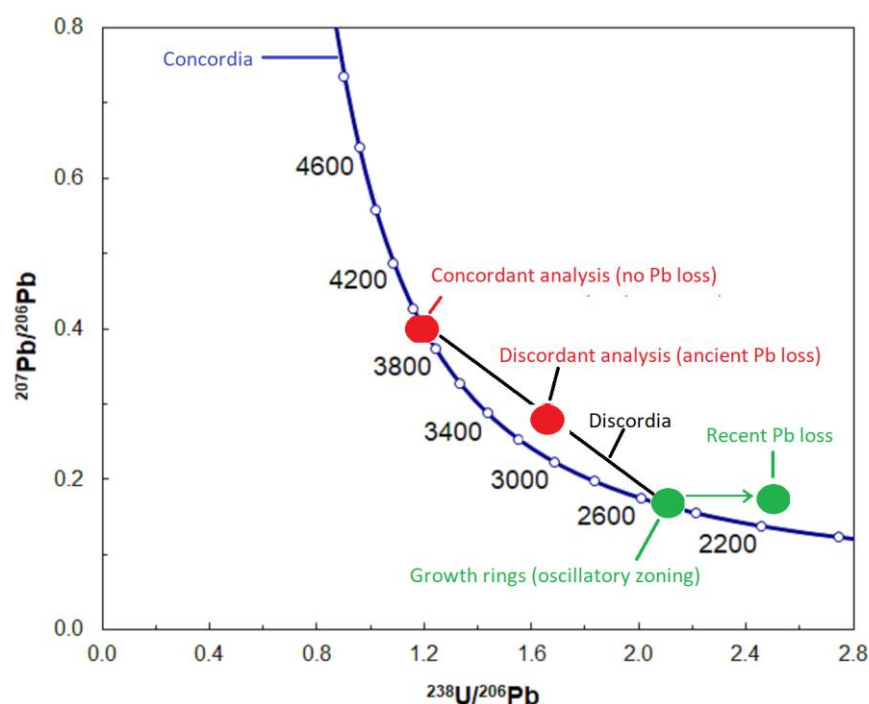


Figure 1.4. A U–Pb concordia diagram, showing the effects of radiogenic–Pb loss from zircon crystals. The concordia curve (blue) is the locus of points where the $^{207}\text{Pb}/^{206}\text{Pb}$ age is equal to the $^{238}\text{U}/^{206}\text{Pb}$ age; the numbers indicate age in Ma. The oldest concordant ages measured in zircon cores (red) reflect the time of magmatic crystallization (c. 3900 Ma in this example) of the rock. Analyses of material that has lost radiogenic Pb lie on a chord (known as a discordia) between the crystallization age and the time of Pb loss (c. 3200 Ma). Damaged zircons, which contain more fractures and other fast–diffusion pathways, have lost more Pb and plot closer to the lower intercept of the discordia. Growth of new zircon rims (green) occurred at ~2500 Ma that was responsible for loss of radiogenic Pb from zircon cores (dispersion to the right).

1.3.5 Scanning Electron Microscope Energy Dispersive Spectrometer (SEM-EDS)

Mineral identification was confirmed by qualitative analysis and back-scattered electron (BSE) imaging with a Hitachi TM3030 table-top scanning electron microscope (SEM) equipped with a SWIFT ED3000 energy dispersive spectrometer (EDS) located at the Western Australian School of Mines, Curtin University, Australia. The accelerating voltage was 15 kV and the filament current was 1850 mA; the EDS detector was calibrated with copper foil. The results of this technique are provided in Appendix 2.

BSE imaging can reveal detailed mineral grain zonation patterns that are invisible or barely visible with conventional transmitted and reflected light microscopy (Hanchar and Miller, 1993). Figure 1.5 displays zonation in a zircon grain and shows: (1) an inner core with an embayment that represents the earliest part of the crystal to form; (2) an outer core; and (3) an oscillatory zone. This zonation can be significant, particularly for dating, because the three zones represent three periods of crystallization. Oscillatory zoning indicates that crystallization occurred within an open system (Holten et al, 2000). The extent to which the system is open or closed during crystallization has significant implications for dating using U–Th–Pb methods (1.3.3).

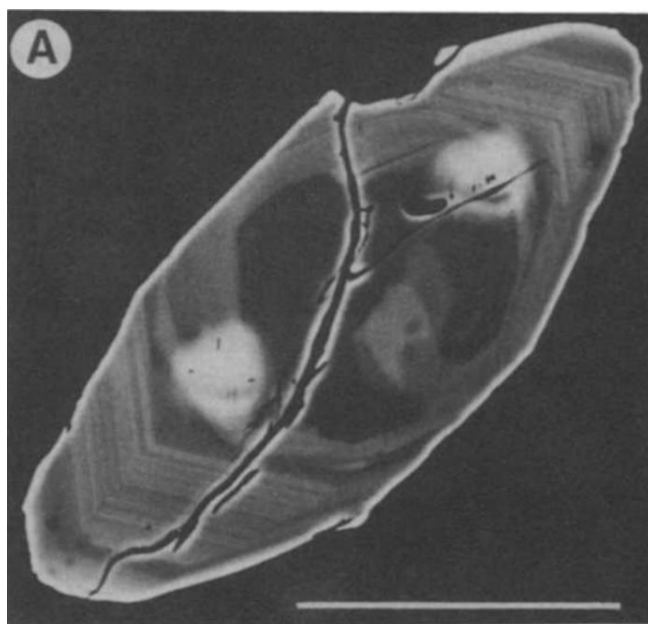


Figure 1.5. Backscattered electron (BSE) zircon image. This zircon is made up of: (1) an inner core (dark grey) with an embayed region; (2) an outer core that truncates the embayed region; (3) a zone of fine-scale oscillatory zoning. Two bright spots either side of crack are sensitive high mass resolution ion microprobe (SHRIMP) analysis spots from previous testing and not due to elemental variations within the zircon. Scale bar is 100 μm . (modified from Hanchar and Miller, 1993).

1.3.6 Transmitted Light Spectroscopy

Six polished thin sections were examined in detail with transmitted light microscopy. This was performed using the Nikon LV100 Pol and Leica DFC290 Digital Imaging Systems, x2 Leica M60 stereo binocular microscopes located at the Western Australian School of Mines, Curtin University, Australia. The instruments were fitted with digital cameras, and images were collected to aid the rock and mineral descriptions and interpretation (Appendix 1.).

2. Geology of the Bentley Deposit

2.1 Regional Geology

The Bentley Zn–Cu VMS deposit is located in the Yilgarn Craton of Western Australia, approximately 300 km north of Kalgoorlie and 65 km north of Leonora (Figure 2.1).

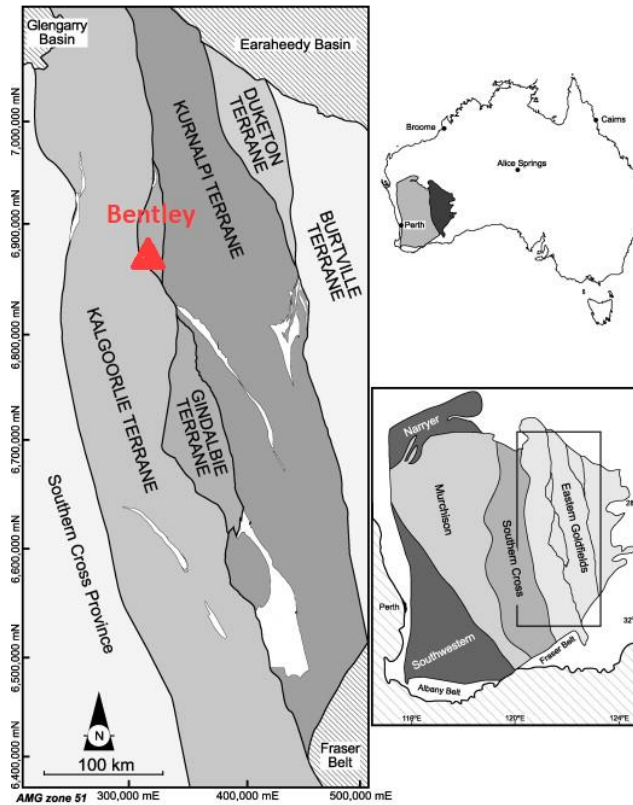


Figure 2.1. Geological map showing the location of the Bentley VMS deposit within the Gindalbie Terrane (Australian Map Grid Zone 51) (modified from Krapež and Barley, 2008).

The deposit occurs in a similar stratigraphic position to Teutonic Bore (1.68 Mt @ 3.5% Cu, 10.7% Zn, 0.9% Pb, 150 g/t Ag; Hollis et al, 2017) and Jaguar (1.6 Mt @ 3.1% Cu 11.3% Zn, 0.7% Pb, 115 g/t Ag; Hollis et al, 2017) VMS deposits (Figure 2.2).

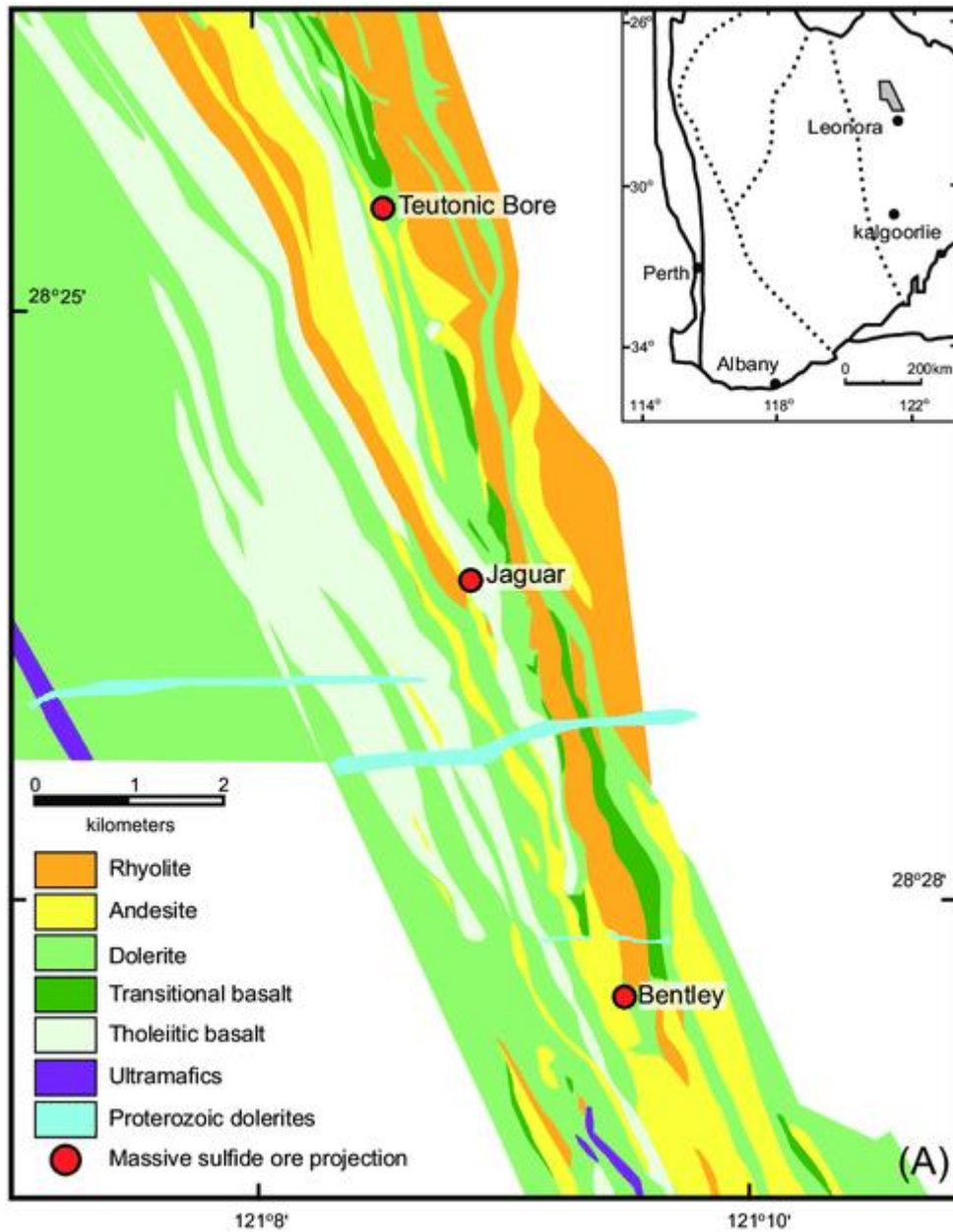


Figure 2.2. Geologic map of the Teutonic Bore volcanic complex, Yilgarn Craton, Western Australia, showing the locations of the Teutonic Bore, Jaguar, and Bentley VMS deposits (modified from Chen et al, 2015).

These deposits are located within the Gindalbie Terrane, which is part of the Eastern Goldfields Superterrane, which covers a large part of the eastern Yilgarn Craton (Belford et al, 2015). The Gindalbie Terrane is considered to have formed in a late Archean volcanic intra-arc setting (Barley et al, 2008; Korsch et al, 2011). The rocks at Teutonic Bore show evidence of bimodal volcanism and plutonism; similar rocks have been described at a number of Archean VMS deposits in Canada (Hallberg and Thompson, 1985).

The Gindalbie Terrane is bounded by the Emu Fault to the east and the Ockerburry–Mount George–Mount Monger Fault to the west. The geology of the Gindalbie Terrane is characterised by bimodal basalt–rhyolite volcanic complexes enriched in the high–field–strength–elements (HFSE), associated with quartz–rich sedimentary rocks and calc–alkaline intermediate–silicic volcanic complexes with ages from 2692 to 2680 Ma (Barley et al, 2008; Belford et al, 2015; Hollis et al, 2015). The volcanic and sedimentary facies indicate sub–aqueous to emergent conditions during volcanism; which comprise of coherent intermediate to silicic lavas, coarse–grained volcanic breccias, high–level intrusions, and volcanogenic sandstones. These facies are commonly intruded by mafic to intermediate sills and dykes. Many of the rhyolites were produced by low–pressure fractional crystallisation or partial melting of andesites (Barley et al, 2008). The adjacent Kurnalpi Terrane is dominated by rhyolitic and dacitic rocks dated at 2720 to 2700 Ma (Barley et al, 2008); these rocks are generally more intermediate in composition than those of the Gindalbie Terrane. The compositional range, eruptive style, abundant mass–flow deposits, and association with late–stage mafic sill complexes of the Gindalbie Terrane are characteristic of intra–arc rift settings (Barley et al, 2008).

The oldest volcanic rocks in the Teutonic Bore area are porphyritic amygdaloidal andesite flows and mass flow breccias, which are overlain by massive and pillow basalts, which underlie rhyolitic volcanic and volcanoclastic rocks. These silicic rocks are overlain by pillow basalts containing discontinuous lenses of immature polymictic conglomerates and greywackes derived mostly from a felsic source, and thinner, more continuous horizons of greywacke, shale, and siltstone (Hallberg and Thompson, 1985). These horizons are intruded by thick mafic sills and have a spatial and temporal association with high–level syenogranites and alkali–feldspar granites (Barley et al, 2008). It is likely that there was a time interval between rhyolite extrusion and the intrusion of their plutonic equivalents, and that basalt was extruded and abundant gabbroic material emplaced during this interval (Hallberg and Thompson, 1985).

Rocks at Teutonic Bore and elsewhere in the Gindalbie Terrane have undergone low grade prehnite–pumpellyite and lower greenschist facies metamorphism but do not show evidence of syn–metamorphic deformation (Hallberg and Thompson, 1985). Most igneous minerals have been altered or replaced by metamorphic minerals, although relict textures and the primary mineralogy can still be recognised in thin section (Barley et al, 2008).

2.2 Local Geology of the Bentley Deposit

The stratigraphy of the Bentley deposit (Figure 2.3) strikes NNW–SSE and dips steeply at 75°–80°W. The host rocks are interpreted as a bimodal volcanic–sedimentary package consisting of a sequence of calc–alkaline volcanic rocks that underlies, and is intruded by, mafic tholeiitic volcanic rocks (Frater, 2010; Stevenson, 2015). The footwall rhyolite, which is the focus of this study, hosts chalcopyrite stringer mineralisation. The rhyolite is overlain by a sequence consisting of felsic volcaniclastics intercalated with younger and older sulphidic black shales and mudstones; the volcaniclastic unit is the main host of massive sulphide mineralisation at Bentley. The hangingwall sequence occurs immediately above the host lithologies, and comprises a sequence of calc–alkaline volcaniclastics, sandstones, mudstones, andesites, and basalts, which show a transition from calc–alkaline to tholeiitic compositions (Frater, 2010). There is no evidence of exhalites or a brecciated horizon within the massive sulphide, its host, or the hangingwall horizon, indicating that ore formation occurred below the seafloor within volcaniclastics and sediments that were at least slightly consolidated.

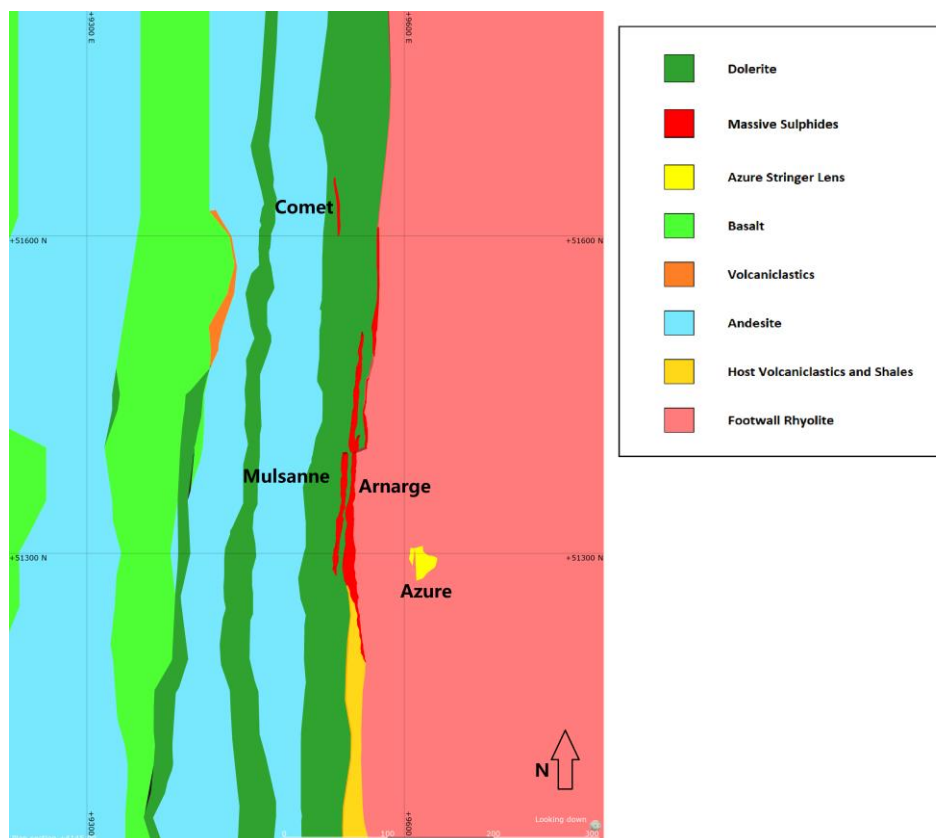


Figure 2.3. Geological Plan Section 4145 rL with ore lenses (Brooklands lens is not present at this level).

2.2.1 Footwall Rhyolite

The footwall rhyolites consist of a fine-grained quartzo-feldspathic matrix with common quartz and rare feldspar phenocrysts.

Alteration phases in the rhyolite include chlorite proximal to the massive sulphide lens and quartz-sericite at the periphery of the deposit. Distal to the deposit, the rhyolite shows few visible signs of alteration, and euhedral to subhedral feldspar crystals are visible in hand specimen (Figure 2.4).



Figure 2.4. Relatively unaltered rhyolite with euhedral feldspar and quartz phenocrysts. Lighter areas show mild sericite alteration with weak feldspar alteration (15TRDD013 740.3–744.8m).

The sericite occurs within the matrix of the rock and within veins, and is generally creamy yellow–green in colour. In the quartz–sericite zone, quartz phenocrysts are generally larger and more euhedral (often >2 mm; Figure 2.5) than in the chlorite zone.



Figure 2.5. Quartz–sericite altered footwall rhyolite (14BUDD005 244.75–248.85m)

This difference might be related to silica addition during the quartz–sericite alteration and/or removal of silica from the chlorite zone. The most intense quartz–sericite alteration is commonly found within the footwall immediately below the mineralisation, where primary feldspar is almost completely altered (Frater, 2010). In the chlorite zone, quartz phenocrysts, if present, are generally <2 mm in size (Figure 2.6), and primary feldspar was not recorded.

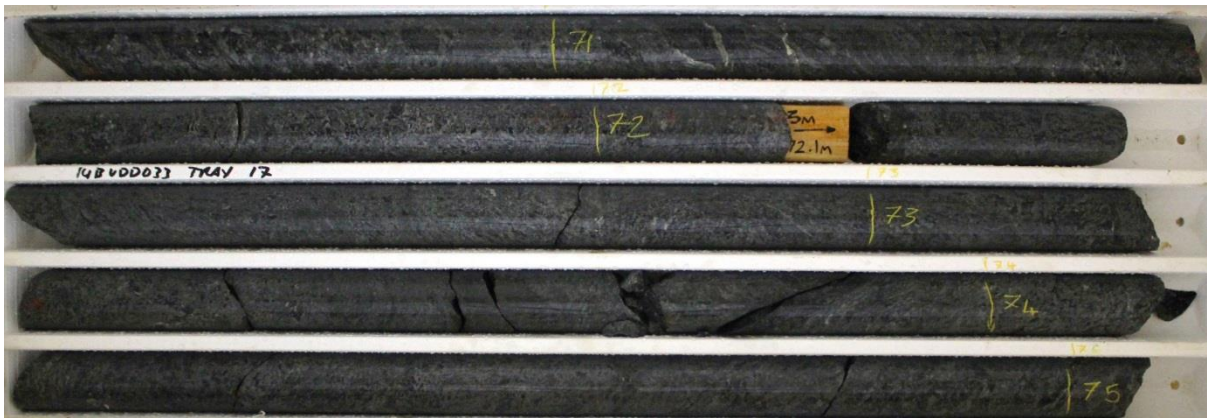


Figure 2.6. Pseudo–breccias within chlorite–altered footwall rhyolite (14BUDD033 70.5–75.05m).

Pseudo–breccia textures comprised of quartz phenocrysts within a chlorite–rich matrix occurs in some places; this texture is attributed to mass loss associated with silica removal (Gifkins et al, 2005). The pseudo–breccias are interpreted as intensely altered rhyolite. They are distinguished from true breccias by the presence of quartz crystals that cross the contacts between clast and matrix, and the quartz grains that are present in similar proportions in both the clasts and the matrix. The chlorite–bearing rhyolites can be easily distinguished from the

quartz–sericite rhyolites.; quartz phenocrysts within the chlorite–bearing lithology are darker and smaller than quartz phenocrysts elsewhere (Figure 2.6). In some places, quartz phenocrysts are absent and the matrix consists of almost 100% chlorite; this is a true breccia and is commonly associated with chalcopyrite/pyrite stringer mineralisation (Figure 2.7). It is referred to here as an infill–type vein texture. The preferred explanation for this texture is that it represents fault structures infilled with chlorite.



Figure 2.7. Chalcopyrite–pyrite stringer mineralisation within intensely chlorite–altered rhyolite in the Azure Lens (13BUDD077 58.3–62.7m).

2.2.2 Host Lithologies

The volcanoclastic unit that hosts the massive sulphide mineralisation consists of bedded quartzo–feldspathic arenites and sandstones, granule conglomerates, fine–grained pumice breccias, and vitric ash siltstones. The most common lithologies are well–sorted arenites and sandstones that have been interpreted as megaturbidites or mass flows (Frater, 2010). Sangster (1972) recognised an association between similar felsic units and massive sulphide ores in a number of Precambrian VMS mining camps in Canada. Outcrops of these rocks were referred to as “mill rocks” because they always occurred within earshot of a mine mill. To the south of the deposit, the host package contains a poorly–defined and poorly understood felsic intrusive unit colloquially referred to as “rhyodacite”, which appears to have been extruded into the volcanoclastic beds prior to consolidation. A black shale unit occurs at the top of the sequence, which acts as an upper marker for the host horizon. The massive sulphides formed or were remobilised within this shale, but do not occur above it. This suggests that the shale formed an impermeable cap that prevented fluid flow into the hangingwall lithologies. An earlier shale is also present within the volcanoclastics and though

thinner it has caused a capping effect with massive sulphides having formed below it. The host volcanoclastics have undergone phyllic alteration to quartz, sericite, chlorite, and carbonate with minor pyrite. Local pervasive silicification has been recorded, particularly in volcanoclastics between the massive sulphides and the footwall rhyolite. Silicification is most intense directly beneath the massive sulphide lenses, and is more commonly present adjacent to chalcopyrite-rich mineralisation. The most intensely silicified rocks have a chert-like appearance.

2.2.3. Mafic Intrusive Rocks

Multiple tholeiitic dolerite dykes intrude the mineralised volcanic–sedimentary package, and at least two dolerites cross-cut, and are close to concordant with, the mineralised horizon. The dolerites are commonly amygdaloidal at the margins and coarsen towards the base of the units, consistent with crystal settling. Dolerites account for approximately 25% of the rocks classified at Bentley (Frater, 2010). These mafic intrusive units dissect at least one ore lens to form the Mulsanne and Comet lodes (Figure 2.3), which have both footwall and hangingwall dolerite contacts.

2.3. Bentley VMS Mineralisation and Classification

In 2015, the Bentley mineral resource consisted of a total resource of 2.96 million tonnes with 8.7% Zn, 1.5% Cu, 139 ppm Ag, 0.9 g/t Au and 0.7% Pb (Stevenson, 2015). Large (1992) used two metal ratios to classify Australian VMS deposits; this classification system is similar to those of Hutchison (1972) and Solomon (1976). The classification system is based on the Cu ratio ($100 \text{ Cu}/(\text{Cu} + \text{Zn})$) and the Zn ratio ($100 \text{ Zn}/(\text{Zn} + \text{Pb})$). Copper deposits have a Cu ratio of >60 and a Zn ratio >60 ; Zn–Cu deposits have a Cu ratio <60 and a Zn ratio >90 ; and Zn–Pb–Cu deposits have a Cu ratio <60 and a Zn ratio between 60 and 90. Based on these criteria, Bentley is a Zn–Cu deposit, with a Cu ratio of 14.7 and a Zn ratio of 92. Hutchison (1972) notes that Zn–Cu VMS often contain significant amounts of Ag and Au. The Teutonic Bore (Cu ratio 13.5, Zn ratio 92.2) and Jaguar deposits (Cu ratio 12.4, Zn ratio 94.2) are also classed as Zn–Cu VMS deposits, based on the Large (1992) classification scheme and the resource data of Hollis et al (2017). Many of Canada's Archean VMS deposits are also classified as Zn–Cu (Hutchison, 1972; Large, 1992).

Mineralisation consists primarily of a rhyolite-hosted stringer zone (Azure) and five massive sulphide lenses: Arnage; Brooklands; Mulsanne; Comet; and Flying Spur. The massive sulphide lenses are primarily composed of pyrite with lesser amounts of sphalerite (~30%)

and chalcopyrite (~4%). The pyrite is subhedral to anhedral and the grain size ranges from <1 mm to >20 mm. There are two main types of sphalerite: a coarse-grained to medium-grained, deep purple, massive type; and an orange-brown, fine-grained, type associated with the silicic over-print. The coarse type is commonly found as large masses or intercalated with pyrite-rich bands. Coarse sphalerite-rich samples have been assayed at over 30% Zn, and some contain small amounts of argentiferous galena. The fine-grained orange sphalerite often occurs within the silica-altered volcanics that host the massive sulphide mineralisation, and as stringer mineralisation within the footwall rhyolite. The mineralogy is consistent with the metal ratio classification schemes (Hutchison, 1972; Sangster, 1972; Large, 1992).

The Brooklands lens (Figure 2.8) formed directly below the black shale at the top of the ore horizon. Relic volcanoclastics are present within massive sulphides with unmineralised volcanoclastics present on the footwall contact.



Figure 2.8. The Brooklands ore lens on the 4000 RL (relative level), looking north.

The Arnarge massive sulphide lens (Figure 2.9) is the largest orebody and formed below the footwall contact of the oldest black shale within volcanoclastics. On the shales hangingwall contact lays another volcanoclastic unit.

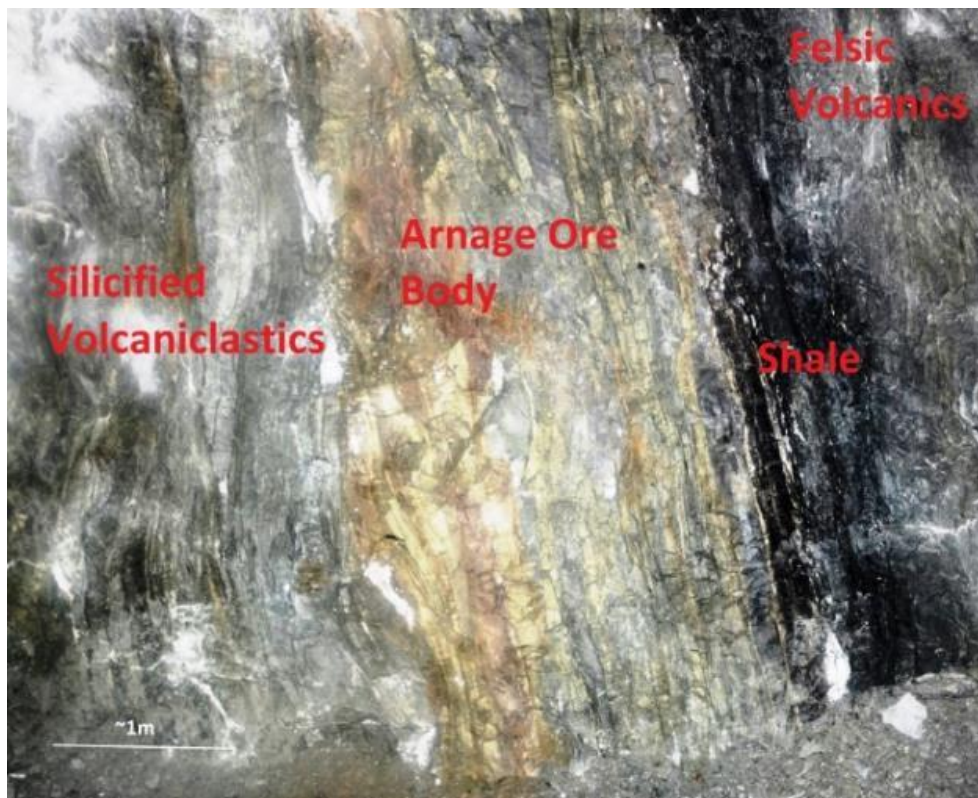


Figure 2.9. The Arnage ore lens on the 3940RL, looking south.

The Azure chalcopyrite stringer zone, and other minor economic and sub-economic stringers at Bentley, consists of chalcopyrite \pm sphalerite-carbonate stringer veins with chlorite-rich alteration halos. A coarse brecciated rock with chlorite infill and chlorite-altered clasts is observed in the footwall associated with the Azure mineralisation. This texture is also found in other minor stringer zones with little or no chalcopyrite, and is considered to represent a major fluid pathway (Figures 2.7, 2.10).

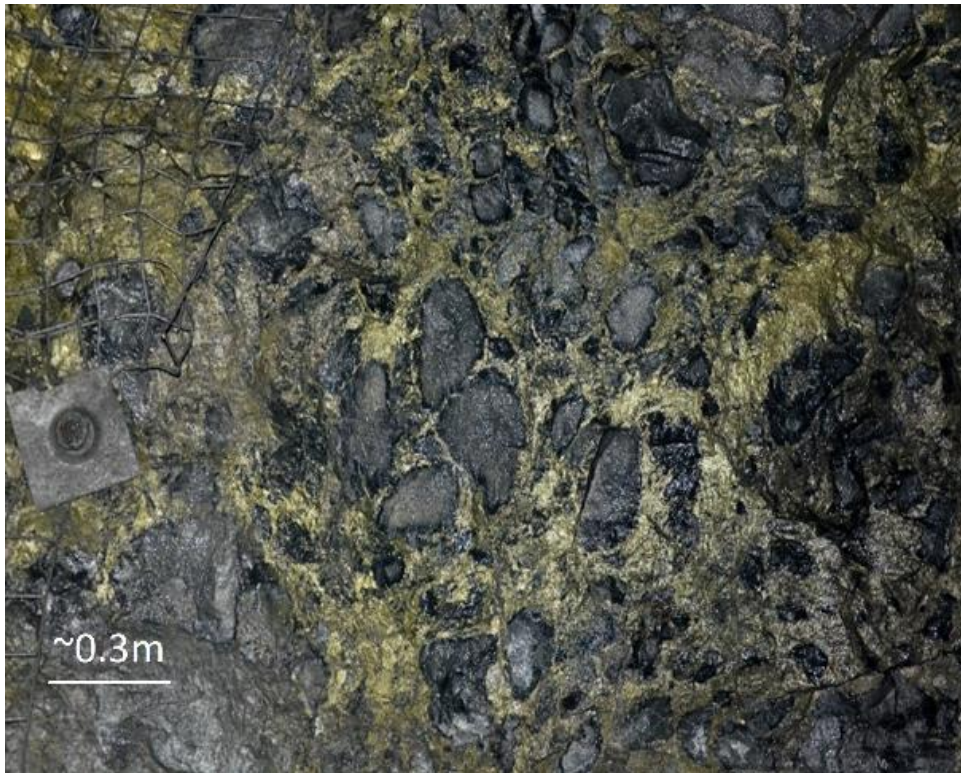


Figure 2.10. The Azure orebody on the 4140 RL access drive. A chlorite–altered rhyolite fault breccia hosts intensely mineralised chalcopyrite–pyrite stringer mineralisation.

The Mulsanne (Figure 2.11) and Comet lenses are located between the Arnage and Brooklands lens. Dolerite has intruded along both the hangingwall and footwall contacts of both. Relic volcanoclastics can be observed in the lens although it is not clear if they correspond to the Arnage or Brooklands.



Figure 2.11. The Mulsanne lens. Looking north on the 4100 RL.

3. Petrography

3.1 Objectives

Six samples that represent the different alteration assemblages present in the footwall rhyolite were selected for petrographic analysis. The results of the petrography were used to ground truth the SWIR data. Details of the six samples, including selected SWIR spectral information, are provided in Table 3.1. Abbreviations are those of Whitney and Evans (2010). Mineral modes and some details additional to those in the text are provided in Appendix 1.

Table 3.1. Details of samples selected for petrography.

Thin Section Spectral Values						
Thin Section ID	Hole ID	From (m)	To (m)	White Mica (2200 nm)	Chlorite (2250 nm)	Chlorite White Mica hqd2250/hqd2200
A4	BA4020A	56	56.1	2195.39	NULL	NULL
A5	13BUDD140	107.2	107.4	2201.27	2253.83	2.362
A6	BAD14015	160	160.1	NULL	2253.69	NULL
A7	BAD14008	316	316.1	2197.09	2243.57	0.18
A8	15TRDD013	744	744.1	2216.03	NULL	NULL
A9	15TRDD013	745	745.1	2214.64	NULL	NULL

NULL: No Value

3.2 Petrographic Results

Samples A8 (Figure 3.1) and A9 (Figure 3.2) contain unaltered plagioclase feldspar and sanidine phenocrysts. Quartz phenocrysts are subhedral and show dissolution embayments. Sample A9 (Figure 3.2) contains twinned sanidine phenocrysts and minor chlorite. The phenocrysts in A8 and A9 occur within a matrix of quartz and brown sericite that defines a metamorphic fabric.



Figure 3.1. Sample A8: Subhedral quartz, sanidine and plagioclase phenocrysts in a quartz–sericite matrix. The preferred orientation of the sericite defines a metamorphic foliation (XPL).

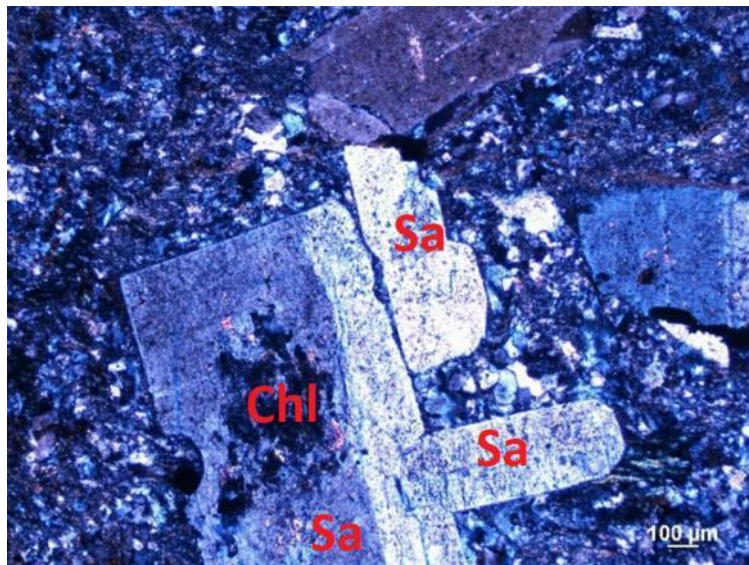


Figure 3.2. Sample A9: Twinned subhedral feldspar (sanidine) crystals with chlorite in a quartz–sericite matrix (XPL).

Sample A4 shows relict feldspar textures within sericite alteration (Figure 3.3). The matrix is similar to the matrix in samples A8 and A9, and consists mostly of quartz and brown sericite. The sericite that replaces the feldspar shows higher birefringence than the matrix sericite. Carbonate is also present.

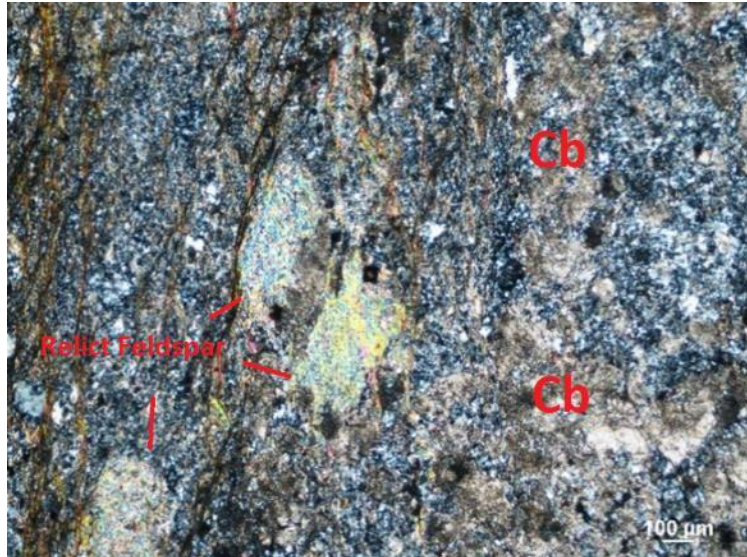


Figure 3.3. Sample A4: Relict feldspars within sericite alteration in a carbonate-bearing quartz-sericite groundmass. The brown sericite defines a metamorphic foliation. The feldspar is pseudo morphed by the higher birefringence sericite (XPL).

Sample A7 consists of high-birefringence sericite within a quartz-rich matrix (Figure 3.4). There are no remnants of primary feldspar. Abundant quartz is present as large clasts in this sample.



Figure 3.4. Sample A7: Fine bright sericite veins define a metamorphic foliation. Minor Mg-rich chlorite and opaque minerals (pyrite, sphalerite) are present within the quartz matrix.

Samples A5 (Figure 3.5) and A6 (Figure 3.6) are chlorite-rich samples with minor carbonate veins, sphalerite, and chalcopyrite. There is abundant Fe-oxide staining in sample A6 consistent with an Fe-rich bulk composition and/or the presence of weathered sulphides.

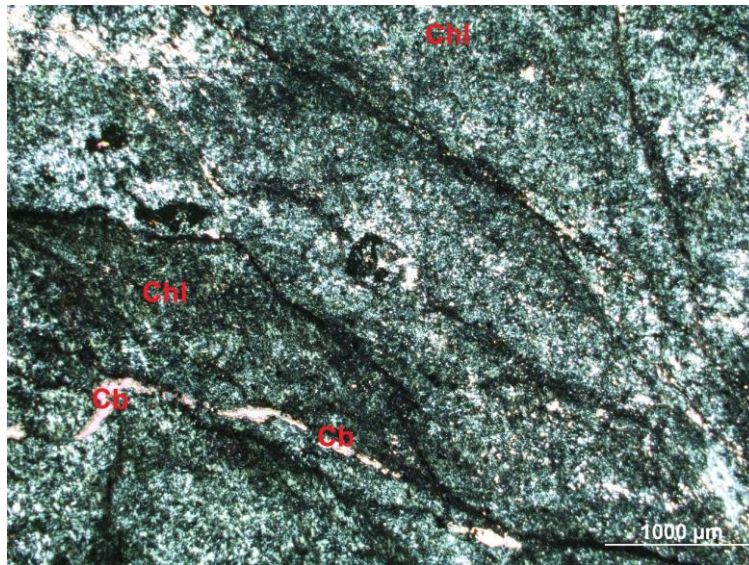


Figure 3.5. Sample A5: Fine carbonate veins (white) within chlorite-rich groundmass (XPL).

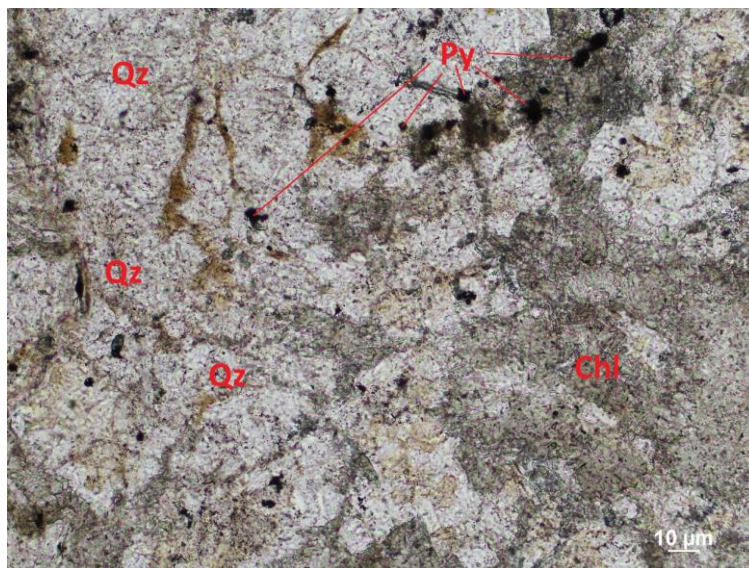


Figure 3.6. Sample A6: Chlorite within a quartz matrix. Note Fe staining (brown) and pyrite and chalcopyrite (opaque grains) (PPL).

3.3 Interpretation

To aid in interpretation the approximate locations of where the thin sections were sampled is provided in Figure 3.7.

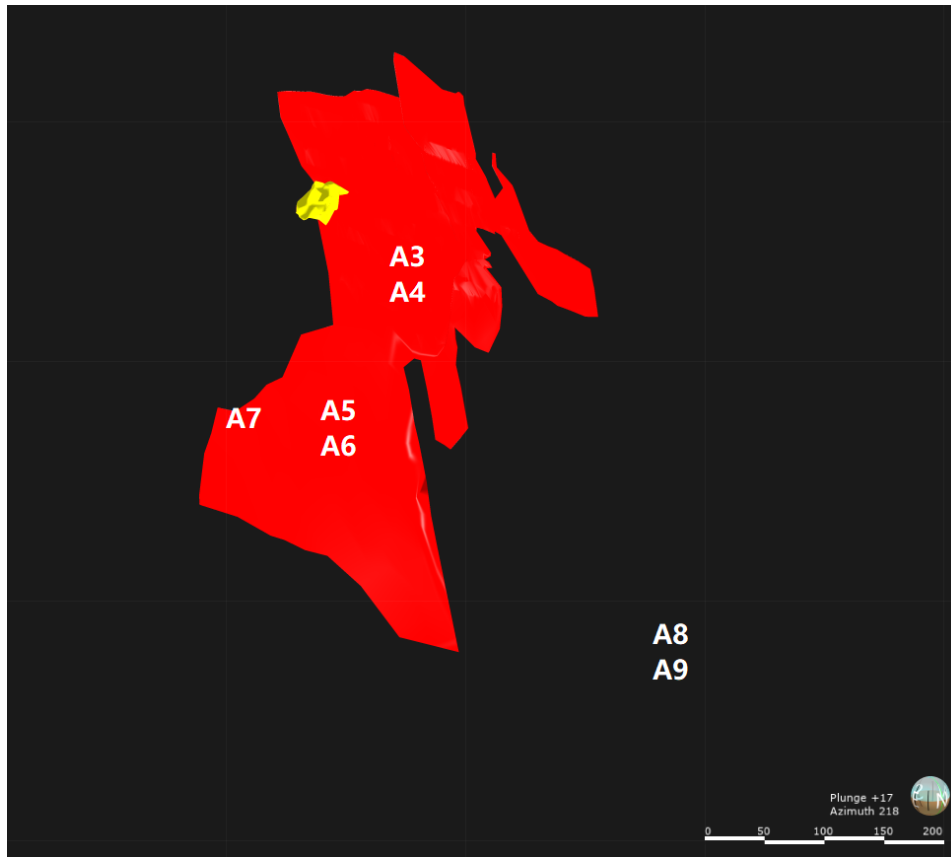


Figure 3.7. Thin Section Sample Points looking southwest. Red is massive sulphide lenses yellow is Azure stringer lens.

3.3.1 Least-altered rocks

Samples A8 (Figure 3.1) and A9 (Figure 3.2) show the least alteration in hand specimen, consistent with the results of the petrographic analysis. In these samples, the presence of euhedral feldspar phenocrysts with little or no alteration indicates that rocks from this zone did not interact much with hydrothermal fluids. The embayed subhedral quartz phenocrysts indicate that the primary melt was water-bearing (Donaldson and Henderson, 1988).

The matrix of samples A8 (Figure 3.1) and A9 (Figure 3.2) is formed by quartz and brown-green sericite. The sericite is interpreted to have formed from fine-grained feldspar during regional metamorphism. Similarly, chlorite is interpreted to have formed from mafic minerals during metamorphism. The presence of coarse phenocrysts in a fine-grained matrix suggests that the melt underwent at least two stages of crystallization. The first stage formed the

phenocrysts, most likely within a magma chamber, and the precursor to the existing metamorphosed matrix formed during rapid cooling after eruption.

The SWIR features at 2216.13 nm for A8 and 2214.64 nm for A9 indicate that these samples contain phengitic white mica. The lack of peaks characteristic of chlorite is consistent with the lack of chlorite noted in the petrographic investigation. The SWIR features are consistent with evidence of limited hydrothermal alteration provided by the unaltered feldspar and their distance from mineralization (Figure 3.7).

3.3.2 White mica—rich rocks

The SWIR feature at 2195.39 nm in the spectrum from A4 indicates that this sample is more altered than A8 and A9 (Figure 3.3), consistent with the absence of feldspar phenocrysts or relict textures after feldspar. The SWIR spectrum of sample A4 does not show any features diagnostic of chlorite and indicates that the white mica is high-Al muscovite, consistent with the petrographic observations.

Sample A4 was collected at 4020 RL, close to the massive sulphide lens, and is inferred to have been below the lens when it formed (Figure 3.7). Paragonite-bearing silicified rocks have been reported below modern VMS sulphide mineralisation at the Mid-Atlantic Ridge (Shanks and Thurston, 2012).

The feature at 2197 nm in the SWIR spectrum of A7 is characteristic of a high-Al white mica. The calculated chlorite:white mica ratio is 0.18, consistent with the sericite-rich assemblage. Features at 2250 nm and 2243 nm indicate that the chlorite is Mg-rich. If chlorite varies from Fe-rich to Mg-rich with increasing distance from the deposit (Figure 3.7), then this sample would represent the outer boundary of the sericite zone.

The feldspars within less altered rhyolites (samples A8 and A9) are replaced by highly birefringent white mica in samples A4 and A7, and the brown phengitic sericite has been replaced by the highly birefringent white mica. These observations are consistent with the SWIR spectral features.

3.3.3 Chlorite—rich rocks

Samples A5 and A6 are likely to be from the most intensely altered parts of the hydrothermal alteration zone. These samples contain significant amounts of chlorite, a lack of feldspar, and white mica is minor or absent. The lack of white mica is consistent with the values of NULL and 2.36 calculated for the chlorite:white mica ratio for samples A5 and A6, respectively. The feature at 2250 nm indicates that the chlorite in these samples is Fe-rich.

Chlorite is a diagnostic mineral of zones within the footwall that host the chalcopyrite– (cp) and pyrite (py)–bearing stringer veins (Thompson and Thompson, 1996). These zones are typically dominated by chlorite (>50 wt.% and commonly >80 wt.%), with subordinate amounts of quartz, pyrite, and sericite, with or without carbonate (Gifkin et al, 2005). Footwall alteration zoning of this type has been noted in Precambrian deposits. In contrast, Mg–rich chlorite occurs near the mineralisation in some younger deposits (Thompson and Thompson, 1996). Thompson and Thompson (1996) suggested that the Mg–rich chlorite records interaction of cold sea water with hot hydrothermal fluids.

The lack of feldspar, minor sericite, and evidence of sericite replacement in samples A5 and A6 are consistent with extensive progress of the reactions above, and with the SWIR results for these two samples. These samples experienced the highest temperatures and the greatest extent of hydrothermal alteration.

Notably, the most abundant mineral is quartz; quartz is a common alteration mineral in VMS systems was also a major constituent of the host rhyolite.

4. SWIR Data

4.1 Objectives of SWIR data processing

The SWIR data were processed to create histograms that enabled identification of groups and trends in: white mica compositions from features around 2200 nm, chlorite compositions from features around 2250 nm, and the relative abundance of chlorite to white mica based on $2250\text{hqd}/2200\text{hqd}$ (referred to subsequently as the chlorite:white mica ratio).

The results show whether chlorite or white mica is dominant in a sample. A mineral is referred to as 'dominant' when it is present in greater abundance than the non-dominant phyllosilicate. The dominant mineral was determined from the values of the hull quotient depth of absorption (hqd). Samples with the greatest depth of absorption for the 2250 nm feature are chlorite-dominant and those with the greatest absorption at the 2200 nm feature are considered white mica-dominant.

4.2 Results

Cumulative frequency histograms of the SWIR data were produced. Chlorite-dominant samples and white mica-dominant samples are shown on the same histogram.

White mica (Al-OH) wavelengths were investigated for the chlorite- and white mica-dominant samples (Figure 4.1). The wavelengths of white mica absorption in chlorite-dominant samples are normally distributed, indicating a single population. White mica in the majority of chlorite-dominant samples absorbs at wavelengths between 2195 and 2200 nm, indicating that the white mica is muscovite ($\text{KAl}_3\text{Si}_3\text{O}_{10}(\text{OH})_2$) (Pontual, 2011).

In contrast, white mica wavelengths in the white mica-dominant samples show a bimodal distribution. The majority of analyses show features between 2193 nm and 2201 nm; these wavelengths lie in the transition between muscovite and Al-rich white mica, and are similar to the wavelengths of the white mica in the chlorite-dominant samples. A minority of samples produced white mica wavelengths between 2200 nm and 2217 nm, consistent with phengitic/celadonic micas. These micas are more Mg-, Fe- and Si-rich than the white micas in the majority of analyses.

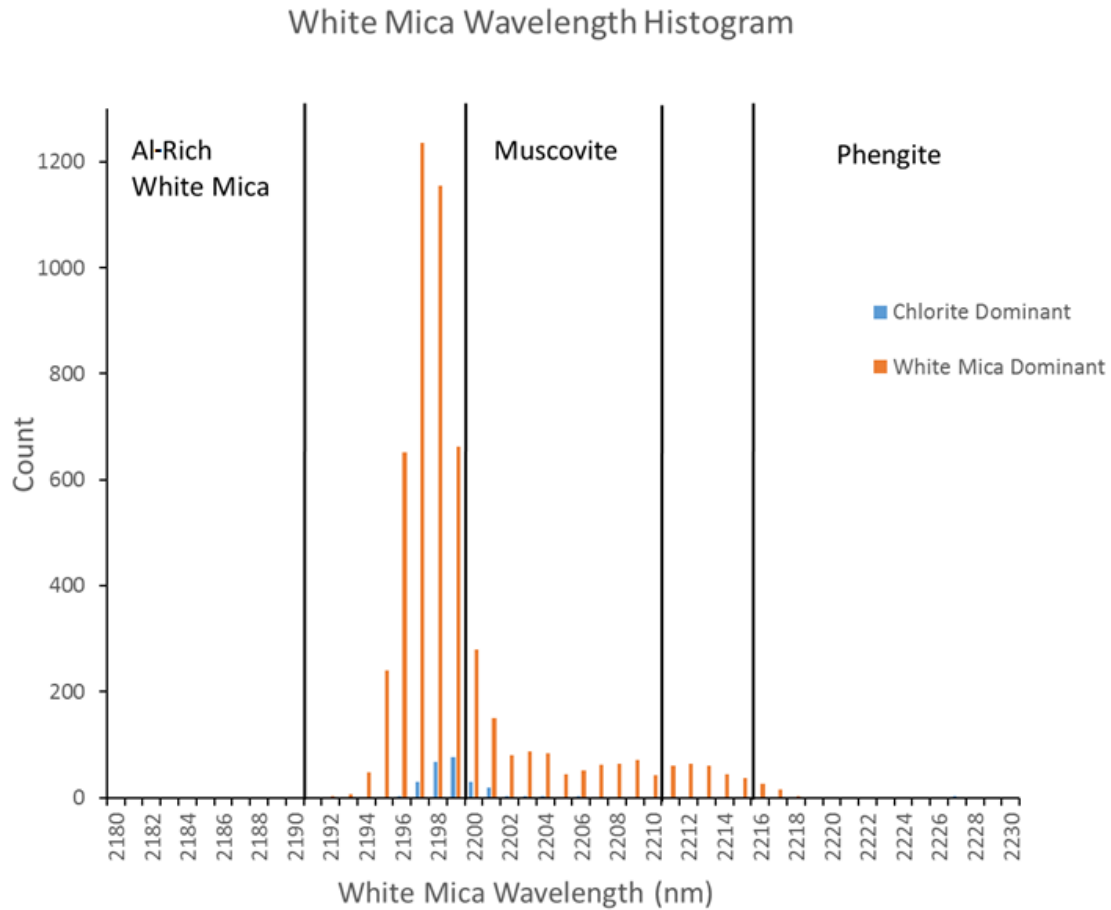


Figure 4.1. Histogram of Al–OH white mica wavelengths (2180–2228 nm) for chlorite and white mica–dominant samples, showing the diagnostic wavelength ranges for mineral types (Pontual, 2005). Unlabelled wavelength ranges indicate transition zones between minerals.

When the 2200 nm spectral data is observed in relation to the Bentley ore bodies (Figure 4.2.) zoning can be observed. Samples with wavelengths shorter than 2200nm appear to be associated with massive sulphide lenses with those greater being found around the periphery of the deposits. The Azure stringer lens appears associated with wavelengths between 2200 and 2195nm.

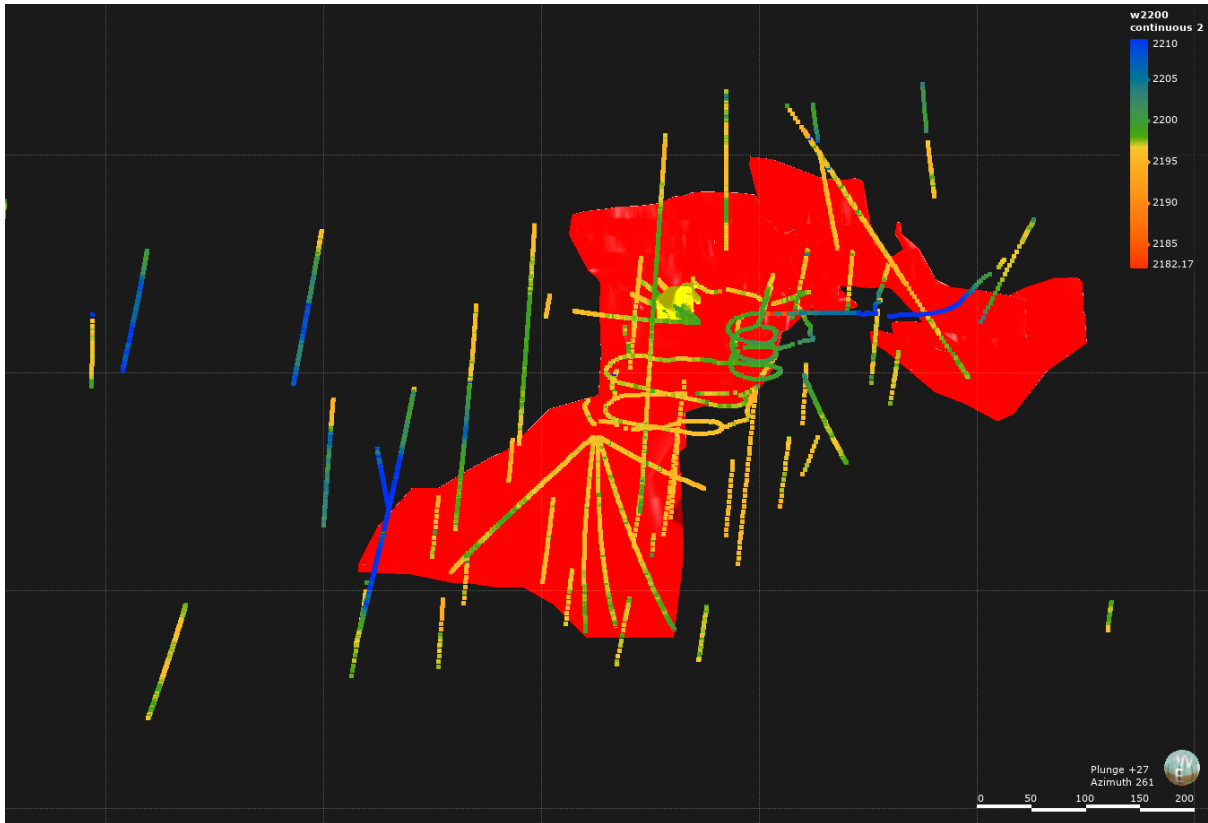


Figure 4.2. Oblique section looking southwest displaying 2200 nm (white-mica wavelength) SWIR spectra heat range in the footwall rhyolite with massive sulphide lenses (red) and Azure stringer lens (yellow).

The wavelengths of Fe–OH chlorite–related features were between 2250 to 2265 nm (Figure 4.3). These wavelengths form a normal distribution centred at the upper end of the range considered to represent intermediate (Fe, Mg) chlorite, and close to that of the Fe–rich chamosite $((\text{Fe}^{2+}_{10}\text{Al}_2)(\text{Si}_6\text{Al}_2\text{O}_{20}(\text{OH})_{16})$ endmember. The wavelengths of chlorite absorption in the white mica–dominant samples show a bimodal population with a smaller, negatively skewed population at 2240–2245 nm and a larger normally distributed peak at 2245–2260 nm. The larger peak represents chlorite of intermediate composition. The smaller peak represents absorption at less than 2244 nm; these wavelengths indicate the presence of Mg–rich chlorite with a clinocllore–like composition $((\text{Mg}_{10}\text{Al}_2)(\text{Si}_6\text{Al}_2\text{O}_{20})(\text{OH})_{16})$.

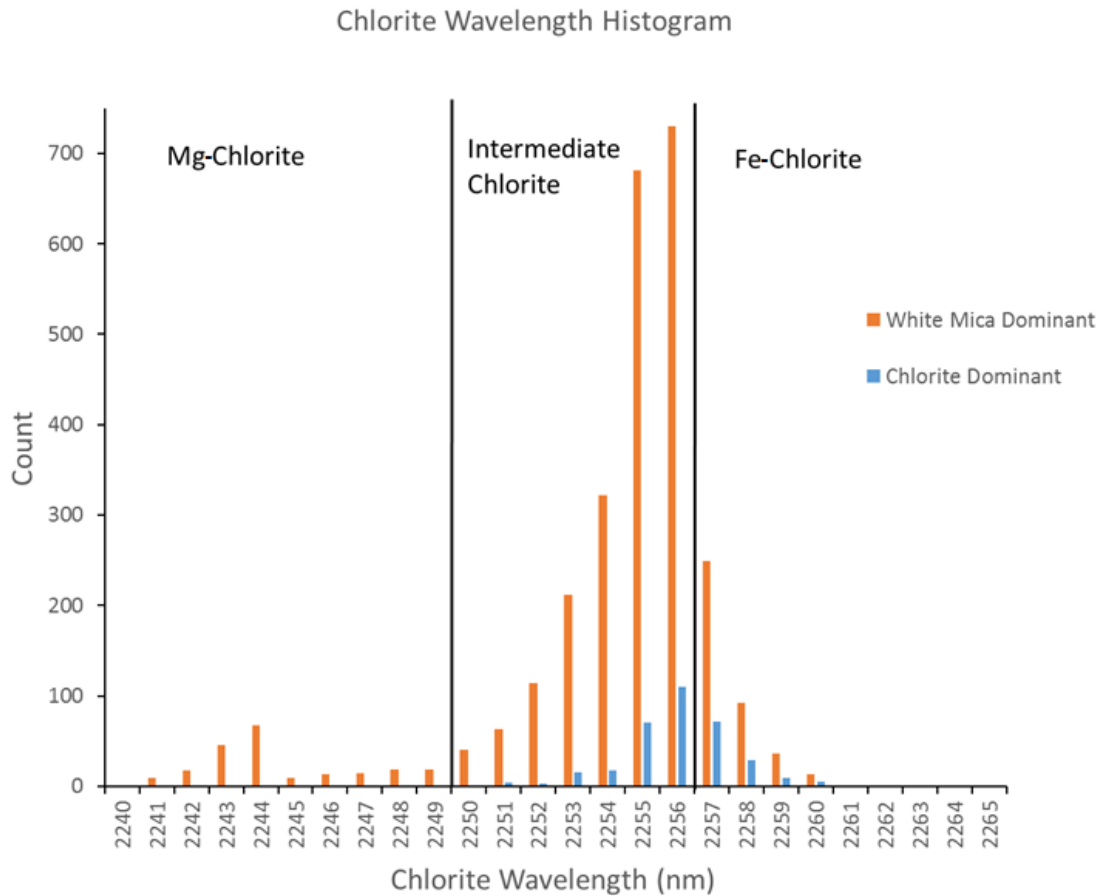


Figure 4.3. Histogram of Fe–OH chlorite wavelengths (2240–2265 nm) for chlorite and white mica–dominant samples, showing the diagnostic wavelength ranges for chlorite compositions (Pontual, 2005).

When the 2200 nm spectral data is observed in relation to the Bentley ore bodies (Figure 4.5.) it can be observed that sample points with chlorite spectral signatures appear spacially associated with the massive sulphide and stringer mineralization. The Mg–rich (<2250 nm) spectra generally are located away from the mineralization with chlorite spectral responses in general being sparse in these areas.

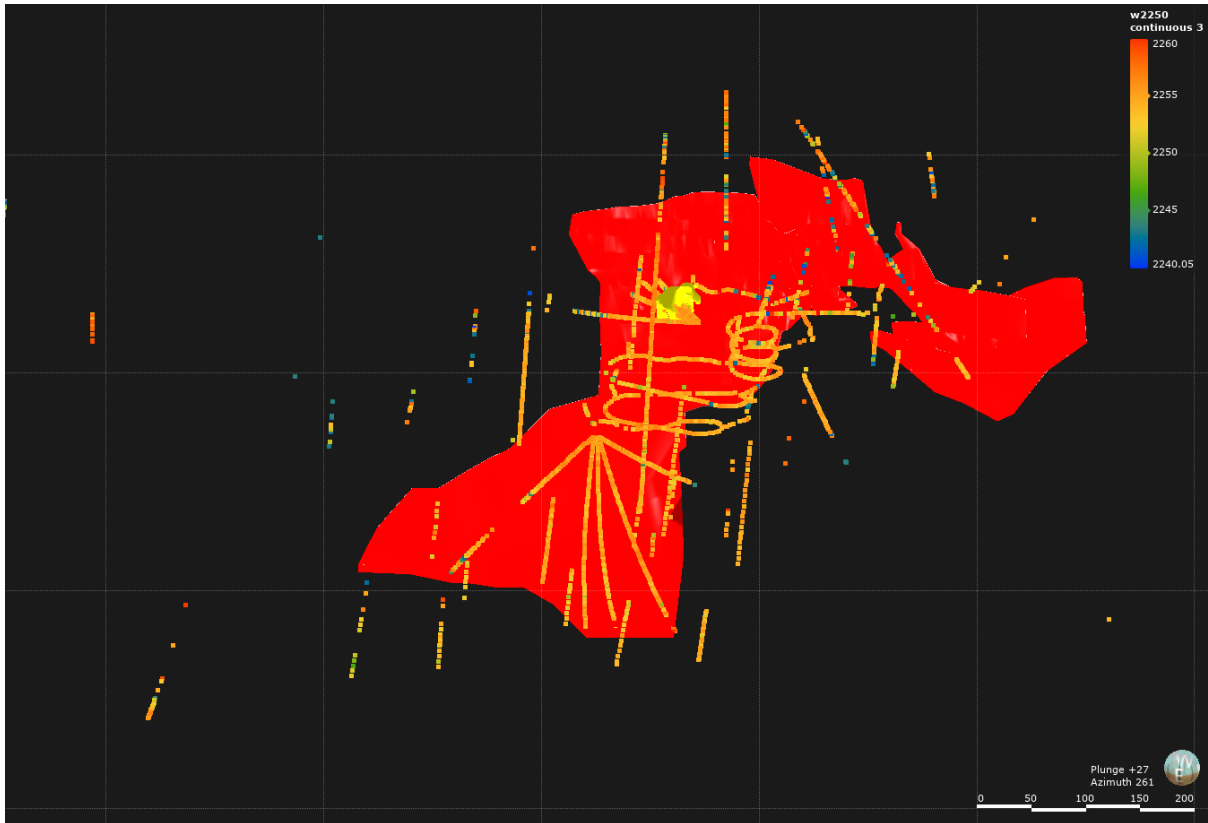


Figure 4.4. Oblique section looking southwest displaying 2250 nm (Fe– chlorite wavelength) SWIR spectra range in the footwall rhyolite with massive sulphide lenses (red) and Azure stringer lens (yellow).

The hull quotient depth ratios (hq_{2250}/hq_{2200}) are plotted in Figure 4.5. Ratios <1 indicate white mica–dominant samples, ratios equal to 1 indicate 50% white mica and 50% chlorite, and ratios >1 indicate that chlorite was dominant. This ratio cannot be calculated for samples that do not contain both white mica and chlorite. The hq_{2250}/hq_{2200} of the white mica–dominant samples are normally distributed, while those of the chlorite–dominated samples show a positively skewed population.

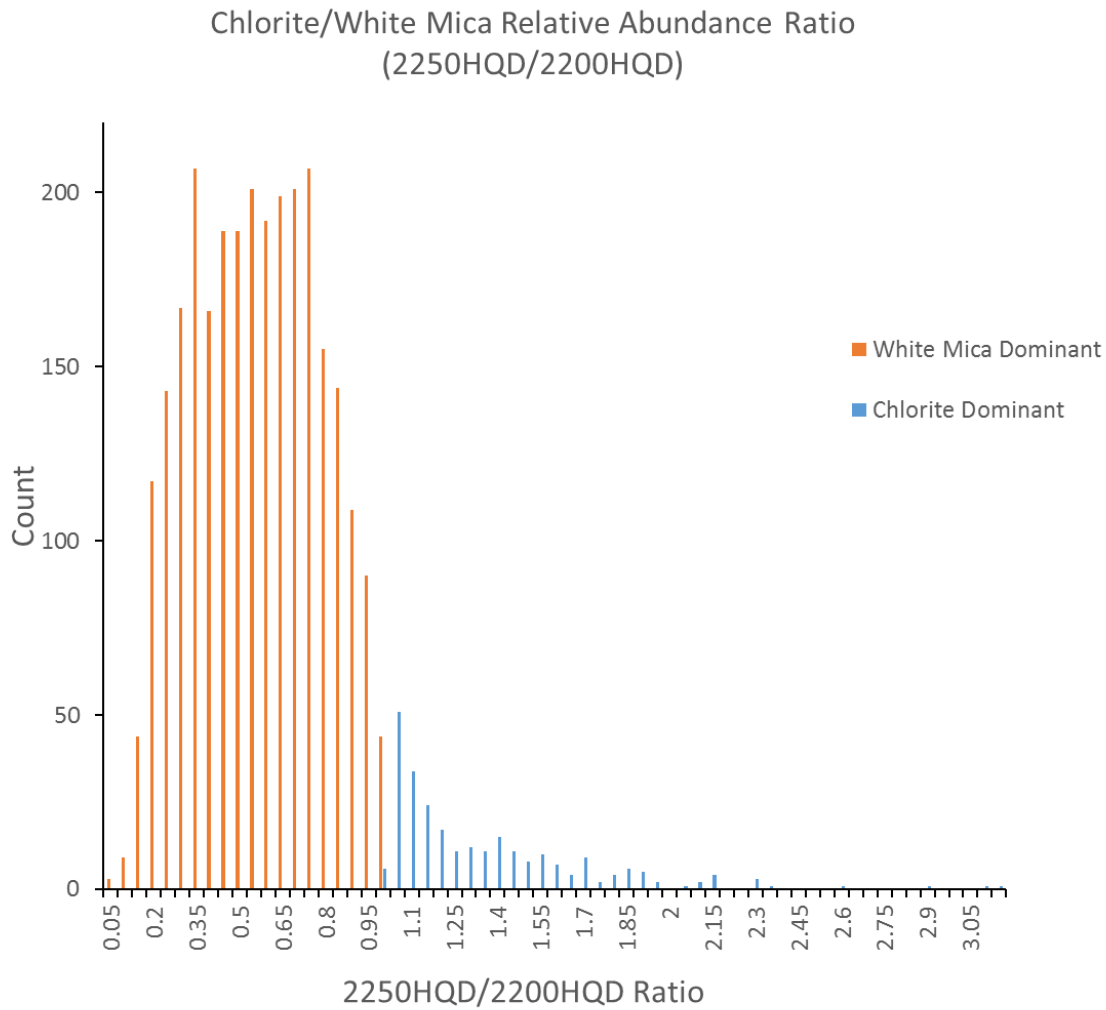


Figure 4.5. Histogram of hull quotient depth ratios, representing the ratio of chlorite to white mica.

The 2250/2200HQD (Figure 4.6.) ratio spectral data shows a similar distribution within samples to that of the chlorite. Higher ratios (>8) are generally located in a close proximity to mineralization although lower ratios appear directly alongside the orebody. Although samples with ratios further away from known mineralization are sparse, they are generally <0.4.

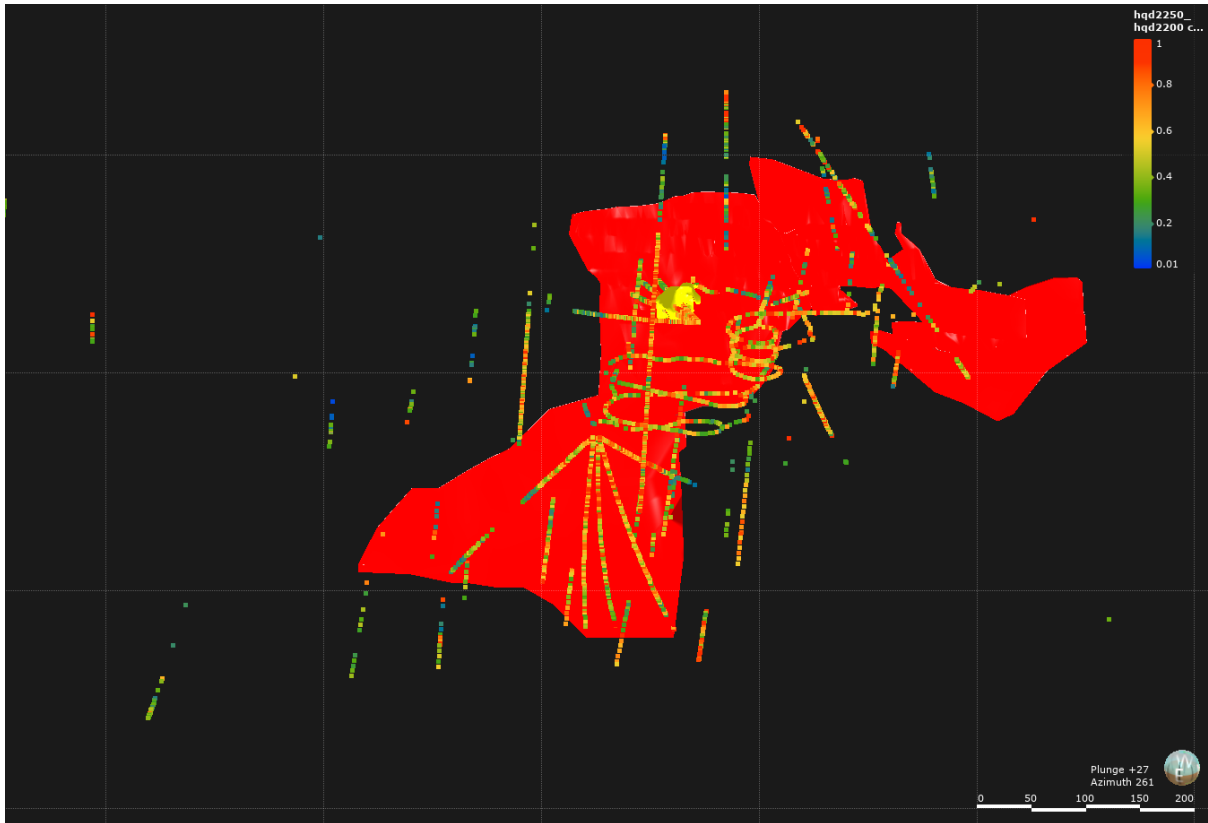


Figure 4.6. Oblique section looking southwest displaying 2250/2200 hull quotient depth ratio in the footwall rhyolite with massive sulphide lenses (red) and Azure stringer lens (yellow).

4.3 Interpretation

4.3.1 White Mica Wavelength

Samples that absorb at wavelengths greater than 2201 nm are interpreted as a record of a zone of muscovitic white mica in the transition between the distal alteration and the hotter proximal chlorite-rich zone. The compositional shift is consistent with a Tschermak substitution of Mg and Fe for Al (Duke, 1994; Jones et al, 2005). Samples with absorption at, or less than, 2197 nm contain white micas that have undergone replacement of Mg and Fe by Al in the presence of hot acidic fluids. Potassium within the interlayer cation sites might also have been replaced by Na to form paragonite, or by other elements, including Ca, Rb, Sr, and Pb (Jones et al, 2005).

4.3.2 Chlorite Wavelengths

Absorption by chlorite–dominant samples in the 2253–2260 nm range is summarised in Figure 4.3. Most chlorite in chlorite–dominant samples are Fe–rich. Iron–rich chlorite zones in VMS deposits are also reported by Large et al (1998) and Galley et al (2007). The chlorite–rich core and areas where chlorite has completely replaced or infilled voids are interpreted as a record of the highest temperature hydrothermal alteration. Chlorites in the white mica–dominant samples fall into two distinct populations. The first population, which is normally distributed, consists of chlorite of slightly Fe–rich to intermediate composition. These chlorites are from an area surrounding the chlorite–rich zone (Figure 4.4), which record the alteration of white mica to chlorite. The second group consists of white mica–dominant samples that contain Mg–rich chlorite. Chlorite in this zone might be depleted in Fe because Fe has been transported into the chlorite–rich proximal alteration.

4.3.3 Chlorite/White Mica Hull Quotient Depth Ratio

Chlorite is a common mineral within the footwall, but white mica is dominant in a larger number of samples (Figure 4.5). This indicates that the unaltered footwall is not chlorite–bearing, and that chlorite–rich regions represent fluid flow pathways.

5. Ages of Igneous and Hydrothermal Activity

A number of techniques are available to measure the date of Earth system processes. Dating using U–Th–Pb isotopes uses decay schemes for which the decay constants are well known: ^{235}U to ^{207}Pb , ^{238}U to ^{206}Pb , and ^{232}Th to ^{208}Pb (Kirkland and Wingate, 2012). This technique has been used to date rocks from the Gindalbie Terrane (Nelson, 1997; Krapež and Pickard, 2010).

5.1 Objectives

The objective of this work was to derive the age of the host rhyolite and hydrothermally altered chlorite through in-situ analysis of monazite and zircon grains. The ages of primary zircons from the footwall rhyolite record the formation of the rhyolite, while the ages of monazite formed during hydrothermal alteration record the timing of deposit formation. Monazite and zircon were identified by SEM–EDS (Appendix 2). Two samples were selected for analysis: A9, one of the least altered rhyolites, which contains zircon of an appropriate size for analysis (Figure 5.1); and A5, a monazite-bearing chlorite-rich rhyolite (Figure 5.2).

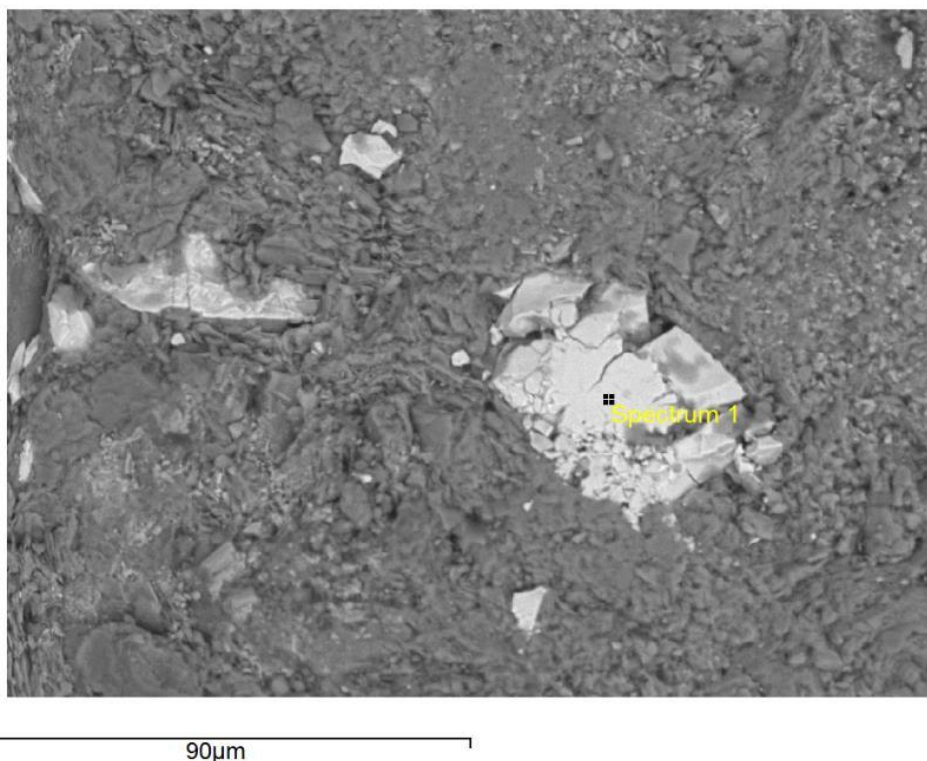


Figure 5.1. SEM–EDS Electron Image of zircon (A9).

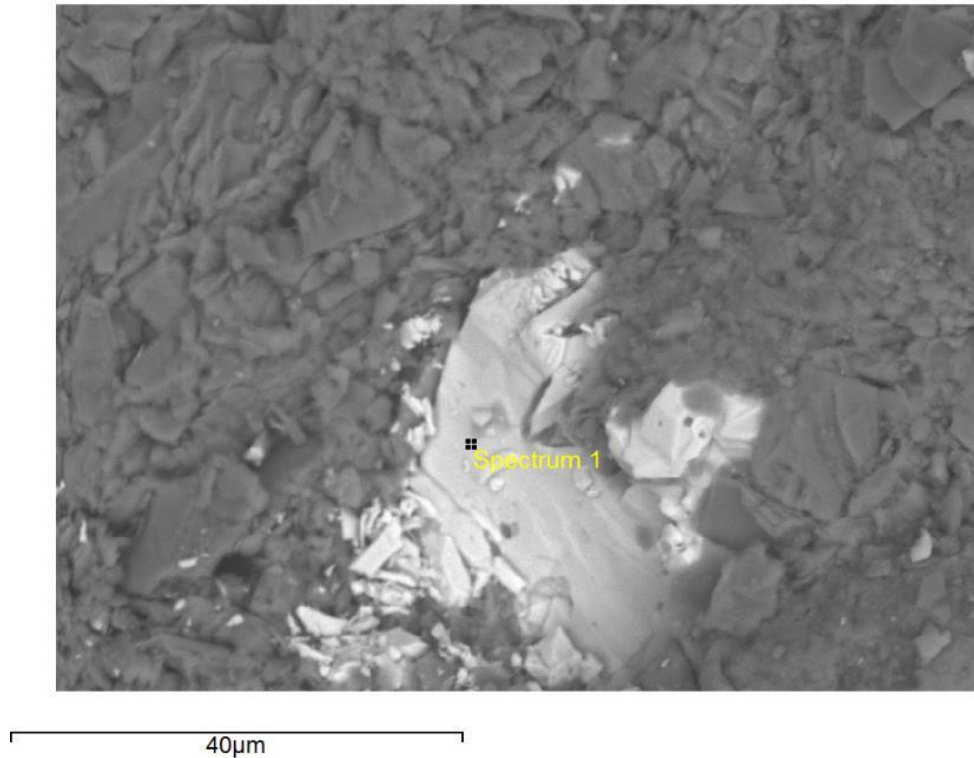


Figure 5.2. SEM–EDS Electron Image of skeletal monazite (Sample A5).

5.2 Results

5.2.1. Zircon

Zircon analysis produced 11 concordant ages, 6 discordant ages, and 3 analyses with evidence of inherited or common Pb (^{204}Pb) (Appendix 3). The mean-square-weighted deviation (MSWD) of the analyses is 1.06, which indicates a high level of precision and confidence in the results. The consistency of the zircon results indicates that the zircons are likely to be igneous; assimilation of zircons from other lithologies would produce more scattered results and multiple populations (Figures 5.2).

Radiogenic Pb might have been rapidly lost during hydrothermal alteration, which would cause dispersion of the affected analyses to the lower right of the concordia line (Figure 5.3). The concordant analyses yield an age, of 2729 ± 24 Ma (95% confidence). The interpretation of the tightly distributed concordant analyses (Figure 5.3), is consistent with the euhedral prismatic crystal habit (Figure 5.1) of the zircon (Yang et al, 2014). Oscillatory zoning was not observed in the analysed zircons, consistent with crystallization within a closed mineral system (Holten et al, 2000).

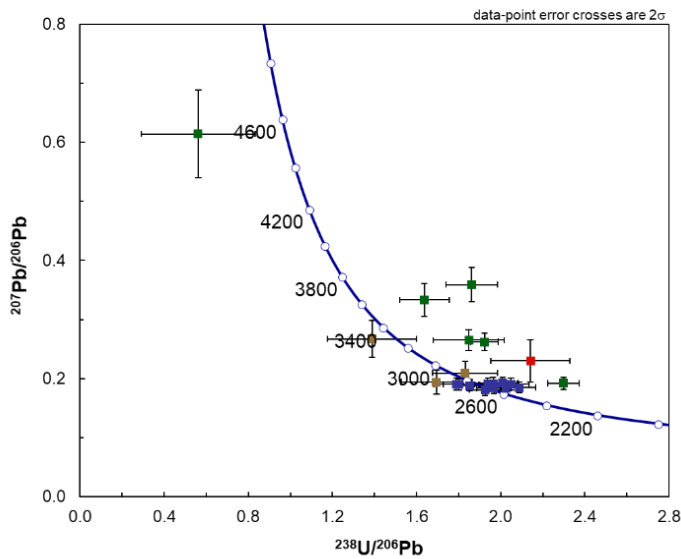


Figure 5.3. U–Pb concordia diagram of zircon analyses. Blue: concordant zircon analyses (interpreted as magmatic); brown: contain inherited or common Pb; green: discordant analyses; Red: monazite (discordant).

5.2.2 Monazite

Only one monazite grain provided useful geochronological results, because the small volume of the grains, the skeletal grain shape, and the presence of common Pb reduced count rates and increased uncertainties. Mineralisation at Bentley is Pb-bearing so the hydrothermal fluids might have been the source of the common Pb. The ^{207}Pb -corrected age of the monazite is ca. 2200 Ma. However, this age is based on assumptions that cannot be tested with the available dataset, so the age is considered to be a minimum model age. Therefore, the age of the monazite is 2730–2200 Ma, where 2730 Ma is the age of the host rhyolite.

5.3 Interpretation

The zircons of the unaltered footwall rhyolite at Bentley are older than previously documented zircons from the Gindalbie Terrane. The age of the Bentley sample (2729 ± 24 Ma) is closer to the age of the Kurnalpi Terrane (2720–2700 Ma) than to existing estimates of the age of Gindalbie Terrane (ca. 2692–2680 Ma: Barley et al, 2008; Belford et al, 2015; Hollis et al, 2015). Samples from Teutonic Bore yielded SHRIMP zircon ages of 2692 ± 4 Ma. A stratigraphic column of the Gindalbie Terrane lithologies is provided by Krapez and Pickard (2016) (Figure 5.4) which has been modified to display the age and emplacement relationship of the Teutonic Bore and Bentley deposit host rocks.

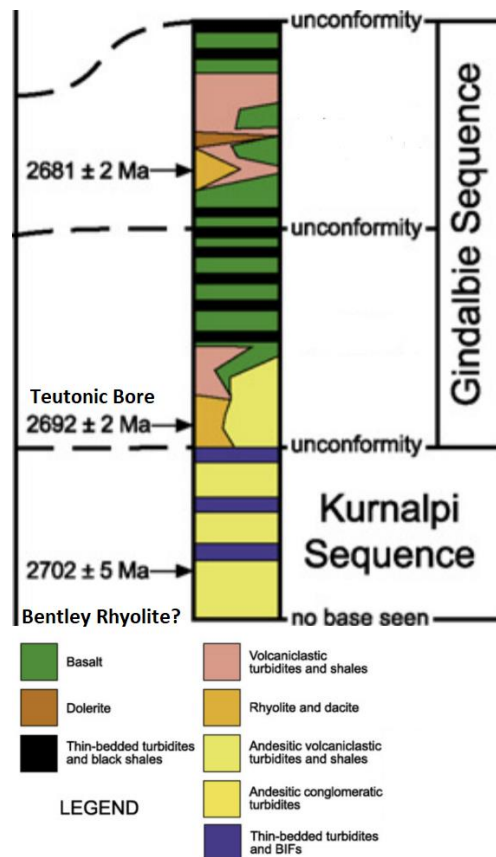


Figure 5.4. Composite sequence stratigraphy of the Gindalbie–Kurnalpi terranes (modified from Krupczak and Pickard, 2016).

The Kalgoorlie Terrane is considered coeval with but geochemically distinct to the Gindalbie Terrane (Kositcin et al, 2008).

The ages of samples from a wide variety of locations within the Eastern Goldfields Superterrane, of which the Gindalbie Terrane is a part, have been determined (Figure 5.5). A number of samples from the Gindalbie Terrane have ages within error of the Bentley age measured in the present study. These include samples E353 (silicified feldspathic volcanogenic sandstone from Bulong), E359 (feldspathic volcanogenic sandstone from Mt Monger) and E360 (feldspathic volcanogenic sandstone from Mt Monger), which yielded ages of 2708 ± 5 Ma, 2708 ± 5 Ma, and 2702 ± 5 Ma respectively. These ages are slightly younger than the age measured for the Bentley protolith, but the rock types are similar to those of the lithologies that host mineralisation at Bentley (Section 2.2.2) and to the “mill rocks” described by Sangster (1972). Further work is needed to determine if these sandstones overlie a rhyolite unit similar to that at Bentley, and if the lithologies that host mineralisation at Bentley are a

similar age to the sedimentary rocks at Bulong and Mt Monger. It has been suggested that the Bulong area is part of the Kurnalpi Terrane (Kositcin et al, 2008).

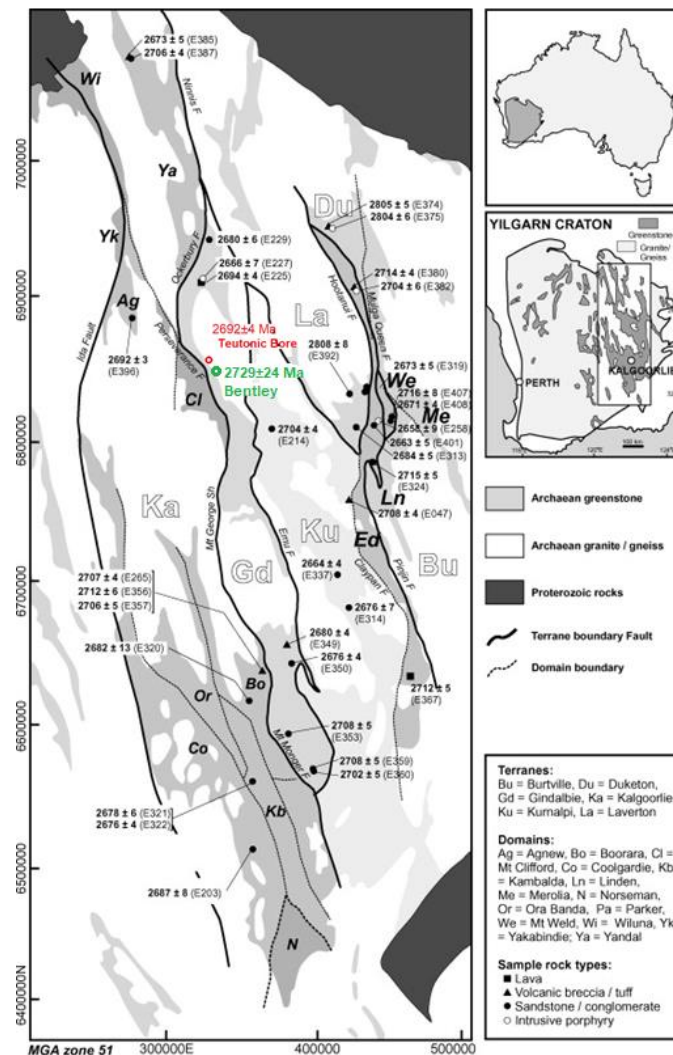


Figure 5.5. Terranes of the Eastern Goldfields Superterrane, and sample locations (modified from Kositcin et al, 2008), showing the Teutonic Bore data (Belford et al, 2015) and the new data from this study for Bentley. Rock descriptions and sample locations are provided in Appendix 4.

The location of other samples within the Gindalbie Terrane, including those at Bentley, are a similar distance from the Ockerberry, Mount George, and Mount Monger faults that form the western boundary of the Gindalbie Terrane. If further work shows that the ages and lithologies of rocks at Mt Monger and Bulong are similar to those at Bentley, then rocks along strike from Bentley to Mt Monger and Bulong might prove prospective for VMS mineralisation.

There are two possible explanations for the disparity between the age of the Bentley sample presented in this study and other Gindalbie Terrane ages:

(1) The lithologies at the Teutonic Bore camp (Figure 2.2) are complex and poorly understood (Belford et al, 2015). Therefore, it is possible that the Bentley rhyolite is an older, previously undated, unit within the bimodal volcanic pile that comprises much of the Gindalbie Terrane. In this case, some Kurnalpi lithologies with ages similar to those of the Bentley rhyolite might be part of the Gindalbie Terrane and be prospective for VMS mineralisation.

(2) The alternative possibility, that the Bentley rhyolite is part of a shared basement to the Gindalbie and Kurnalpi terranes (Kositcin et al, 2008), requires assessment through further geochemical and geochronological analysis. If this hypothesis is proven then regions currently assigned to the Kurnalpi Terrane might form part of the basement of the Gindalbie Terrane, and be prospective for VMS mineralisation.

The 2200 Ma age of the single monazite grain is associated with a large uncertainty because of the high concentration of ^{204}Pb within the monazite. The estimated age of the monazite (2730–2200 Ma) is within error of the age of the footwall rhyolite, and provides only weak constraints on the age of mineralisation at Bentley. Additional monazite analyses might provide tighter constraints on the age of mineralisation. Dating of the dolerites that cross-cut the ore would provide additional constraints on the timing of mineralisation.

6. Discussion

The characteristics of SWIR absorption within the studied footwall to VMS mineralisation are determined by a combination of structural controls, the composition of mineralising fluid, and interactions between fluids and the footwall rocks. The SWIR data can be combined with other geological data to produce an interpretation of the genesis of the Bentley deposit. The SWIR results record the composition and temperature of the mineralising fluids, and map structural corridors related to mineralisation.

The interpretation of the SWIR data provides insights into formation of the Bentley deposit and a guide to the use of SWIR in VMS and other deposit types elsewhere.

6.1 Model Cross Sections based on SWIR data

An interpretive 3D model of alteration at Bentley was created using the SWIR dataset and the Leapfrog Mining software (see section 1.3.2 for methods). A series of cross sections was created to show the variation of the spectral features within the footwall rhyolite. Cross sections were created for the 4145 RL, 3870 RL and 3750 RL mine levels, and for the line of lode of the deposit (189° azimuth, 65° dip) (Figure 6.1).

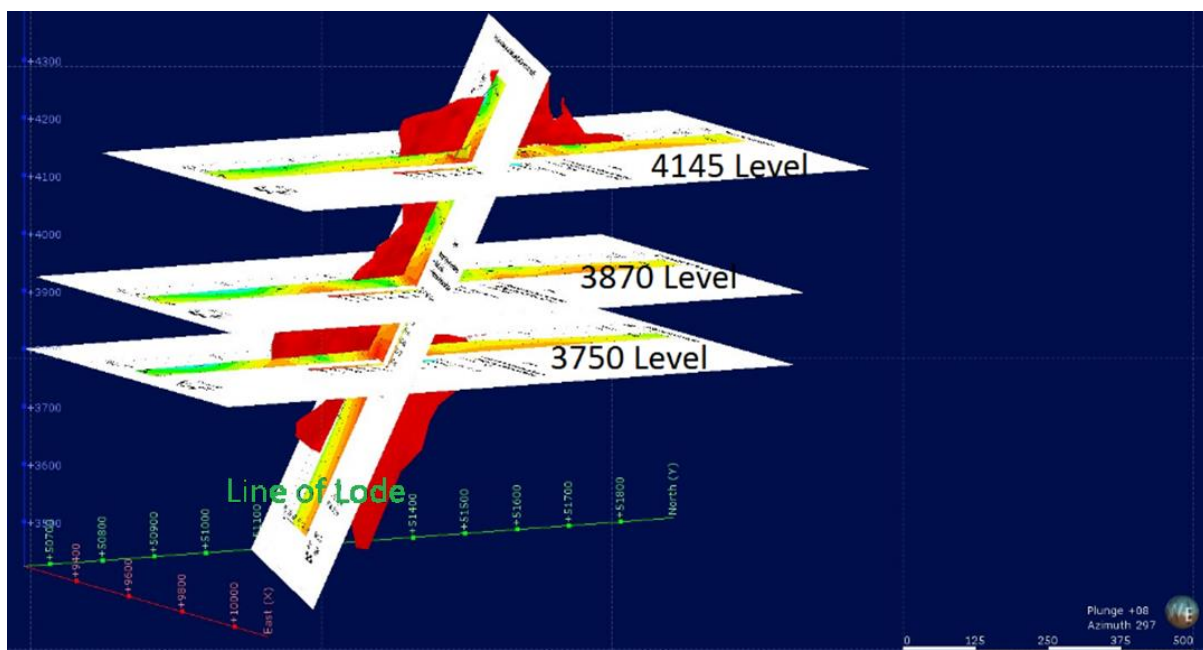


Figure 6.1. Three dimensional visualisation of the locations of the cross sections at 4145 RL, 3870 RL and 3750 RL and along the line of lode. Looking northwest. The main massive sulphide lens (Arnage) is shown in red.

The Bentley footwall SWIR dataset contains ca. 5600 data points (Appendix 5). The vast majority of samples are from within 120 m of the massive sulphide lens. The high sampling density, particularly in and around 4145 RL, enables creation of a detailed representation of the SWIR-sensitive alteration features associated with formation of the Bentley deposit. The data becomes increasingly sparse with increasing depth and with distance from the massive sulphide lens.

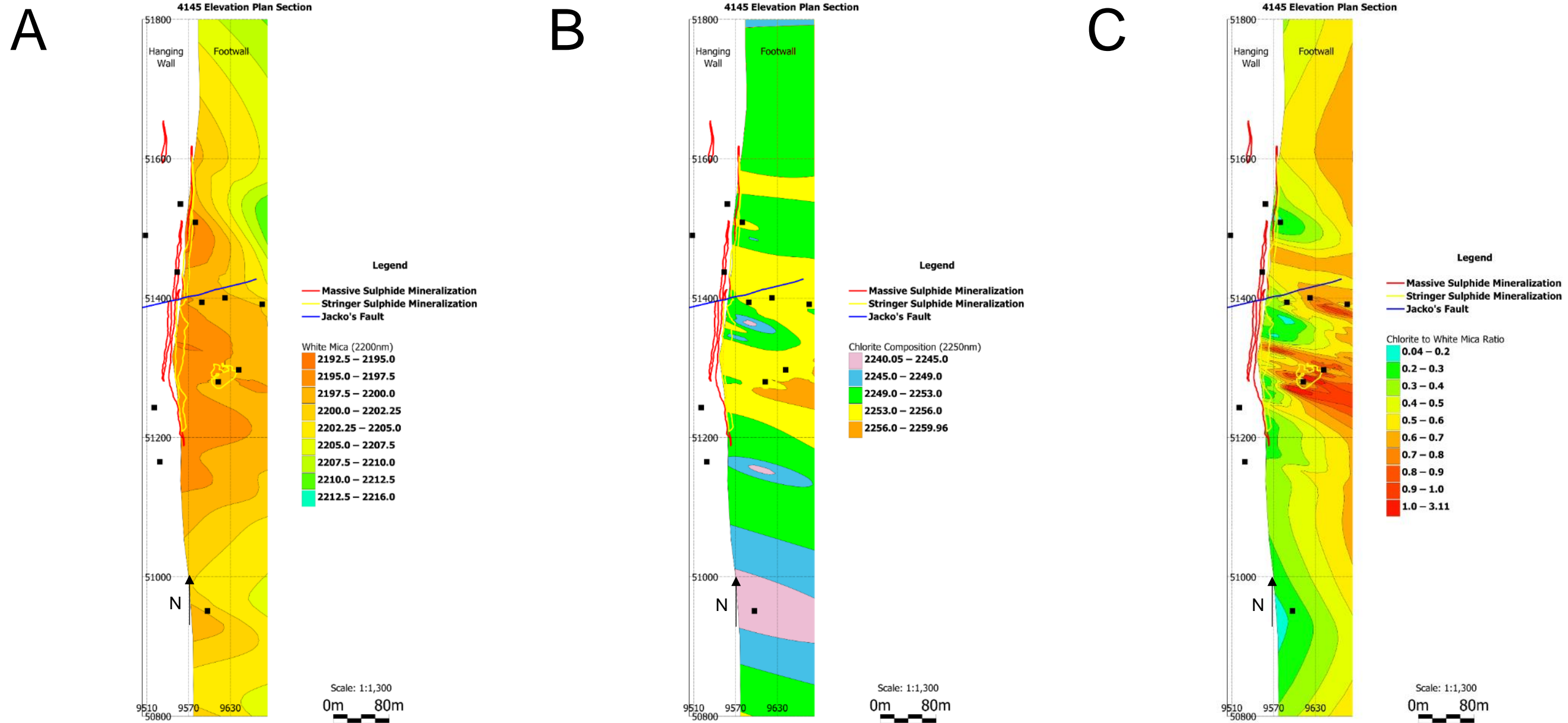
6.1.1 Modelled Alteration on 4145 RL

6.1.1.1 Observations

The 4145 RL level contains the Azure lens of stringer mineralisation. The SWIR sampling density is high around this level, so it is likely that the model represents the alteration well.

Features of note include:

- Regions of Fe-rich chlorite (absorption at <2256 nm) (Figure 6.2B) and white mica (absorption at 2197.5–2200 nm) (Figure 6.2A) associated with the Azure Lens.
- The region of Fe-rich chlorite is associated with a region where the chlorite:white mica ratio is high (>0.9) in the vicinity of the Azure stringer lens (Figure 6.2B–C). A small area of Mg-rich chlorite occurs to the north of this region, close to the massive sulphide lens.
- Regions of Mg-rich chlorite are also present on the periphery of the massive sulphide lens, where they form a halo. Chlorite more distal than this Mg-rich halo is intermediate in composition. The Mg-rich chlorite forms a separate population on the histogram with absorption between 2241 nm and 2244 nm (Figure 4.2).
- The chlorite-dominant samples have a higher Fe content than chlorite in the white mica-dominant samples (Figure 4.2). The 4145 RL samples with a high chlorite:white mica ratio ($2250\text{hqd}/2200\text{hqd} > 0.9$) contain Fe-rich chlorite.
- A broad halo of white mica of higher Al content (<2202 nm) shows a strong association with the massive sulphide ore.



2

Figure 6.2. Plan section of alteration on 4145 RL. Black squares indicate drill-hole pierce points. (A) White mica absorption. (B) Chlorite absorption. (C) Chlorite:white mica ratios.

6.1.1.2 Interpretation

The presence of Fe-rich chlorite proximal to mineralisation is consistent with the observations of Galley et al (2007), who described Fe-rich chlorite close to mineralisation at some deposits within the Bathurst mining camp, New Brunswick, Canada, and with Large et al (1998), who documented Fe-rich chlorite proximal to the ore body at the Roseberry, Hellyer, and Western Tharsis deposits, Tasmania, Australia. These observations contrast with those of the Thalanga deposit, where Mg-rich chlorite occurs close to the ore. Shanks and Thurston (2012) describe spatial differences in the Fe content of chlorite and related Fe-Mg phyllosilicates as a function of the distance to sulphide ore in weakly metamorphosed VMS deposits in Cyprus, Japan, Canada, and Turkey. In these deposits, Fe-rich chlorite occurs in the cores of feeder zones, and Mg-rich chlorite occurs on the margin of the alteration. A similar alteration pattern was described at a modern deposit within the Galapagos rift (Shanks and Thurston, 2012). Metamorphic tourmaline at the metamorphosed deposit at Kidd Creek, Canada, is Fe-rich in the footwall close to the deposit, and Mg-rich at the periphery of the deposit.

The association between abundant Fe-rich chlorite and the economic chalcopyrite stringer mineralisation indicates that the Fe-rich chlorite on 4145 RL formed on a major fluid pathway that led to the massive sulphide lenses.

The SWIR absorption by white mica in samples from the 4145 RL shows a decrease in the wavelength of absorption with decreasing distance to the massive sulphide lens. White mica absorption in the regions closest to the massive sulphide lens occurs at <2197 nm. The formula of muscovite is $K_2Al_4(Si_6Al_2)O_{20}(OH)_4$. Other Al-rich white micas, such as paragonite ($Na_2Al_4(Si_6Al_2)O_{20}(OH)_4$), and Fe- and Mg-rich micas, such as celadonite ($K(Mg,Fe^{2+})Fe^{3+}(Si_4O_{10})(OH)_2$), form a solid solution series with muscovite.

The chemical composition of white mica varies mainly as a result of the Tschermak substitution. In this coupled substitution, tetrahedral Si and octahedral Mg and Fe exchange for Al ($Si_{TET}(Fe, Mg)_{OCT} = Al_{TET}Al_{OCT}$); Jones et al, 2005). Substitution of interlayer K does not affect the absorption features directly, but records changes to Fe and Mg through the relationship between interlayer K and octahedral Mg and Fe (Pontual, 2011). At the Bentley deposit, a reduction in the white mica absorption wavelength represents a reduction in the Fe and Mg content of white mica. These elements are then available to other minerals, such as chlorite. At Bentley, the white mica distal from the main sulphide lens is typically phengitic, white mica close to the main feeder zone is muscovitic, and white mica proximal to the massive sulphide is Al-rich and paragonitic. Similar patterns have been observed at the Western Tharsis, and Highway/Reward deposits, but opposite trends were observed at the Roseberry and Hellyer deposits (Large et al, 1998).

The muscovite in chlorite–dominant samples is a high–Al muscovite (Figure 4.1). This observation is consistent with a relationship between the high–Al muscovite and high temperature feeder conduits within the footwall. The majority of the white mica–dominant samples form a right–skewed population; most of these samples absorb at 2194–2202 nm, typical of intermediate muscovite to high–Al white micas (Figure 4.1). These absorption wavelengths are similar to those measured in the chlorite–dominant samples. It is concluded that absorption at these wavelengths records hydrothermal alteration within the feeder region. The right–skew of the white mica wavelengths in the white mica–dominant samples represents longer absorption wavelengths for the Mg– and Fe–rich white micas (phengitic). These analyses record increasingly phengitic white mica with increasing distance from the massive sulphide lens.

6.1.2 Modelled Alteration on 3870 RL and 3750 RL

6.1.2.1 Observations

The chlorite compositions on 3870 RL (Figure 6.3B), and 3750RL (Figure 6.4B), show similar patterns to chlorite on 4145 RL. However, the model is less detailed because the sampling density was less. Regions of Mg–rich chlorite (>2249 nm) occur at the periphery of the deposit, intermediate to Fe–rich chlorite (>2253 nm) occurs below the massive sulphide lens, and Fe–rich chlorite is uncommon. The regions of Fe–rich chlorite (>2253 nm) are not aligned with regions of high chlorite:white mica ratio (<0.8), in contrast with the observed distributions of chlorite and white mica on 4145 RL.

White mica that absorbs at <1997.5 nm occurs in similar locations to chlorite that absorbs at >2253 nm. However, the distribution of this white mica does not form a v–shape or cone below the massive sulphides, as observed on 4145 RL.

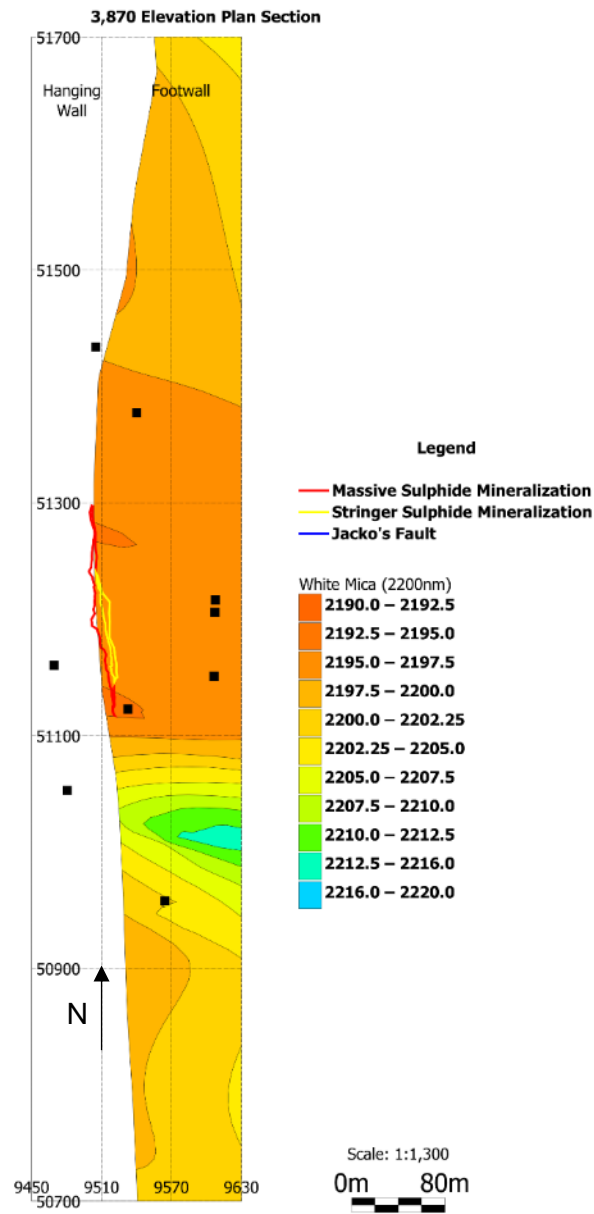
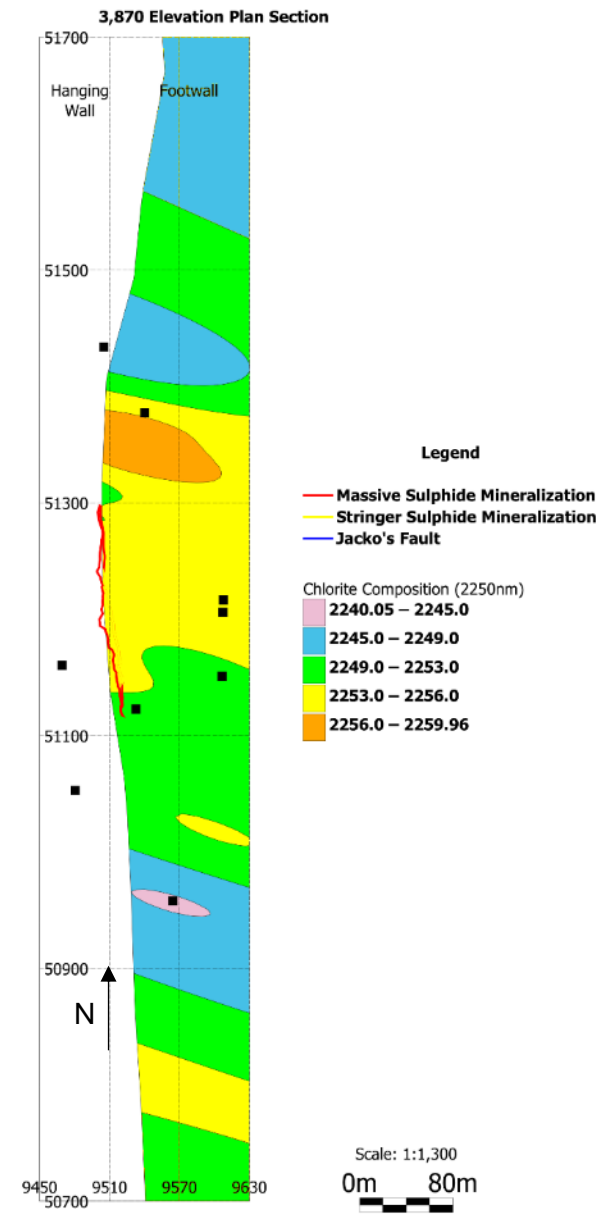
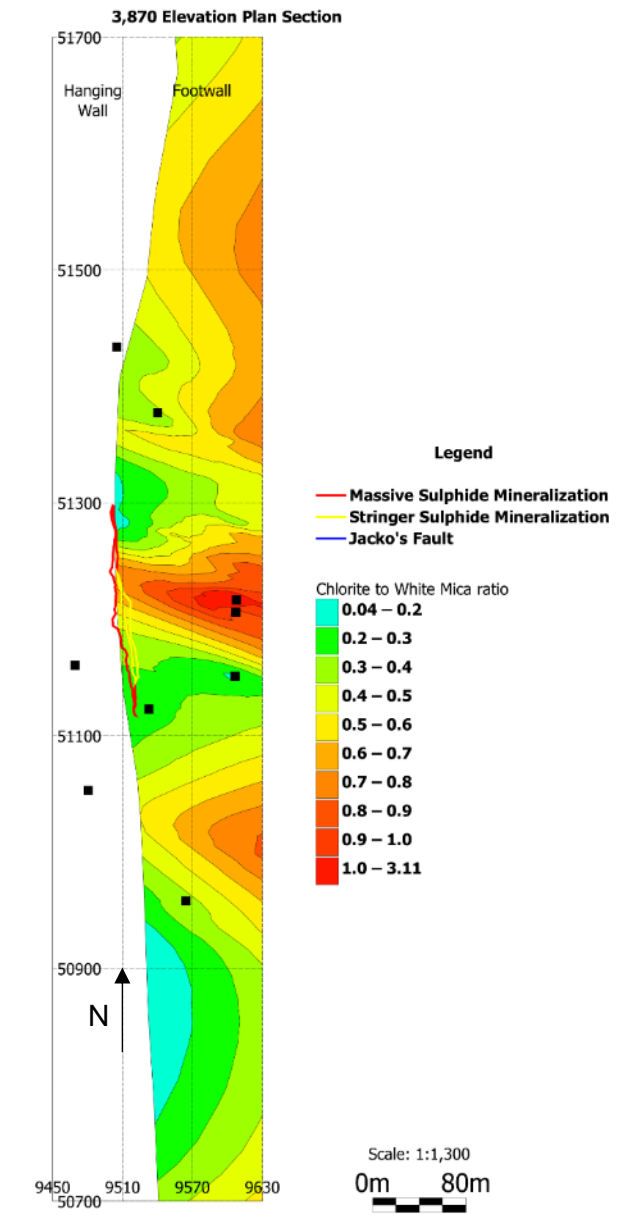
A**B****C**

Figure 6.3. Plan Section of alteration on 3870 RL. Black squares indicate drill-hole pierce points. (A) White mica absorption. (B) Chlorite absorption. (C) Chlorite:white mica ratios.

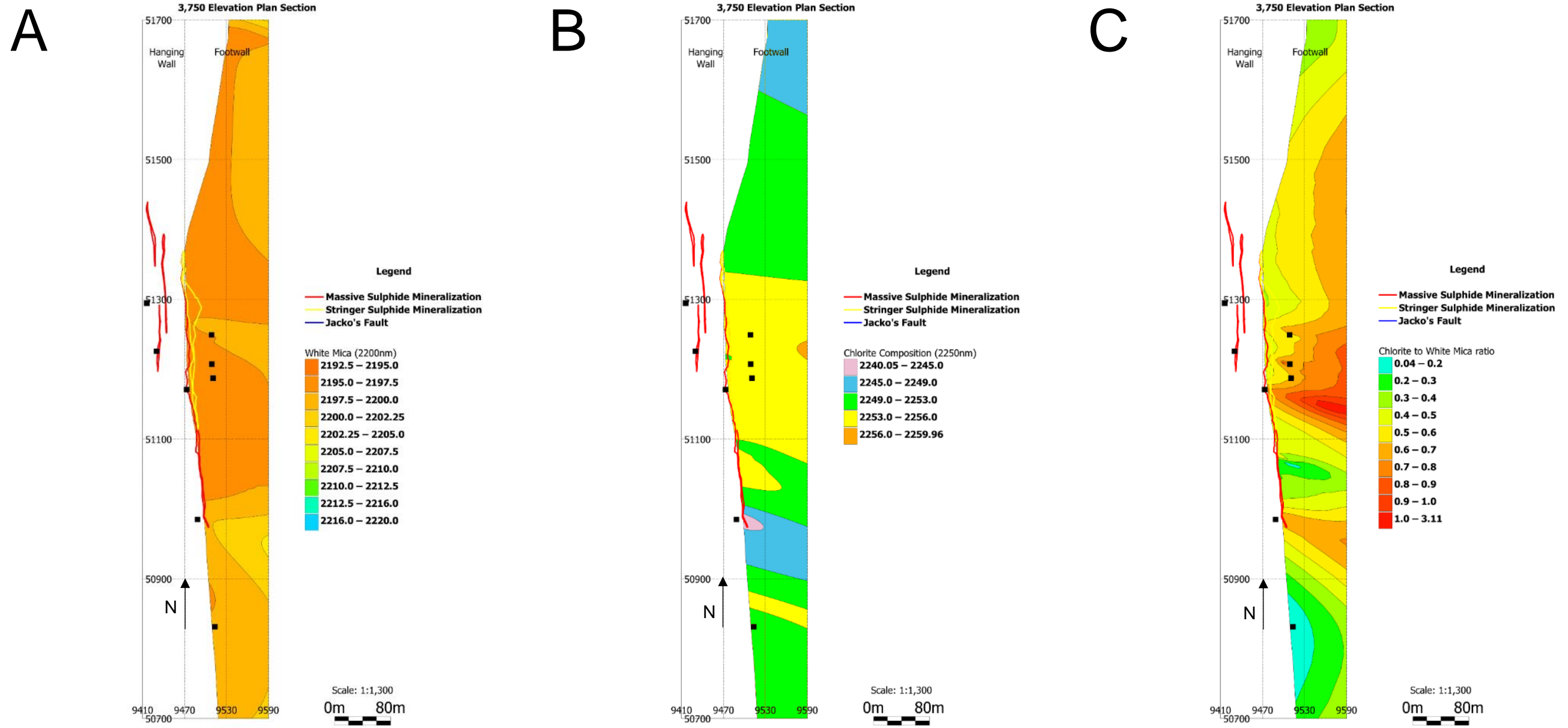


Figure 6.4. Plan Section of alteration on 3750 RL. Black squares indicate drill-hole pierce points. (A) White mica absorption. (B) Chlorite absorption. (C) Chlorite:white mica ratios.

6.1.2.2 Interpretation

The chlorite:white mica ratio on 3870 RL and 3750 RL can be used to map fluid pathways. The chlorite-rich regions trace pathways that lead towards the massive sulphide lens, and these are interpreted as fluid feeder pathways. These features are similar to the feeder pathway identified on 4145 RL. However, stringer sulphides have not been identified on 3870 RL or 3750 RL.

Fe-rich chlorite (>2253 nm) on 3870 RL (Figure 6.3B) and 3750 RL (Figure 6.4B) is associated with the massive sulphide lens, consistent with the spatial distribution of Fe-rich chlorite on 4145 RL. The most Fe-rich chlorites (>2256 nm) are present on 4145 RL and 3750 RL but their spatial extent is not so well defined on 3750 RL. A similar zone occurs on 3870 RL, but the position is not related to ore in the same way as on 4145 RL. The difference in distribution might be an artefact of the different sampling densities.

The regions of Mg-rich chlorite is interpreted as Fe-depleted zones. These regions correspond to regions with low chlorite:white mica ratios (<0.5) and high-Al white mica (>2200 nm). These features are interpreted as typical of regions that are marginal to the most intense hydrothermal activity.

The chlorite:white mica ratios indicate that regions with a higher relative abundance of chlorite (>0.9) occur in the expected position on 3870 RL (Figure 6.3C) and 3750 RL (Figure 6.4C). On 3750 RL, the region of Fe-rich chlorite (>2256 nm) corresponds with the region of high relative abundance of chlorite. On 3870 RL, the region of Fe-rich chlorite does not correspond with elevated chlorite:white mica ratios. The difference might be an artefact of the reduced sampling density on 3870 RL.

White mica absorption on 3870 RL (Figure 6.3A) and 3750 RL (Figure 6.4A) defines a broad zone of high-Al mica (<2197.5 nm). This halo is different to the v-shaped or cone-shaped region of alteration observed on 4145 RL. The difference is attributed to the reduced sampling density on 3870 and 3750 RL.

6.1.3 Modelled Alteration Line of Lode

6.1.3.1 Observations

The chlorite:white mica ratios on the cross section on the line of lode (Figure 6.4C) define three regions where the relative abundance of chlorite to white mica is higher than in the surrounding footwall. Elevated chlorite:white mica ratios occur on 4145 RL, 3870 RL, and 3750

RL. The region of elevated chlorite:white mica ratio on 4145 RL is associated with the Azure stringer lens.

There is a broad halo of medium to Fe-rich chlorite (>2253 nm) (Figure 6.4B) surrounding a region of Fe-rich (>2256) chlorite on 4145 RL, which is associated with a region of high chlorite:white mica ratios (>0.8).

White mica wavelengths display a broad halo of high-Al white mica (<2197.5 nm). White mica associated with the Azure stringer absorbs at 2197.5–2200 nm.

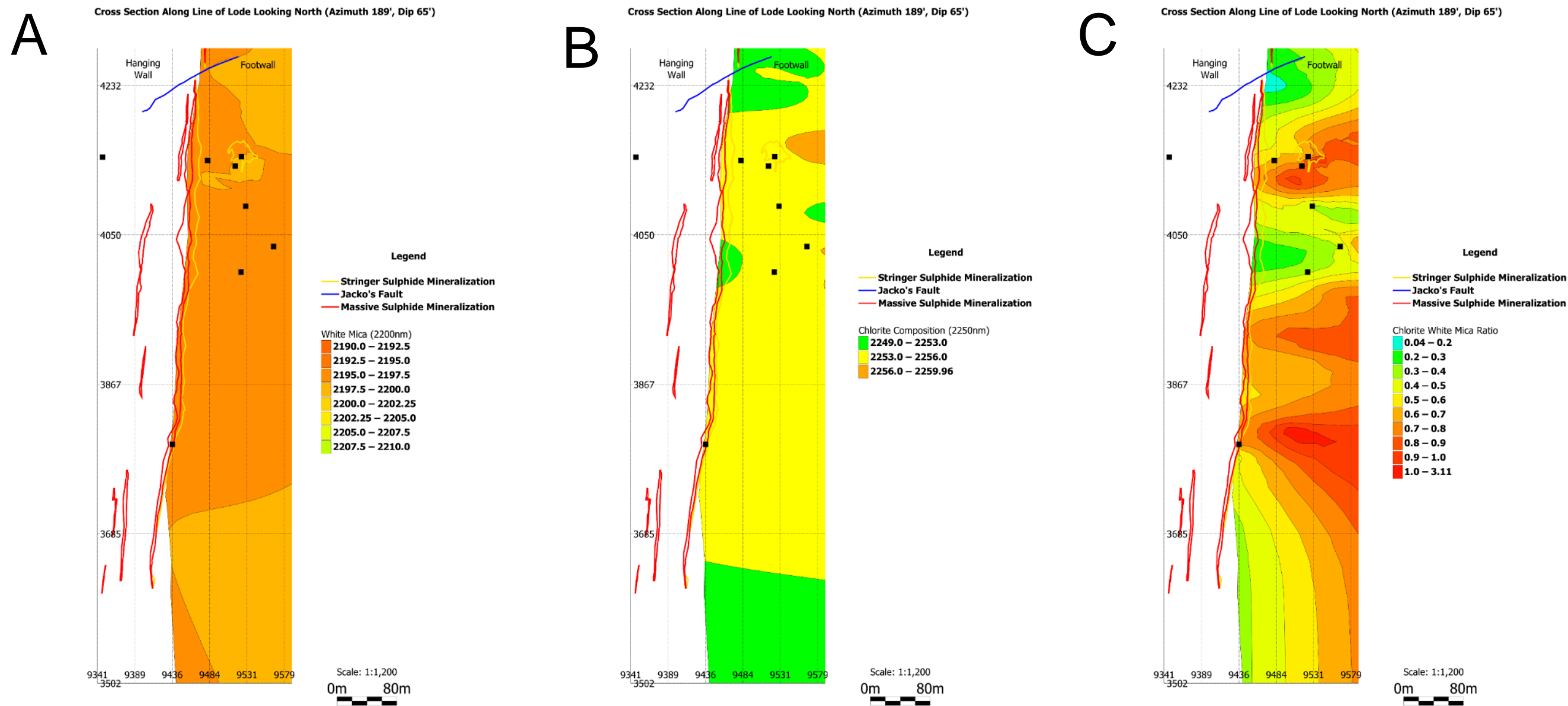


Figure 6.5. Plan Section of alteration on the line of lode. Black squares indicate drill-hole pierce points. (A) White mica absorption. (B) Chlorite absorption. (C) Chlorite:white mica ratios.

6.1.3.2 Interpretation

The region with high chlorite:white mica ratios on 4145 RL coincides with the Azure sulphide stringer (Figure 6.2C). The zone of high ratio (>0.8) appears associated with the Azure lens.

Consistent with the other cross sections, there is a broad halo of Fe-rich chlorite (>2253 nm), and the most Fe-rich chlorite (>2256 nm) is associated with the Azure stringer lens.

White mica absorption defines a broad halo of slightly high-Al muscovite (<2197.5 nm), and a zone of high-Al white mica (2197.5 – 2200 nm) associated with the Azure stringer lens (Figure 4.1). White mica that absorbs at these wavelengths can occur in chlorite-dominant samples, even when the abundance of white mica is low (chlorite:white mica ratio > 0.8). These values are considered diagnostic of the regions that experienced the most fluid flow.

6.2 Alteration Summary

To summarise:

The broad halo of Fe-rich chlorite (>2253 nm) and high-Al white mica (<2197.5 nm) surrounds mineralisation within the footwall and might provide a vector to mineralisation elsewhere.

The chlorite:white mica ratio defines the inferred hydrothermal pathways. Therefore, this parameter might provide a vector for in-mine exploration for stringer mineralisation and trace hydrothermal feeders within the footwall that might lead to stacked massive sulphide lenses. The hydrothermal feeders, which are commonly associated with normal faults, can be mapped to provide insights into fault orientation when structural data is not available.

Regions of Fe-rich chlorite correspond with regions with high chlorite:white mica ratios. The Fe-rich chlorite at core of the alteration is consistent with the conclusions of Galley et al (2007), but is inconsistent with the Mg-rich chlorite at the core of the Hellyer deposit, Tasmania, that is described by Large (1992). Trends in chlorite composition vary among VMS deposits so it does not provide a useful exploration vector unless the deposit mineralogy and alteration are well understood.

A model of the alteration zones at Bentley was constructed, based on the SWIR data (Figure 6.6). The model was constructed on 4145 RL because the data density is highest at this level, and because 4145 RL hosts the Azure stringer sulphide lens.

6.2.1 Alteration Zone 1

Alteration Zone 1 is interpreted as the hottest part of the hydrothermal system that produced the Bentley deposit. This zone is defined by chlorite:white mica ratios >0.8 and the presence of Fe-rich chlorite (>2256 nm). White mica in this zone absorbs at 2197.75–2202 nm, typical of white mica in chlorite-dominant samples (Figure 4.1). This zone is similar to zone two of the Precambrian Bathurst mining camp, Canada (Galley et al, 2007; Figure 1.1), where white mica is present in low abundance. A similar chlorite-dominant zone was identified by Huang et al (2017), at the Honghai VMS deposit, China, based on SWIR data, but the chlorite in that example is Mg-rich.

Alteration of the footwall to VMS is controlled mainly by fluid temperature and the redox state of hydrothermal fluids (Schardt et al, 2001). Mineralising fluids are typically considered to be seawater modified by variable mixing with magmatic water (Ohmoto and Rye, 1974; Bodnar et al, 2014) and through interacting chemically with seafloor rocks (Galley et al, 2007). Hydrothermal convection cells that drive fluids through the host lithologies is driven by heat from synvolcanic intrusions at depth (Shanks and Thurston, 2012). The fluids leach and transport the elements that form ore and alteration minerals.

Without fluid inclusion analysis, the characteristics of the fluid that formed the Bentley VMS must be estimated, using the characteristics of similar examples from the literature. Chlorite-rich zones require temperatures above 200°C to form (Schardt et al, 2001); for example, the core of the Kuruko VMS deposit, Japan, formed at temperatures close to 300°C from ore fluids thought to have had a predominantly seawater origin (Ohmoto and Rye, 1974). At the Windy Craggy deposit, Canada, sulphides formed from fluids at temperatures of ca. 220°C–380°C (Peter and Scott, 1993). At the Turgeon deposit, Canada, chamositic (Fe-rich) chlorite formed in the core of the deposit at 329°C–361°C (Lalonde and Beaudoin, 2015). Therefore, it is inferred that Zone 1 at Bentley formed at temperatures of ca. 290°C–359°C. Further work is required to confirm this conclusion.

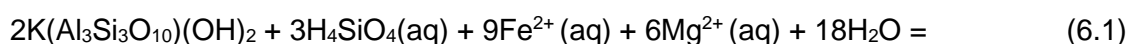
Iron-rich chlorite occurs in the cores of Precambrian VMS deposits, and younger deposits typically have Mg-rich chlorite within their core (Thompson and Thompson, 1996). An exception is provided by alteration forming within the Galapagos Rift, where the core of the VMS deposit contains mostly Fe-rich chlorite (Shanks and Thurston, 2012).

The early oceans were characterised by anoxic, Fe-rich (ferruginous) conditions prior to the rise of atmospheric oxygen at ca. 2.45 Gyr (Rasmussen et al, 2015). It is likely that much of the Fe that formed the Fe-rich chlorite was sourced from ancient seawater, as well as from the surrounding country rock. Fluid inclusion data from VMS deposits indicate that the salinity of the hydrothermal fluids was 0–30 wt.% NaCl (or NaCl+CaCl₂), indicating that the seawater was modified by water-rock interaction, phase separation, addition of magmatic fluid, or a combination of these processes. Fluid inclusion data from some VMS deposits in Archean rocks record salinities higher than modern seawater; these values have been interpreted as evidence of secular variation in seawater chemistry (Bodnar et al, 2014).

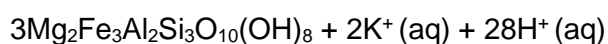
The secular shift from Fe-rich chlorite to the Mg-rich chlorite that is typical of the cores of most modern deposits might be related to the difference between Precambrian and Phanerozoic seawater compositions. The Phanerozoic oceans are typically oxic with low Fe concentrations. Iron in the fluids that form modern VMS combine with S to form sulphides, and

with O to form hematite, magnetite, and/or goethite. Consumption of Fe leaves dissolved Mg available for chlorite formation. This proposal is consistent with observations of drillcore from the active Trans–Atlantic Geotraverse hydrothermal field (TAG). Here, VMS mounds are forming on the Mid–Atlantic Ridge. Hematite is forming with chlorite, quartz, pyrite, smectite, and talc (Shanks and Thurston, 2012).

The characteristic reaction within Zone 1 is conversion of white mica to chlorite:



Muscovite Silicic Acid



Chlorite

(Buschette, 2015). This reaction involves transfer of H⁺ to the reacting fluid, which decreases fluid pH. Muscovite or paragonite forms, rather than chlorite, when the pH is less than 4.5 (Buschette and Piercy, 2016).

6.2.2 Alteration Zone 2

Absorption by white mica is similar in Zone 2 and Zone 1 (2197.75–2202 nm), but chlorite is less relatively abundant in Zone 2 (chlorite:white mica ratio = 0.5–0.8) and the chlorite is less Fe–rich than the chlorite in zone 1 (2253–2256 nm). Sample A5 (Figure 3.5) is typical of this zone. Sample A6 (Figure 3.6) is transitional between zones 1 and 2; the lack of white mica is typical of Zone 1, but the chlorite composition is more typical of Zone 2.

Zone 2 represents a transition between the hotter core of the hydrothermal system (Zone 1) and a cooler outer core where sericite is more abundant and chlorite is more Mg–rich. Sericite generally does not form at temperatures above 300°C (Schardt et al, 2001). The outer chlorite zone, where fluids were cooler, facilitates sericite formation. At the Turgeon deposit, Canada, a clinocllore (Mg–rich) chlorite outer zone formed at 246°C–286°C (Lalonde and Beaudoin,

2015). Zone 2 at Bentley is thought to have formed at a similar temperature, but further work is required to confirm this proposal.

Alteration within zone 2 is transitional between that of the chlorite-rich Zone 1 and white mica-dominant alteration. The transition is gradational rather than sharp and is related to gradients in temperature and fluid composition, and a transition from reaction 1 to reactions 4 and 5.

6.2.3 Alteration Zone 3

Zone 3 is defined by the presence of Al-rich white mica (<2197 nm) and a chlorite:white mica ratio <0.4. Zone 3 is found below the massive sulphide lens, close to the contact between the footwall and the hangingwall.

Sample A4 typifies this zone (Figure 3.3). Primary feldspars are completely replaced by high-Al white mica (2195.39 nm), which is paragonitic in some cases. Paragonite-bearing rocks form in the presence of acidic Na-bearing hydrothermal fluids at temperatures of about 300°C (Hikov, 2014). Therefore, it is likely that the fluids that formed Zone 3 had a lower pH, but similar temperature, to the fluids that formed Zone 1 (ca. 300°C).

Chlorite in zone 3 is Mg-rich (<2253 nm) or Mg-dominant (<2245 nm). The Mg-rich composition of the chlorite is attributed to preferential Fe-depletion. Phengitic white micas form a solid solution between celadonite and muscovite, and typically contain some ferric iron in the octahedral sites of the crystal lattice. Formation of high-Al sericite requires removal of the ferric iron from the crystal lattice. This must occur before Na can exchange for K, or another element with similar atomic radius on the inter-layer cation site. Reduced fluids that contain electron acceptors such as hydrogen sulphide (H₂S) (Schardt et al, 2001), can convert the ferric iron to the more mobile ferrous iron. The ferrous iron can then be transported in a mineralising fluid to be consumed by the formation of Fe-bearing sulphides and chlorite in zones 1 and 2.

Sulphur is a prerequisite for the formation of hydrogen sulphide (H₂S) and sulphide mineralisation. Hot convecting fluids leach sulphides from the country rock near the intrusive heat source (Baker et al, 2001):



Sulphur as S₂ can react with water to form hydrogen sulphide:



Transfer of sulphur from solid phases to the fluid is more complicated than shown in equations 6.1 and 6.2, because of the multiplicity of solid and aqueous sulphur-bearing species.

Convection, advection, or diffusion of fluids from the massive sulphide lens into the footwall might have played a key role in the formation of Zone 3. The interaction of sulphides with fluids might have increased the concentration of hydrogen sulphide in the fluid through reactions similar to (2) and (3). These reactions might have helped to buffer fluid pH and remove ferric iron from phengite, facilitating the formation of high-Al white mica.

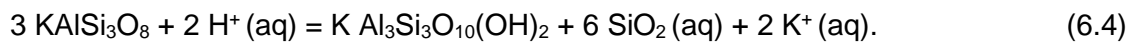
Fluid pH can be buffered by the dissociation of H₂S and by reactions 6.1 and 6.6, and changes in pH might inhibit chlorite formation. Chlorite is generally considered to form at high temperatures (250°C–350°C) and moderate pH (4.5–5.5) (Buschette and Piercy, 2016). The temperature range is similar to that proposed by Hikov (2014) for paragonite formation (ca. 300°C) but the pH range is higher than the pH proposed for sericite stability by Gifkins et al (2005) (4.0–4.5). If the fluids were acidic and H₂S-rich as a consequence of the infiltration of mineralising fluids from the massive sulphide lens into footwall lithologies, then the fluids within Zone 3 might have had a pH lower than that required for chlorite formation. Instead, the fluids might have favoured paragonite formation. Bentley is assumed to have formed below the seafloor, so the extent of interaction between hydrothermal fluids and fresh seawater would be much less than in the case of a VMS deposit that formed on the seafloor. The sub-seafloor setting might have reduced the rate of flow of acidic fluids and trapped heat. If this was the case, then the fluid temperature would be similar to that of the fluids that formed Zone 1, but the pH might have been lower.

6.2.4 Alteration Zone 4

Zone 4 is defined by a chlorite:white mica ratio <0.5, similar to Zone 3. White micas in this zone absorb between 2197–2205 nm, consistent with the presence of muscovite. The chlorite absorption feature is generally at <2253 nm, so the chlorites are less Mg-rich than those in Zone 3. Sample A7 (Figure 3.4) is representative of this zone.

Zones 3 and 4 of this classification correspond to Zone 3 of Galley et al (2007) (Figure 1.1). The difference between the two models is that variation in the Al content of the white micas is taken into account in this model.

In Zone 4, the feldspars are highly altered, phengite is replaced by muscovite, and the rocks are muscovite-dominant. Destruction of orthoclase to form muscovite can be represented by:



Orthoclase Muscovite Quartz

Destruction of albite can be represented by:



Albite Muscovite Quartz
+ 3Na⁺ (aq)

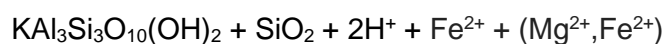
(Gifkins et al, 2005). The alteration of feldspars involves consumption of H⁺ in the fluid, with a consequent increase in fluid pH. An increase in fluid pH might favour chlorite formation, as described for Zones 1 and 2.

Albite destruction releases Na⁺ into the fluid; this Na⁺ might substitute for K⁺ in muscovite to form the paragonite found in Zone 3.

Replacement of celadonite/phengite with muscovite can be represented by;



Celadonite



Muscovite Quartz

Alteration of celadonite to muscovite involves the replacement of Mg and ferrous Fe by Al on the octahedral site and the replacement of Fe³⁺ by Al on the tetrahedral site. The increase in the Al content of the mica is accompanied by a shift from phengite to muscovite; idealised phengite can be represented as $KAl_{1.5}(Mg,Fe)_{0.5}(Al_{0.5}Si_{3.5}O_{10})(OH)_2$ (Mindat.org, 2019). Removal of Fe²⁺ and Mg from the crystal lattice makes these elements available for chlorite formation within Zone 1.

6.2.5 Alteration Zone 5

Zone 5 represents the least altered areas of the deposit and is defined by samples with a chlorite:white mica ratio <0.5, white mica–dominant, and phengitic white mica (>2205 nm). This zone lies outside the main region of hydrothermal alteration and might record regional metamorphism. Samples A8 (Figure 3.1) and A9 (Figure 3.2), which contain unaltered feldspars and large quartz phenocrysts are typical of this Zone. If chlorite were present in this zone then it would be Mg–rich. The phengite in this zone has the highest concentrations of Si, Mg, and Fe. Alteration of the phengite by hydrothermal fluids make these elements available to form quartz (Si), chlorite (Mg, Fe), and, with the addition of S, iron sulphide minerals (Fe).

The presence of Mg–rich chlorite is attributed to the lack of proximity to the intense hydrothermal alteration. In Zone 5, fluids did not liberate ferric iron from the phengite crystal lattice, but were still able to release Mg⁺² to form Mg–chlorite. Therefore, Mg–rich chlorite could have formed, albeit in small amounts, alongside phengite.

A better understanding of the less altered zones around the Bentley VMS might provide insights into the types of alteration expected in different lithologies. Alteration in Zone 5 is subtle, but it could provide a larger target for exploration than the other zones; this is helpful, because the precise location of the mineralisation is less important than recognition of prospective areas, so resources can be focused on those areas.

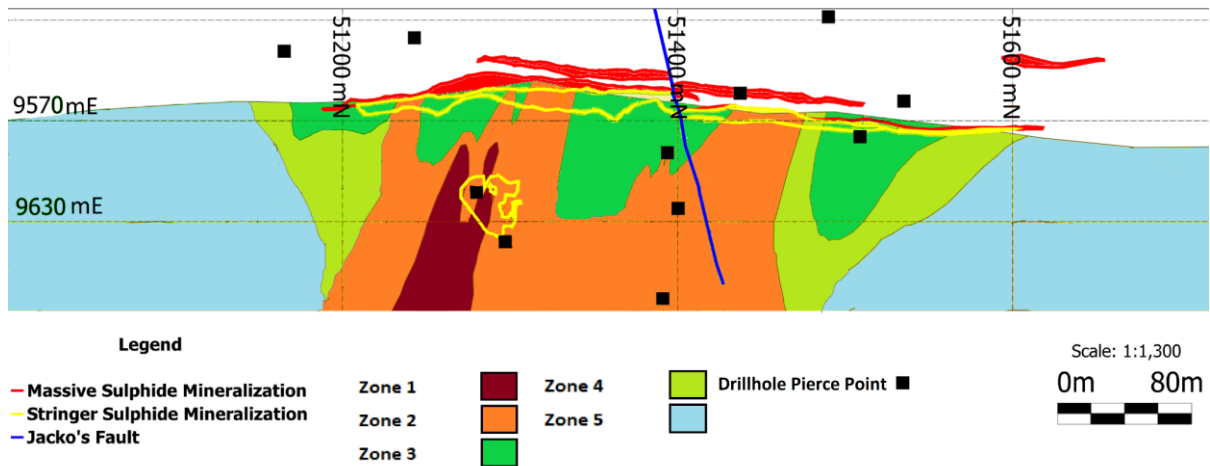


Figure 6.6. Model of alteration at the Bentley Deposit 4145 rL (cross-section).

6.2.6 Further Work

Further work should be undertaken to determine the spectral model's usefulness as an exploration tool.

Zones 1 to 4 provide a potentially large vector to mineralization extending >100m into the footwall from massive sulphide but a similar size along strike, at the 4145 rL. A SWIR criteria with chlorite:white mica ratio <0.5 and white mica of <2205 nm may be a useful tool for regional exploration. Chlorite absorption features <2253 nm may also be useful but due to different VMS systems containing Fe or Mg-rich chlorite within the alteration core it should be treated with caution.

To validate these criteria spectral sampling of any existing exploration holes near Bentley could be undertaken. This would determine whether the current exploration drill spacings used onsite are sufficient to detect these spectral vectors. Similarly, this could then be done with exploration drilling for the Jaguar and Teutonic Bore deposits to further determine usefulness.

The principal limitation of the model of alteration at Bentley is that the model only describes alteration in the footwall. The insights gained through this work suggest that the Bentley deposit formed below the seafloor. Therefore, the hangingwall might have been emplaced prior to mineralisation and might have undergone hydrothermal alteration (Gifkins et al, 2005). Further study might lead to the discovery of mineralised hydrothermal conduits within the younger hangingwall lithologies.

6.3 Structural Control of Fluid Flow

The primary control on the geometry of hydrothermal alteration is the propagation of normal faults. Faults are often described and represented as planar features, but this is rarely the case.

Detailed studies of normal fault propagation can provide useful insights. Such studies are scarce, particularly in volcanic rocks because it is rare to find good exposures of fault systems associated with extensional regimes in these lithologies. Martel and Langley (2006) and Kaven and Martel (2007) describe the propagation of the Hopena normal fault through extrusive basalts on the Koaie fault system at the Kilauea volcano, Hawaii (Figure 6.7).

Features created by the formation of normal faults within volcanic rock include antithetic faults, footwall fissures, and rock-filled cavities (Figure 6.7). These features create high hydraulic conductivities, similar to those of gravel, which can be maintained even if the faults are overlain by lava or, in the case of Bentley, by volcanoclastics (Martel and Langley, 2006). The high hydraulic conductivity is particularly relevant at deposits such as Bentley that formed below the seafloor. Brecciated cavities facilitate the formation of stringer sulphide mineralisation such as the Azure lens (Figures 2.7, 2.10), with massive sulphides above the stringers or close to the seafloor.

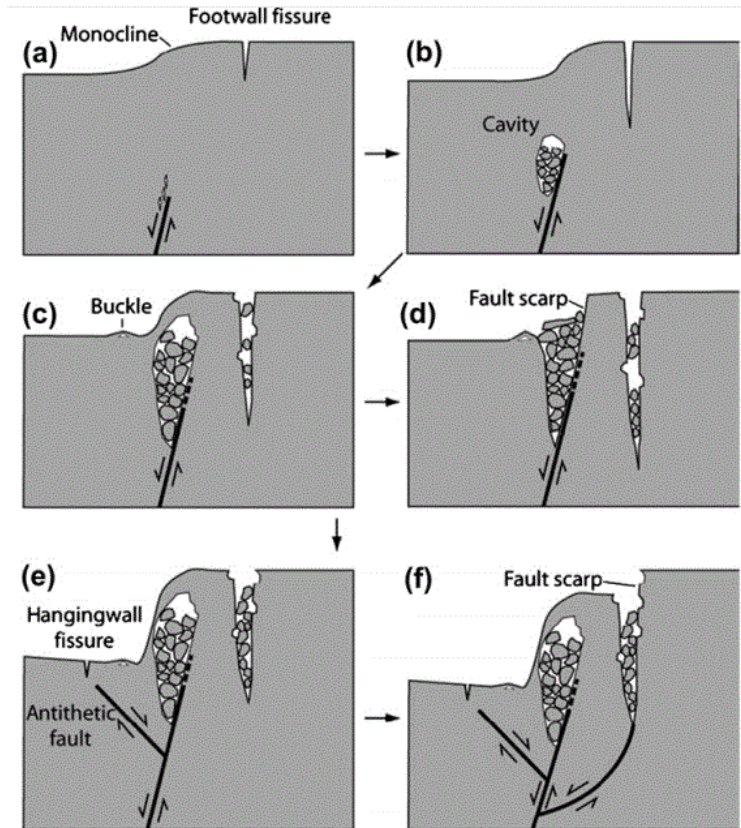


Figure 6.7. Conceptual model of the propagation of a normal fault to the surface (in basalt). (modified from Martel and Langley, 2006) (a) Slip at depth yields a broad monocline, which opens pre-existing cooling cracks at the surface, and fractures near the fault tip. (b) As the fault tip propagates towards the surface, surface fissures widen and deepen, and cavities open on the hangingwall near this tip (hydraulic conductivities increase as it evolves). (c) A buckle begins to develop on the hangingwall near the base of the scarp with the cavity growing to the extent that a monoclinical bridge forms. (d) The fault breaches the surface and the monoclinical bridge collapses. (e) The central limb of the monocline becomes progressively steeper if the monoclinical bridge does not collapse. (f) The fault links with the gaping fissure, transferring the monocline to the fault footwall.

Many or all of the structures typical of normal faults (Figure 6.7), and shown by the evolving Hopena normal fault system with its associated fractures, displacement and buckles (Figure 6.8) should be present at the Bentley deposit. The approximate current width of the Bentley deposit massive sulphide lenses is likely to be similar to the width of the features that formed on normal faults at Bentley. Such structures and cavities increase the rock porosity, facilitating infiltration and circulation of hydrothermal fluids.

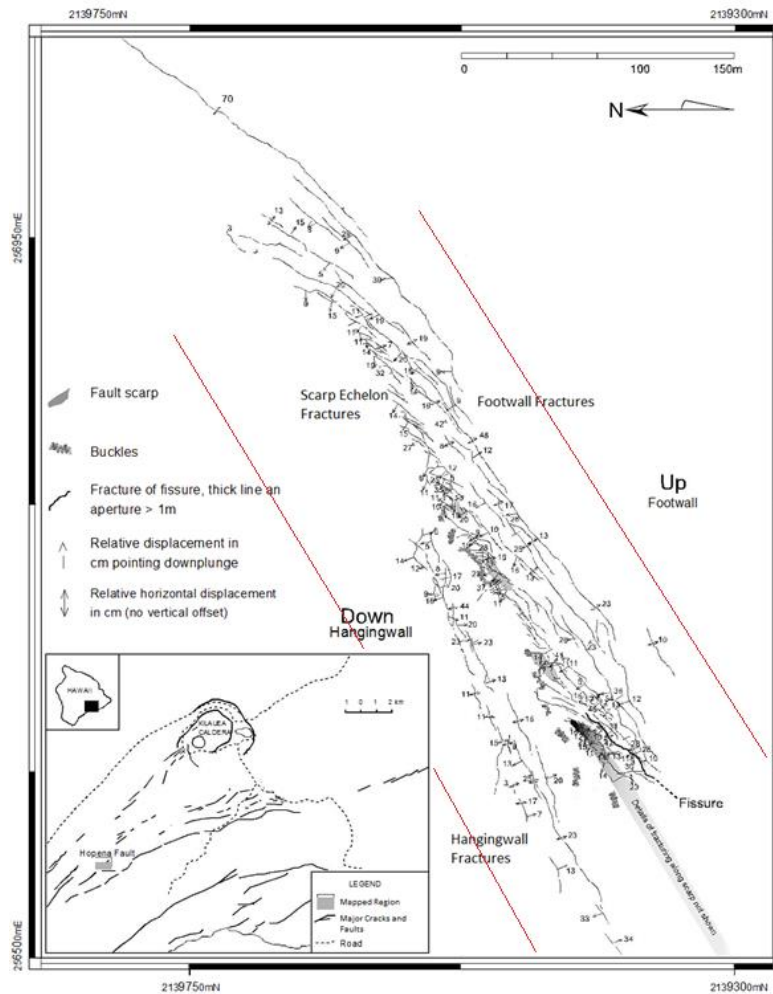


Figure 6.8. Structural map of the northern fork of the Hopena Fault showing the approximate width of the Bentley deposit (red lines). Modified from Kaven and Martel (2007).

Features within the three dimensional model based on the chlorite:white mica ratios are consistent with the characteristics of structures related to normal faulting (Figure 6.9). Chlorite:white mica ratios greater than 0.65 are shown in blue to highlight chlorite-rich zones that intersect the massive sulphide lens (Figure 6.9; light blue). Larger chlorite-rich regions are associated with smaller ancillary chlorite-rich regions that are interpreted as smaller antithetic faults and fissures that were associated with the main normal fault plane. These features can be seen best above 4145 RL, where sampling density is higher, and are less

common at the lower levels where the sampling density was sparse. The width of the region defined by the high chlorite:white mica ratios is approximately 150 m (Figure 6.9), which is the same as the width of the Koae fault system (Figure 6.8). The features highlighted in Figure 6.8 also show the trend of the structural feature that hosts mineralisation, which provides a vector for exploration.

Much of the current literature on VMS deposits provides a simplistic view of the structural controls on footwall alteration (e.g., Figure 1.1). In reality, the geometry of fluid flow is likely to be complicated. Idealised conceptual models such as that of Figure 1.1, show a single fluid conduit within an alteration zone; in reality there are likely to be multiple conduits (Figure 6.9). It is likely that not all of the conduits host economic stringer mineralisation, but further mineralisation might be discovered if the conduits are identified and targeting with drilling.

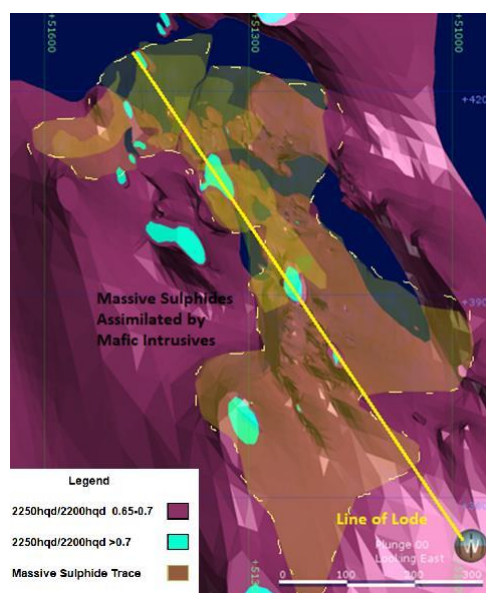


Figure 6.9. Cross section of the Bentley deposit cross-section looking east. Partly transparent features are the economic massive sulphide lenses, which are overlaid on the surface defined by interpolated chlorite:white mica ratios of 0.65–0.7. The blue zones indicate regions where the chlorite:white mica ratios is greater than 0.7, and that intersect the massive sulphide lens.

Other fault-related structures can be interpreted within the Bentley alteration model (Figures 6.7, 6.10). It is possible that a cavity existed in the present location of the Azure stringer sulphide lens, that Zone 1 lies on a partially formed major fault plane, and that Zone 2 traces the location of fissures and antithetic faults. These structures might not be fully developed, but the SWIR data suggest that they were able to focus the mineralising fluids.

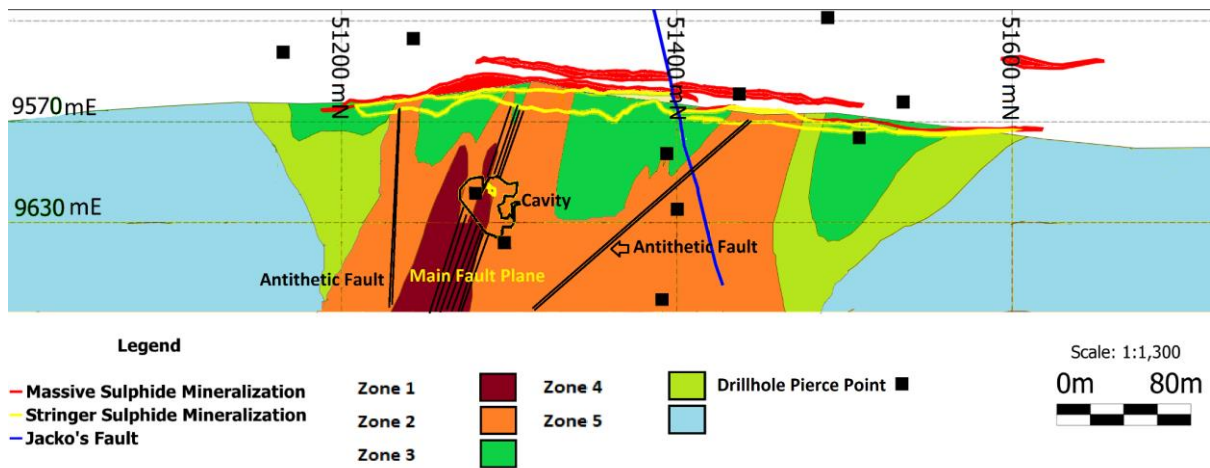


Figure 6.10. Alteration zones in plan section at the Bentley deposit on 4145 RL, with interpreted fault structures.

6.4 A Genetic Model for the Bentley Deposit

The Bentley VMS deposit is interpreted to have formed below the seafloor, based on evidence from a drive face in the Brooklands ore lens (Figure 2.8). The side of the face that lies within the hangingwall consists of shale with minimal brecciation. The contact between the Brooklands lens and the shale is sharp, and there are almost no sulphides, economic or otherwise, within or structurally above the contact. Therefore, the sulphides formed mainly within the volcanoclastics, and the black shale formed an almost impenetrable barrier to the mineralising fluids when the deposit formed and during any later deformation and remobilisation of the ore. The sharp boundary is consistent with the conclusions of Large (1992) and Tornos et al (2015), that subsea replacement deposits are well developed in reactive and/or porous rocks such as volcanoclastic facies, and negligible in fine-grained sediments such as shales. If Bentley formed as a mound style deposit, then ore breccias would be present. Models of VMS deposit formation that involve fine-grained sediments, such as the brine pool or regionally anoxic seafloor models (Tornos et al, 2015) predict sulphides and massive sulphides within the fine-grained sediments.

6.4.1 Footwall Rhyolite

The Bentley footwall rhyolite extruded onto the seafloor within an island–arc setting at 2729 ± 24 Myr (Figure 6.11A). The rhyolite consists of a fine–grained quartzo–feldspathic matrix that contains common quartz and rare feldspar phenocrysts. The feldspar phenocrysts are euhedral, which indicates that the melt was partially crystallised prior to extrusion onto the seafloor. The quartz phenocrysts may record modification of crystallised rhyolite that solidified upon extrusion onto the seafloor or reworking of a deeper rhyolite unit. The rhyolite overlies a transitional basalt (calc–alkaline to tholeiitic) and an andesite that occurs to the east of the massive sulphides (Figure 2.2). It is not clear if sediments and volcanoclastics were intercalated with these lithologies. If they are present, then they might host sulphides or stacked lenses. Diamond drilling through the rhyolite along the strike of Zone 1 might reveal if this zone intercepts lithologies that host economic mineralisation. However, this has not been tried; the current diamond drilling program has drilled through the hangingwall into the footwall.

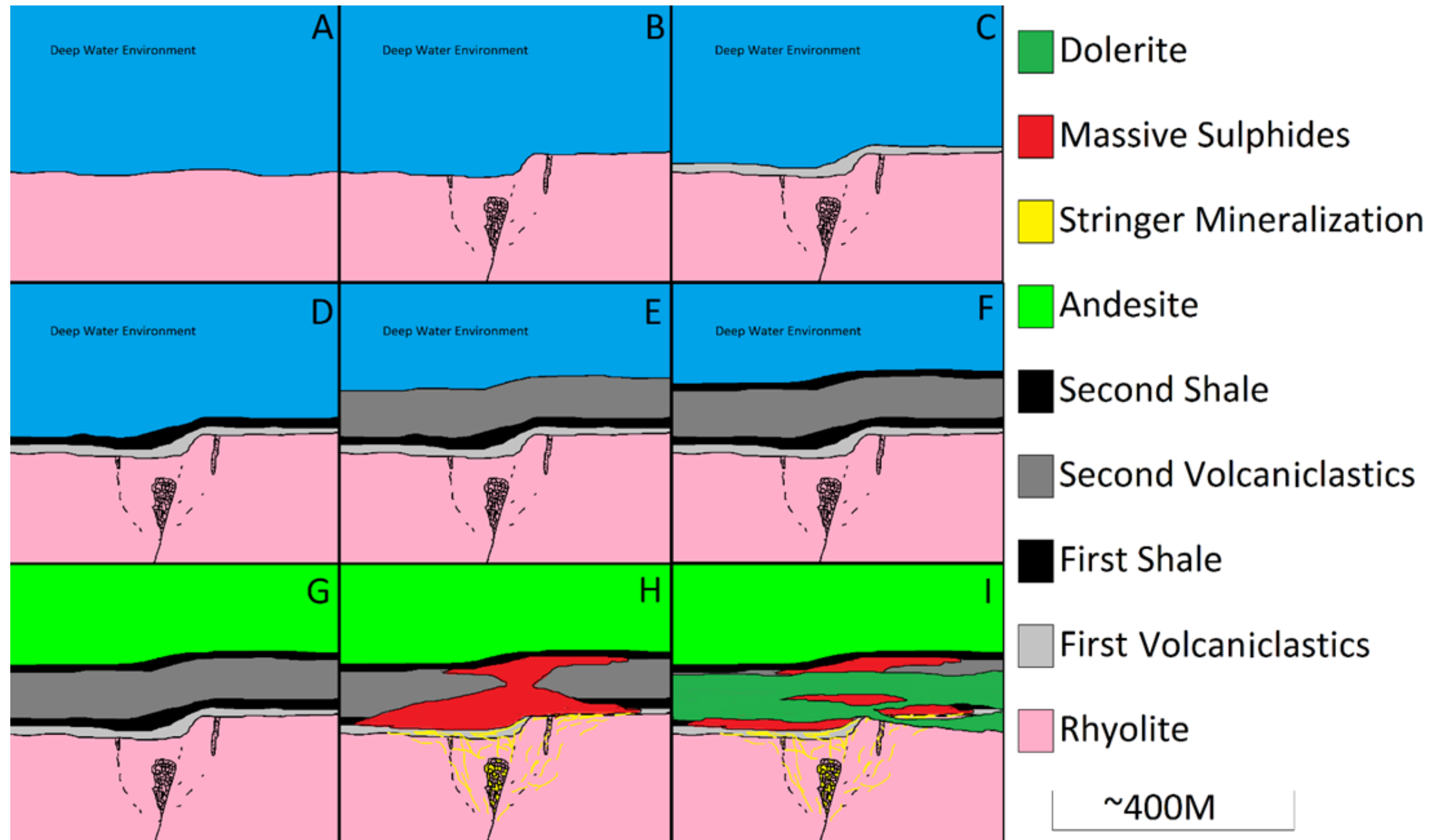


Figure 6.11. Conceptual model of the formation of the Bentley Volcanogenic Massive Sulphide deposit (4145 RL). (A) Formation of extrusive rhyolites on the seafloor within a back-arc environment, above an as yet unknown basement. (B) Formation of monocline as a normal fault propagates towards the seafloor, with consequent formation of breccia-filled cavities on secondary faults that increased hydraulic conductivity. (C) Silicic volcanoclastics were deposited above the rhyolite. (D) Graphitic and sulphidic shales formed during a respite in volcanic activity. (E) Formation of further volcanoclastics, possibly as one or a number of large subaqueous mass flows. (F) A second black shale formed during a hiatus in volcanic activity. (G) Eruption of an extrusive andesite intercalated with volcanoclastics and overlain by a series of extrusive andesites and basalts that transition from calc-alkaline to tholeiitic compositions. (H) Mineralising hydrothermal fluids travel along the master fault to the void created by rock milling within the fault. The fluids continued through the minor fractures within the rhyolite to the volcanoclastic and shale units. The porous volcanoclastics facilitated the passage of mineralising fluids, but contact between the fluids and the low porosity shales promoted precipitation of the Arnage and Brooklands lenses. (I) Tholeiitic dolerites intruded along the sedimentary and volcanoclastic horizons.

6.4.2 Normal Faulting

Normal faulting occurred after eruption of the rhyolite (6.11B). The faulting created fault planes, cavities, fissures, and a monocline feature (Figures 6.7,). Hydrothermal fluids circulated through the voids and fractures, which determined the geometry of alteration and sulphide mineralisation.

The majority of faulting is likely to have occurred prior to consolidation, based on the slight thickening of volcanoclastics and sediments in the fault/mineralisation zone. There is however, minor fracturing observed within the host lithologies indicating that minor fault movement may have occurred post consolidation (Figure 6.12).



Figure 6.12. Variable grained volcanoclastics (fine grained within coarse grained) interpreted to have fractured pre-mineralization. Diamond drill-hole BUDD078 @ 61.1m. Sulphides are pyrite and chalcopyrite (Core width is 50mm).

It is proposed that the structure that hosts the Azure stringer mineralisation (Figure 2.10) on 4145 RL is a cavity formed during normal faulting (Figure 6.7).

6.4.3 First Volcaniclastics

Arenites, volcaniclastics, and sandstones overlie the rhyolite. These units are thought to represent a period of felsic volcanism (Figure 6.11C). Mineralising fluids silicified these units, but prior to silicification the volcaniclastics might have provided a permeable layer that facilitated deposition of the massive sulphide lens within the early volcaniclastics. This unit hosts the Arnage lens (Figure 2.9).

6.4.4 First Black Shale

After deposition of the first volcaniclastics (Figure 6.11C), there was a cessation in volcanic activity and a bedded black shale unit was deposited (Figure 6.11D). This unit would have been consolidated at the time of sulphide mineralisation, based on the evidence that the black shale formed a capping unit that forced the fluids to move horizontally.

6.4.5 Second Volcaniclastic

A second volcaniclastic unit records recommencement of felsic volcanic activity (Figure 6.11E). The second volcaniclastic unit hosts the Brooklands lens (Figure 2.8).

6.4.6 Second Black Shale

The second period of felsic volcanism was followed by a cessation of volcanic activity and deposition of a second black shale unit (Figure 6.11F). This black shale, like the early black shale, presents a boundary to the massive sulphide mineralisation of the Brooklands lens (Figure 2.8).

6.4.7 Andesite

After formation of the second black shale, a period of extrusive volcanic activity formed the andesite hangingwall (Figure 6.11G). This unit lies beneath a tholeiitic basalt unit and other andesites.

6.4.8 Mineralisation

After eruption of the andesite and emplacement of at least some of the hangingwall lithologies, the sediments and volcanoclastics were consolidated. Mineralising fluids driven by an unknown source passed through the normal fault and infiltrated the host lithologies, where they deposited two massive sulphide lenses beneath the two impermeable black shale units (Figure 6.11H).

The location where the fluids passed through the first black shale to form mineralisation below the second black shale has not been found. The normal fault likely continued to develop after consolidation, and this would have allowed fluid access to the later shale. However, consolidation requires burial, so the andesite must have been emplaced prior to consolidation, and in this case the normal fault would be expected to have passed through the andesite, producing fractures and fluid ingress. There is no observed evidence of fluid flow or mineralisation in lithologies younger than the later volcanoclastic unit, which has a well-defined sharp contact with the massive sulphide lens (Figures 2.8, 2.9). Evidence of consolidation prior to mineralization can be observed as minor fractures within the host horizon (Figure 6.12). Relic volcanoclastic and shale lithologies remaining intact within the mineral deposit are diagnostic of a sub-seafloor replacement VMS, with a lack of any “chimney” breccia being consistent with this interpretation (Doyle and Allen, 2003).

6.4.9 Intrusion of Dolerites

After mineralisation, the mineralised horizon was intruded by dolerites (Figure 6.11I), which cut two ore horizons to form the Brooklands (Figure 2.8), Arnage (Figure 2.9), Mulsanne (Figure 2.11) and Comet lenses (Figure 2.3). The dolerites have assimilated parts of the sequence and might have removed evidence that showed how fluids entered the host package. Minor amygdales at the upper contacts and evidence of crystal settling towards the bottom suggest that intrusion occurred prior to inversion of the stratigraphy by regional deformation.

7. Conclusions

The Bentley VMS deposit formed below the seafloor within a felsic volcanoclastic unit that overlies a 2729 ± 24 Ma porphyritic rhyolite footwall unit. At least two massive sulphide lenses formed within the host lithologies. The lenses are capped by beds of sulphidic black shale. The host lithology was intruded by dolerite dykes that split the sulphide lenses into smaller lenses.

Short Wave Infrared spectroscopy was used to investigate the compositions of chlorite and white mica at Bentley and to estimate their relative abundance within the deposit footwall. The data were used to trace the pathways followed by mineralising fluids, which correspond to areas of stringer mineralisation. The fluid pathways host Fe-rich chlorite; chlorite elsewhere is Mg-rich.

The composition of the white micas becomes more Al-rich in the vicinity of the fluid flow pathways and even more Al-rich beneath the massive sulphide lens. Increases in Al are associated with a loss of Si, Fe, and Mg from the white mica as the mica alters from phengite to muscovite to Al-rich white mica.

The white mica SWIR features provide a convenient way to recognise fluid flow and alteration. However, the relative abundance of chlorite to white mica is the most useful proxy for mineralising fluid pathways at Bentley, and elsewhere, because it is not sensitive to local geochemistry or the conditions of mineralisation. Major fluid pathways within VMS systems are always chlorite-rich, with little to no white mica, regardless of the footwall composition. The chemical composition of white micas and chlorite within a VMS footwall can be influenced by the composition of the protolith, but their relative abundance is primarily determined by their location within the feeder zone. At Bentley, the Azure stringer mineralisation occurs within a region where the chlorite:white mica ratio is high. This region forms a fluid pathway towards the massive sulphide lens.

The present study provides a framework that can be used to create models for other VMS systems, and to use SWIR to interrogate minerals associated with other hydrothermal deposit types.

8. List of References

- Baker, D. R., Barnes, S., Simon G., Bernier, F., 2001, Fluid transport of sulphur and metals between sulphide melt and basaltic melt, *The Canadian Mineralogist*, Vol 39 (2), pp 537–546.
- Barley, M.E., 1998, Archaean volcanic-hosted massive sulphides, *AGSO Journal of Australian Geology and Geophysics*, Vol 17(4), pp 69–73.
- Barley, M.E., Brown S.J.A., Krapez B., Kositcin, N., 2008, Physical volcanology and geochemistry of a Late Archaean volcanic arc: Kurnalpi and Gindalbie Terranes, Eastern Goldfields Superterrane, Western Australia, *Precambrian Research*, Vol 161, pp 53–76.
- Belford, S.M., Davidson, G.J., McPhie, J., Large, R.R., 2015, Architecture of the Neoproterozoic Jaguar VHMS deposit, Western Australia: Implications for prospectivity and the presence of depositional breaks, *Precambrian Research*, Vol 260, pp 356–377.
- Blatt, H., Tracy, R.J., Owens, B.E., 2006, *Petrology: Igneous, Sedimentary, and Metamorphic*, W. H. Freeman and Co., New York, 3rd Ed., pp 486–489.
- Bodnar R.J., Lecumberri-Sanchez P., Moncada D. and Steele-MacInnis M, 2014, Fluid inclusions in hydrothermal ore deposits. In: Holland H.D. and Turekian K.K. (eds.) *Treatise on Geochemistry*, Second Edition, Vol 13, pp 119–142.
- Buschette, M.J., 2015, Hydrothermal alteration and lithogeochemistry of the Boundary volcanogenic massive sulphide deposit, central Newfoundland, Canada, Master of Science, Department of Earth Sciences, Memorial University of Newfoundland.
- Buschette, M.J. and Piercey S.J., 2016, Hydrothermal alteration and lithogeochemistry of the Boundary volcanogenic massive sulphide deposit, central Newfoundland, Canada, *Canadian Journal of Earth Sciences*, Vol 53, pp 506–527.
- Canet, C., Arana, L., González-Partida, E., Pi, T., Prol-Ledesma, R.M., Franco, S.I., Villanueva-Estrada, R.E., Camprubí, A., Ramírez-Silva, G., López-Hernández, A., 2010, A statistics-based method for the short-wave infrared spectral analysis of altered rocks: An example from the Acozaco Caldera, Eastern Trans-Mexican Volcanic Belt, *Journal of Geochemical Exploration*, Vol 105, pp 1–10.
- Chen, M., Campbell, I.H., Xue, Y., Tian, W., Ireland, T.R., Holden P., Cas, R. A. F., Hayman, P. C., Das, R., 2015, Multiple sulphur isotope analyses support a magmatic model for the volcanogenic massive sulphide deposits of the Teutonic Bore

- Volcanic Complex, Yilgarn Craton, Western Australia, *Economic Geology*, Vol 110, pp 1411–1423.
- Donaldson, C.H., Henderson, C.M.B., 1988, A new interpretation of round embayment quartz crystals, *Mineralogical Magazine*, Vol 52, pp 27–33.
- Doyle, M.G., and Allen, R.L., 2003, Subsea-floor replacement in volcanic-hosted massive sulfide deposits, *Ore Geology Reviews*, Vol 23, pp 183-222.
- Duke, E.F., 1994, Near Infrared spectra of muscovite, Tschermak substitution and metamorphic reaction progress: Implications for remote sensing, *Geology*, Vol 22, pp 621–624.
- Franklin, J.M., Sangster, D.M., and Lydon, J.W., 1981, Volcanic-associated massive sulphide deposits, in Skinner, B.J., ed., *Economic Geology Seventy-Fifth Anniversary Volume*, Society of Economic Geologists, pp 485-627.
- Franklin, J.M., Gibson, H.L., Galley, A.G., and Jonasson, I.R., 2005, Volcanogenic Massive Sulphide Deposits, in Hedenquist, J.W., Thompson, J.F.H., Goldfarb, R.J., and Richards, J.P., eds., *Economic Geology 100th Anniversary Volume: Littleton, CO*, Society of Economic Geologists, pp 523-560.
- Frater, K.M., 2010, Bentley Stratigraphy, Internal Technical Report, Jabiru Metals.
- Galley, A.G., Hannington, M.D., Jonasson, I.R., 2007, Volcanogenic massive sulphide deposits, mineral deposits of Canada: Synthesis of major deposit types, district metallogeny, the evolution of geological provinces, and exploration methods, Geological Association of Canada, Mineral Deposits Division, Special Publication no. 5, pp 141–161.
- Gibson, H L., Allen, R.L., Riverin, G., Lane T.E., 2007, The VMS model: Advances and application to exploration targeting, ore deposits and exploration technology, Paper 49, In *Proceedings of Exploration 07: Fifth Decennial International Conference on Mineral Exploration*, edited by Milkereit, B., pp 713–730.
- Gifkins, C., Herrmann, W., Large, R. R., 2005, *Altered volcanic rocks: a guide to description and interpretation*, Centre for Ore Deposit Research, Hobart, Tasmania, University of Tasmania, pp 163–233.
- Geovia, Surpac Products, Dassault Systemes. Accessed March 23, 2017. <https://www.3ds.com/products-services/geovia/products/surpac/>
- Hallberg, J.A., Thompson, J.F.H., 1985, Geologic Setting of the Teutonic Bore Massive Sulphide Deposit, Archean Yilgarn Block, Western Australia, *Economic Geology*, Vol 80, pp 1953–1964.
- Hanchar, J.M., Miller, C.F., 1993, Zircon zonation patterns as revealed by cathodoluminescence and backscattered electron images: Implications for interpretation of complex crustal histories, *Chemical Geology*, Vol 110, pp 1–13
- Hikov, A., 2014, Paragonite and paragonitic altered rocks from the Asarel porphyry copper deposit, Central Srednogorie, *Compt. Rend. Acad. Bulg. Sci.*, Vol 67, pp 1119–1128.

- Hollis, S.P., Yeats, C.J., Wyche, S., Barnes, S.J., Ivanic, T.J., Belford, S.M., Davidson, G.J., Roache, A.J., Wingate, M.T.D., 2015, A review of volcanic-hosted massive sulphide (VHMS) mineralisation in the Archaean Yilgarn Craton, Western Australia: Tectonic, stratigraphic and geochemical associations: *Precambrian Research*, Vol 260, pp 113–135.
- Hollis, S.P., Yeats, C.J., Wyche, S., Barnes, S.J., Ivanic, T.J., 2017, VMS mineralisation in the Yilgarn Craton, Western Australia: A review of known deposits and prospectivity analysis of felsic volcanic rocks: *Geological Survey of Western Australia*, Report 165, 68p.
- Holten, T., Jamtveit, B., Meakin, P., 2000, Noise and oscillatory zoning of minerals, *Geochimica et Cosmochimica Acta*, 2000, Vol 64(11), pp 1893–1904.
- Huang, J., Chen, H., Han, J., Deng, X., Lu, W., Zhu, R., 2017, Alteration zonation and short wavelength infrared (SWIR) characteristics of the Honghai VMS Cu–Zn deposit, Eastern Tianshan, NW China, *Ore Geology Reviews* Vol 100 pp 263–279.
- Huston, D.L., Pehrsson, S., Eglington, B.M., Zaw, K., 2010, The geology and metallogeny of volcanogenic-hosted massive sulphide deposits: Variations through geologic time and with tectonic setting: *Economic Geology*, Vol 105, pp 571–591.
- Hutchison, R.W., 1972, Volcanogenic sulphide deposits and their metallogenic significance, *Economic Geology*, Vol 68, pp 1223–1246.
- Jones, S., Herrmann, W., Gemmell, J.B., 2005, Short wavelength infrared spectral characteristics of the HW horizon: Implications for exploration in the Myra Falls volcanic-hosted massive sulphide camp, Vancouver Island, British Columbia, Canada, *Economic Geology*, Vol 100, pp 273–294.
- Kaven, J.O., Martel, S.J., 2007, Growth of surface-breaching normal faults as a three-dimensional fracturing process, *Journal of Structural Geology*, Vol 29, pp 1463–1476.
- Kirkland, C.L., Wingate, M.T.D., 2012, Reading deep time: radiogenic isotope geochronology, *Geological Survey of Western Australia*, Record 2012/15, 10p.
- Korsch, R.J., Kositcin, N., Champion, D.C., 2011, Australian island arcs through time: Geodynamic implications for the Archean and Proterozoic, *Gondwana Research*, Vol 19, pp 716–734.
- Kositcin, N., Brown, S.J.A., Barley, M.E., Krapež, B., Cassidy, K.F., Champion, D.C., 2008, SHRIMP U–Pb zircon age constraints on the Late Archaean

- tectonostratigraphic architecture of the Eastern Goldfields Superterrane, Yilgarn Craton, Western Australia, *Precambrian Research*, Vol 161 pp 5–33.
- Krapež, B., Barley, M.E., 2008, Late Archaean synorogenic basins of the Eastern Goldfields Superterrane, Yilgarn Craton, Western Australia: Part III. Signatures of tectonic escape in an arc–continent collision zone, *Precambrian Research*, Vol 161(1), pp 183–199.
- Krapež, B., Pickard, A.L., 2010, Detrital–zircon age–spectra for Late Archaean synorogenic basins of the Eastern Goldfields Superterrane, Western Australia, *Precambrian Research* Vol 178, pp 91–118.
- Laakso, K., Peter, J.M., Rivard, B., White, H.P., 2016, Short–wave infrared spectral and geochemical characteristics of hydrothermal alteration at the Archean Izok Lake Zn–Cu–Pb–Ag volcanogenic massive sulphide deposit, Nunavut, Canada: Application in exploration target vectoring, *Economic Geology*, Vol 111, pp 1223–1239.
- Lalonde, E., Beaudoin, G., 2015, Petrochemistry, hydrothermal alteration, mineralogy, and sulphur isotope geochemistry of the Turgeon Cu–Zn volcanogenic massive sulphide deposit, northern New Brunswick, Canada, *Canadian Journal of Earth Science*, Vol 52, pp 215–234.
- Large, R.L., 1992, Australian volcanic–hosted massive sulphide deposits: Features, styles and genetic model: *Economic Geology*, Vol 87, pp 471–510.
- Large, R.L., Gemmell, B., Herrman, W., 1998, Summary of geochemical and mineralogical vectors to ore, based on the seven case studies in P439, *Studies of VHMS–related alteration: geochemical and mineralogical Vectors to Ore, P439*, Australian Minerals Research Association Limited, Final Report, 1998.
- Lau, I.C., Thapar, N., 2014, *Laboratory Spectroscopy calibration procedures*. CSIRO, Australia. EP147766.
- Leapfrog 3D, The Leapfrog Engine, ARNZ Geo Limited, Accessed September 3, 2017. <http://www.leapfrog3d.com/about-us/technology> .
- Martel, S.J., Langley J.S., 2006, Propagation of normal faults to the surface in basalt, Koaie fault system, Hawaii, *Journal of Structural Geology*, Vol 28, pp 2123–2143.
- Mindat.org, Phengite, Hudson Institute of Mineralogy. Accessed March 23, 2019. <https://www.mindat.org/min-3189.html>
- Nelson, D.L., 1997, Evolution of the Archaean granite–greenstone terranes of the Eastern Goldfields, Western Australia: SHRIMP U–Pb zircon constraints, *Precambrian Research* Vol 83, pp 57–81.
- Ohmoto, H., Rye, R.O., 1974, Hydrogen and oxygen isotopic compositions of fluid inclusions in the Kuroko Deposits, Japan, *Economic Geology*, Vol 69, pp 947–953.
- Peter, J.M., Scott, S.D., 1993, Fluid inclusion and light isotope geochemistry of the Windy Craggy Besshi–Type massive sulphide deposit, Northwestern British Columbia, *Resource Geology Special Issue*, Vol 17, pp 229–248.
- Pontual, S., 2005, *Spectral Interpretation Field Book: GMEX Vol. 1*, AUSSPEC International Ltd, Kew, Victoria.

- Pontual, S., 2011, Spectral Processing: getting it right and making it work for your project area: Spectral Geology Workshop, Perth, Western Australia, 2011, AUSSPEC International Ltd, Kew, Victoria.
- Rasmussen, B., Krapež, B., Muhling, J., Suvorova, A., 2015, Precipitation of iron silicate nanoparticles in early Precambrian oceans marks Earth's first iron age, *Geology*, Vol 43(4), pp 303–306
- Relvas, J.M.R.S., Barriga, F.J.A.S., 2006, Hydrothermal alteration and mineralisation in the Neves–Corvo volcanic–hosted massive sulphide deposit, Portugal. II. oxygen, hydrogen, and carbon isotopes, *Economic Geology*, Vol 101, pp 791–804.
- Ross, P-S., Bourke, A., Schnitzler, N., Conly, A., 2019, Exploration Vectors from Near Infrared Spectrometry near the McLeod Volcanogenic Massive Sulphide Deposit, Matagami District, Québec. *Economic Geology*, Vol 114. pp 613–638.
- Sangster, D.F., 1972, Precambrian Volcanogenic Massive Sulphide Deposits: A review, *Geological Survey of Canada, Paper 72–22*, p 44.
- Schardt, C., Cooke, D.R., Gemell, J.B., Large, R.R., 2001, Geochemical modelling of the zoned footwall alteration pipe Hellyer volcanic–hosted massive sulphide deposit, Western Tasmania, Australia, *Economic Geology*, Vol 96, pp 1037–1054.
- Shanks, W.C.P., III, and Thurston, R., (Eds), 2012, Volcanogenic massive sulphide occurrence model: U.S. Geological Survey Scientific Investigations Report, 2010–5070–C, p.345.
- Solomon, M., 1976, “Volcanic” massive sulphides and their host rocks, *Handbook of Strata–bound and Stratiform Ore Deposits*, Vol 6, Cu, Zn, Pb and Ag deposits, Elsevier Publishing, 1976.
- Stevenson, P., 2015, Bentley Deposit: Massive sulphide and stringer mineralisation resource estimate March–July 2015: Jaguar Base Metals Project, Independence Group NL.
- The Spectral Geologist, “TSG”, Commonwealth Scientific and Industrial Research Organisation (CSIRO). Accessed September 15, 2017. <https://research.csiro.au/thespectralgeologist/tsg/>
- Tornos, F., Peter, J. M., Allen, R., Conde, C., 2015, Controls on the siting and style of volcanogenic massive sulphide deposits, *Ore Geology Reviews*, Vol 68. pp 142–163.
- Whitney, D.L., and Evans, B. W., 2010, Abbreviations for names of rock–forming minerals, *American Mineralogist*, Vol 95, pp 185–187.

Yang, W., Niu, H., Shan, Q., Sun, W., Zhang, H., Li, N-B., Jiang, Y., Yu, X-Y., 2014, Geochemistry of magmatic and hydrothermal zircon from the highly evolved Baerzhe alkaline granite: Implications for Zr-REE-Nb mineralization, *Mineralium Deposita*, Vol 49(4), pp 451–470.

Appendix 1. Petrographic Descriptions

Six samples were examined using transmitted light microscopy. All conventional microscopy study was undertaken using the facilities at the Department of Applied Geology, Curtin University, Australia.

The following individual section descriptions include the sample ID, rock description, and description of the mineralogy.

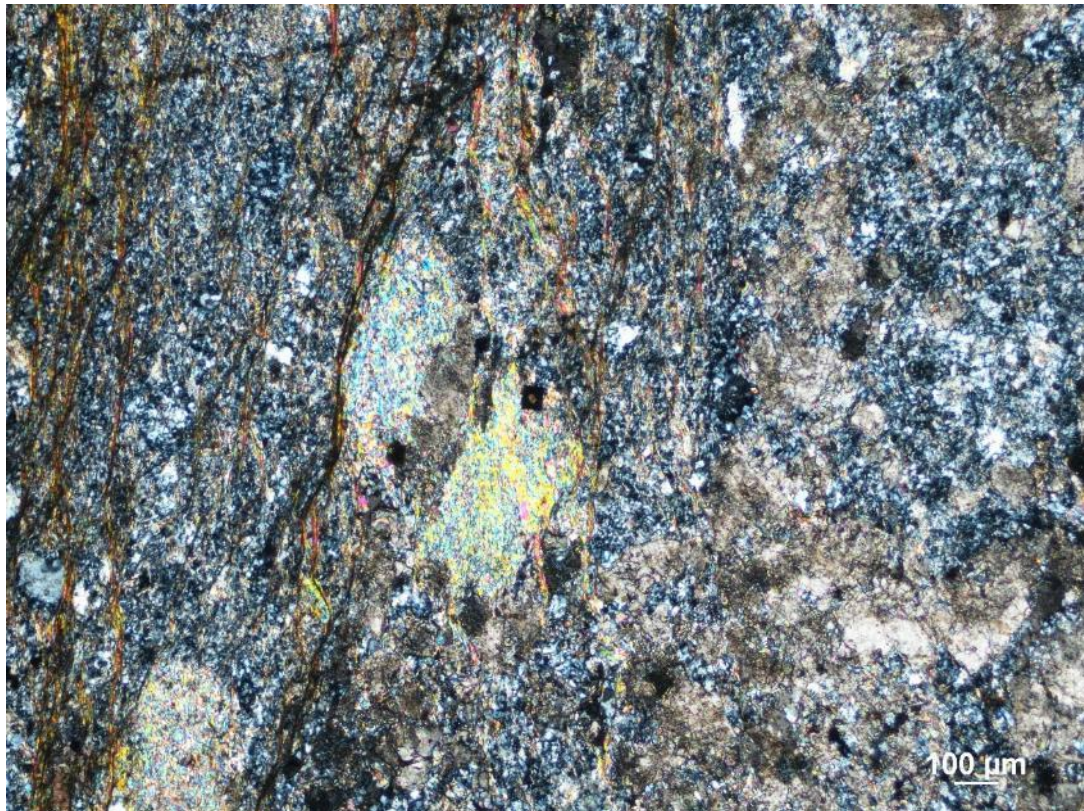
Sample N° A4

Rock Description:

Sericite–altered quartz rhyolite.

Mineralogy:

<u>Mineral</u>	<u>Mode %</u>	<u>Textural features of mineral</u>
Quartz	40	Very fine–grained matrix with a few larger phenocrysts.
Sericite 1	22	Brown sericite that defines a metamorphic foliation.
Sericite 2	8	High birefringence sericite that pseudomorphs relict feldspar.
Carbonate	30	Massive irregular zones.



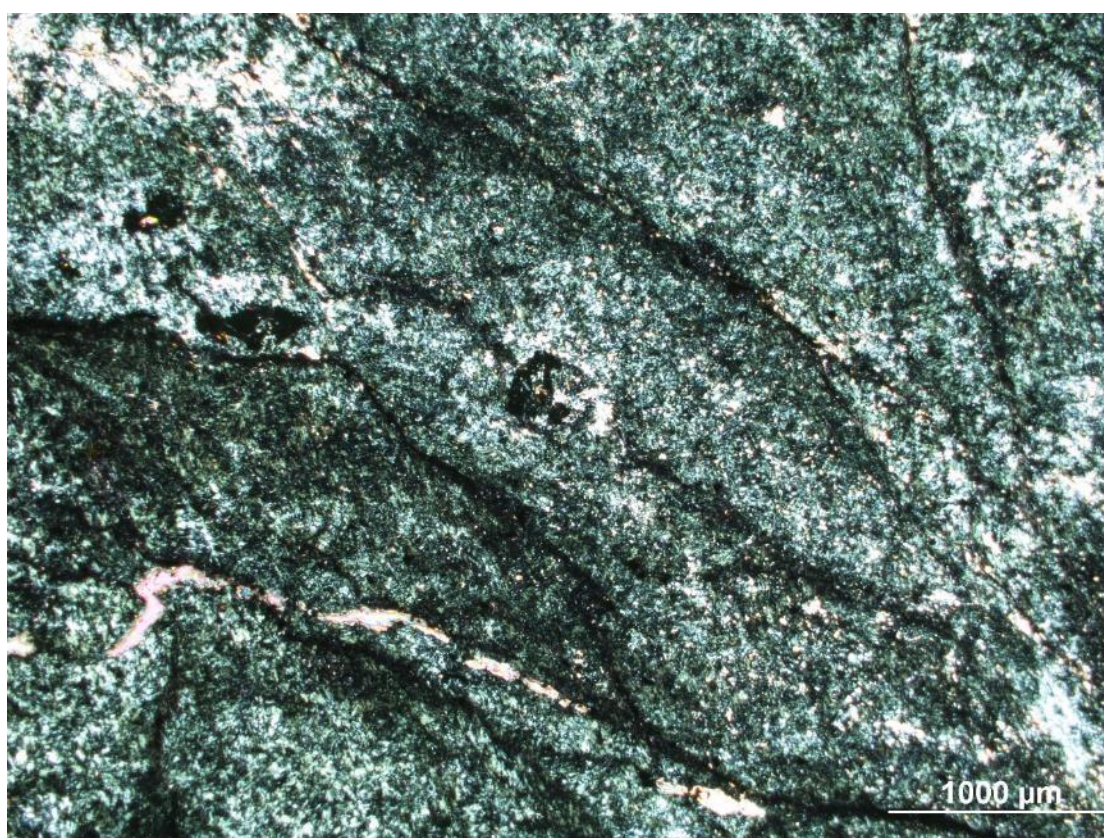
Sample N° A5

Rock Description:

Chlorite–altered quartz rhyolite, possible void infill.

Mineralogy:

<u>Mineral</u>	<u>Mode %</u>	<u>Textural features of mineral</u>
Quartz	15	Minor fine–grained quartz with a few large rounded relict quartz clasts.
Chlorite	80	Green–black chlorite that defines a metamorphic foliation.
Carbonates	5	Minor carbonate veins.



Sample N° A6

Rock Description:

Chlorite–altered quartz rhyolite.

Mineralogy:

<u>Mineral</u>	<u>Mode %</u>	<u>Textural features of mineral</u>
Quartz	10	Very fine–grained quartz
Chlorite	80	Brown sericite that defines a metamorphic foliation.
Sulphides	10	Opaque subhedral sulphides (<10 microns).



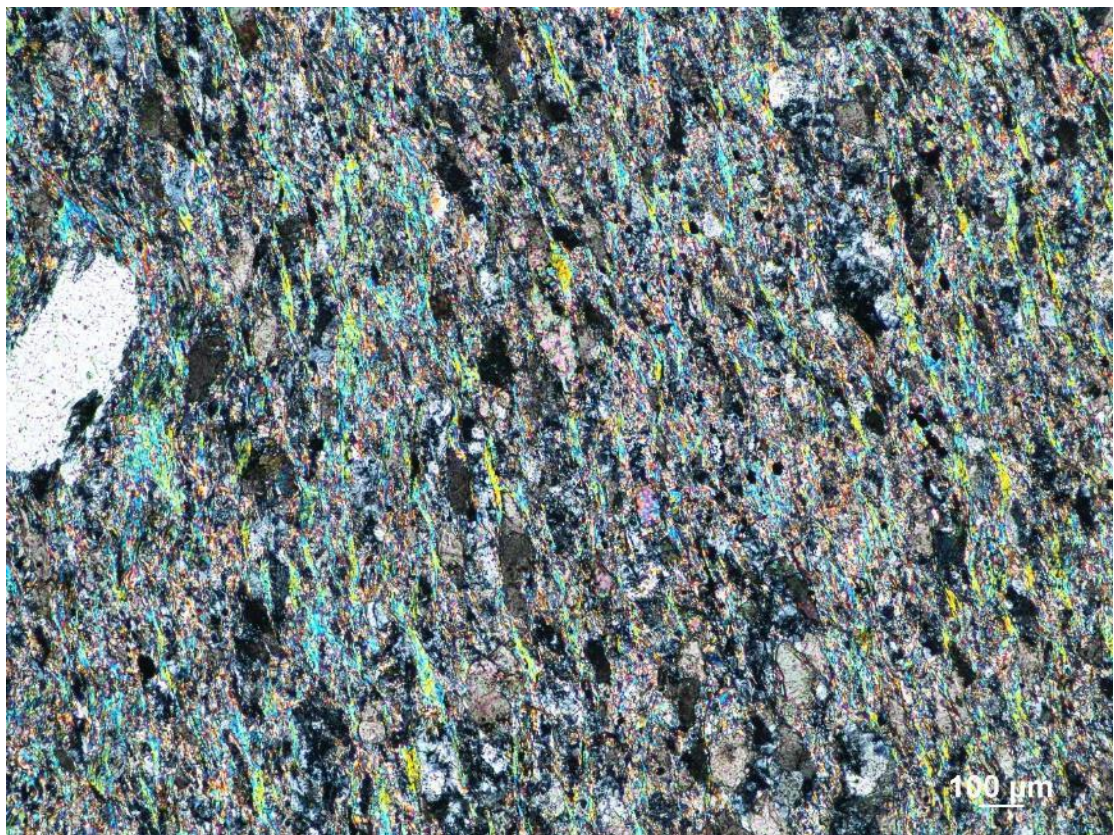
Sample N° A7

Rock Description:

Sericite–altered quartz rhyolite.

Mineralogy:

<u>Mineral</u>	<u>Mode %</u>	<u>Textural features of mineral</u>
Quartz	50	Very fine–grained matrix with a few larger clasts.
Sericite	30	High birefringence sericite that defines a metamorphic foliation.
Carbonates	20	Massive irregular zones.



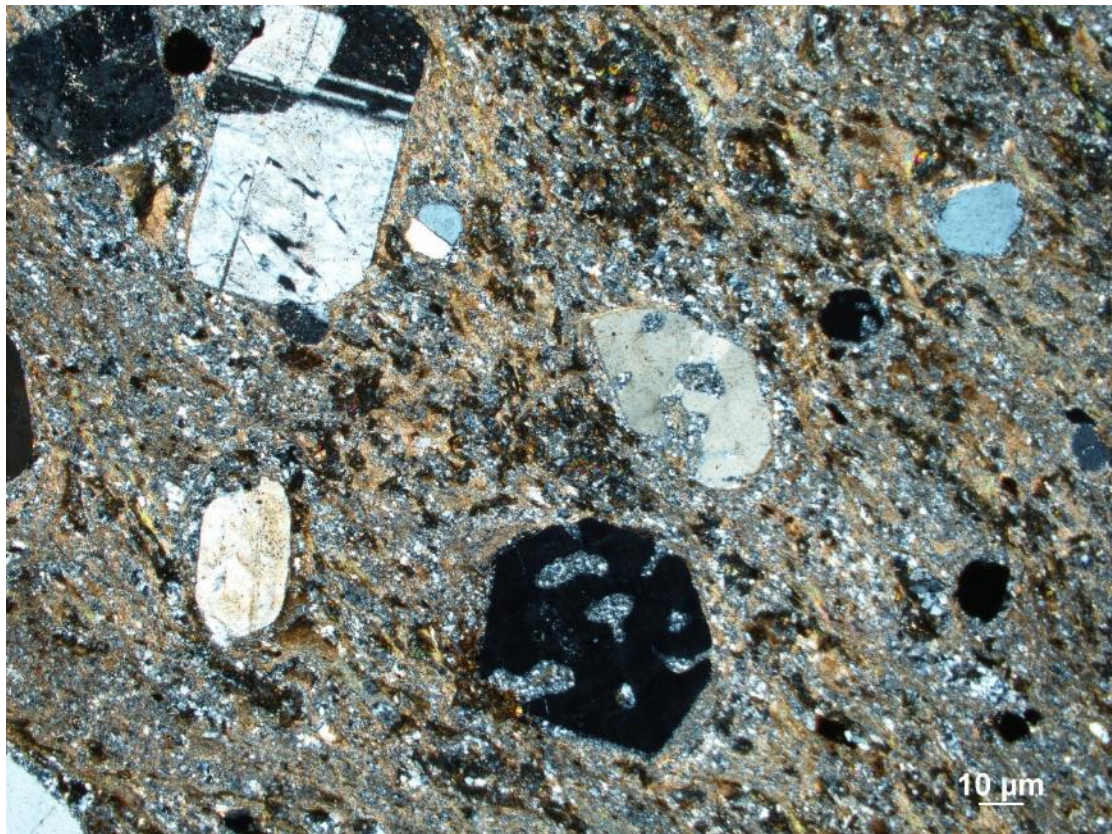
Sample N° A8

Rock Description:

Quartz rhyolite with minor alteration.

Mineralogy:

<u>Mineral</u>	<u>Mode %</u>	<u>Textural features of mineral</u>
Quartz	60	Very fine-grained matrix with a many larger clasts with embayments.
Sericite	25	Brown sericite that defines a metamorphic foliation.
Feldspar	15	Euhedral K-feldspar (sanidine).



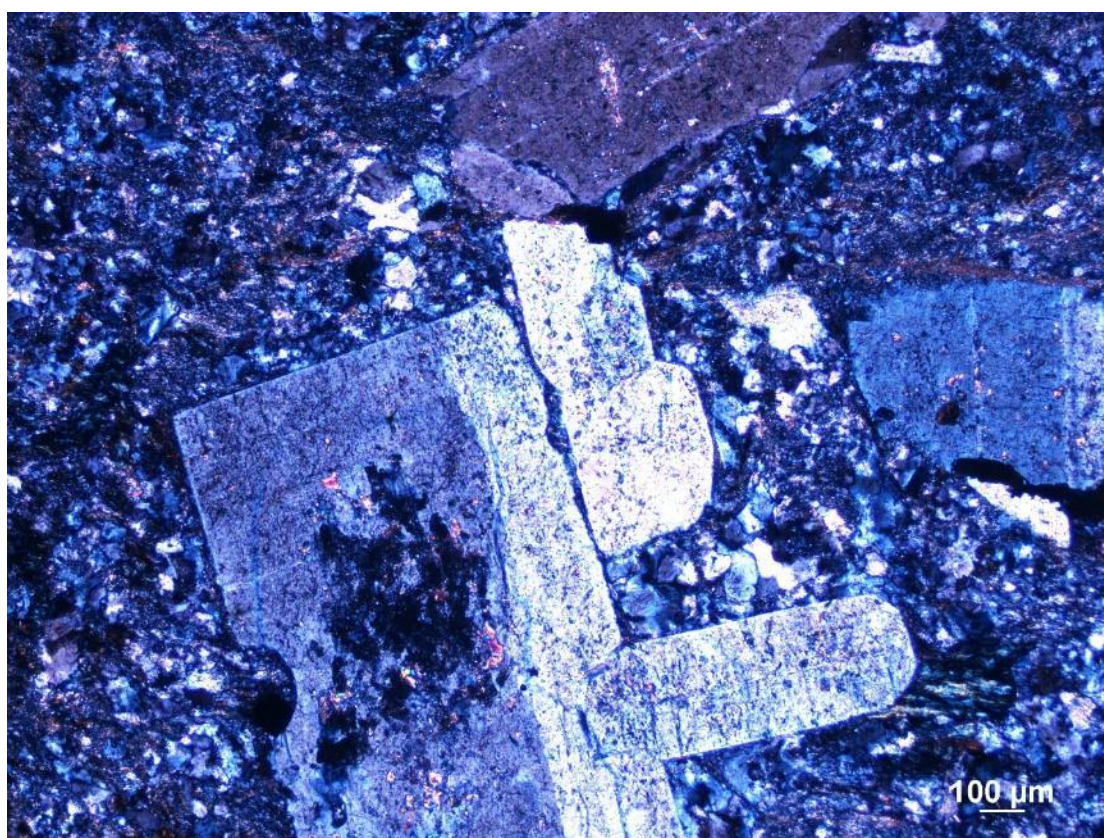
Sample N° A9

Rock Description:

Sericite–altered quartz rhyolite.

Mineralogy:

<u>Mineral</u>	<u>Mode %</u>	<u>Textural features of mineral</u>
Quartz	60	Very fine–grained matrix with a few larger clasts.
Sericite	22	Brown sericite that defines a metamorphic foliation.
Feldspar	10	Twinned euhedral K–feldspar (sanidine).
Chlorite	8	Dark green chlorite.



Appendix 2. SEM–EDS Observations

Two samples were investigated with SEM–EDS. A Hitachi TM3030 table–top scanning electron microscope (SEM) equipped with a SWIFT ED3000 energy dispersive spectrometer (EDS) was used at the Western Australian School of Mines, Curtin University. The accelerating voltage was 15 kV and the filament current were 1850 mA. The EDS detector was calibrated with copper foil; analyses are semi–quantitative

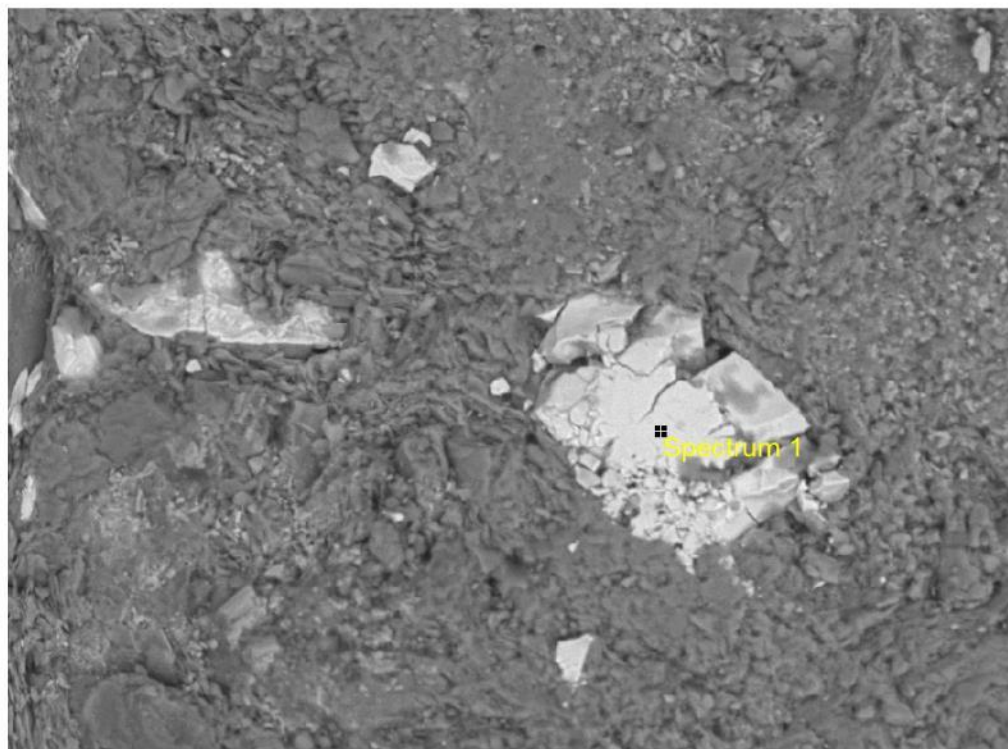
The following descriptions include an electron image, acquisition conditions, quantification settings, and a summary of results.

Spectrum details

Sample ID: A9

Electron Image

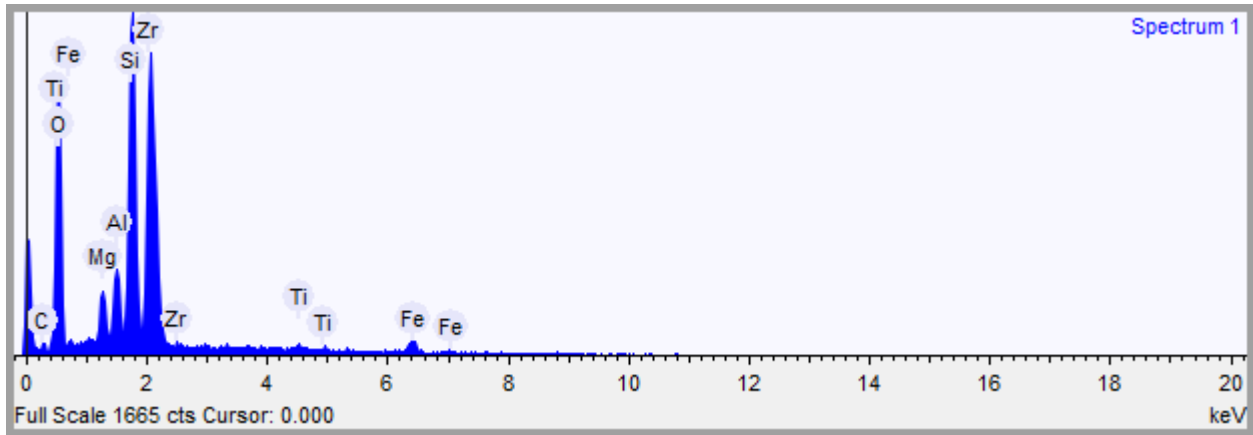
Image Width: 163.9 μm



90 μm

Acquisition conditions

Acquisition time (s)	10.0	Process time	5
Accelerating voltage (kV)	15.0		



Quantification Settings

Quantification method	Stoichiometry (normalised)
Combined element	Oxygen
Number of anions	6.0
Coating element	None

Summary results

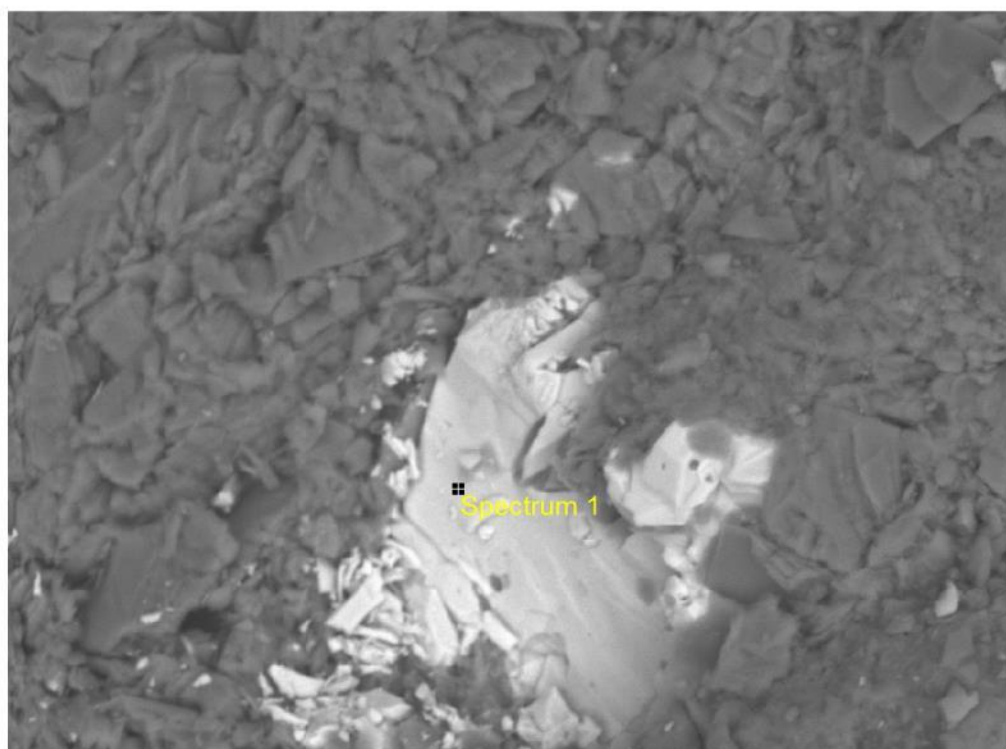
Element	Weight %	Weight % σ	Atomic %	Compound %	Formula
Carbon	4.480	0.797	9.208	16.414	CO ₂
Magnesium	2.068	0.115	2.100	3.429	MgO
Aluminium	2.418	0.117	2.213	4.570	Al ₂ O ₃
Silicon	12.235	0.280	10.755	26.174	SiO ₂
Titanium	0.621	0.125	0.320	1.036	TiO ₂
Iron	3.021	0.243	1.336	3.886	FeO
Zirconium	32.937	0.720	8.915	44.490	ZrO ₂
Oxygen	42.220	0.961	65.153		

Spectrum details

Sample ID: A5

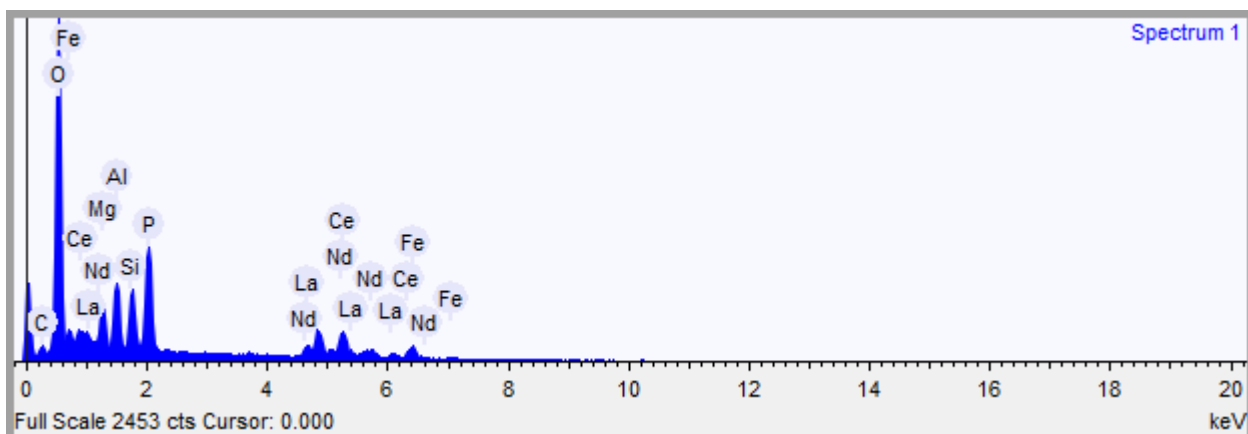
Electron Image

Image Width: 81.9 μm



Acquisition conditions

Acquisition time (s)	10.0	Process time	5
Accelerating voltage (kV)	15.0		



Quantification Settings

Quantification method	Stoichiometry (normalised)
Combined element	Oxygen
Number of anions	6.0
Coating element	None

Summary results

Element	Weight %	Weight % σ	Atomic %	Compound %	Formula
Carbon	4.410	0.725	9.134	16.159	CO ₂
Magnesium	3.502	0.182	3.583	5.806	MgO
Aluminium	5.068	0.187	4.673	9.576	Al ₂ O ₃
Silicon	4.503	0.178	3.989	9.634	SiO ₂
Phosphorus	9.269	0.270	7.444	21.238	P ₂ O ₅
Iron	3.848	0.308	1.714	4.951	FeO
Lanthanum	5.713	0.516	1.023	6.700	La ₂ O ₃
Cerium	14.115	0.631	2.506	16.533	Ce ₂ O ₃
Neodymium	8.062	0.577	1.391	9.404	Nd ₂ O ₃
Oxygen	41.509	0.984	64.543		

Appendix 3. Laser Ablation Inductively Coupled Plasma Mass Spectrometry (LA-ICPMS)

Two samples were examined with sensitive high-resolution ion microprobe (LA-ICPMS). This was undertaken the Department of Applied Geology, John de Laeter Centre, Curtin University, Australia.

	Monazite															
Notes CLK	ID	Final238_206	Final238_206_Prop2SE	Age 6/8	Age er	Final207_206	Final207_206_Prop2SE	Age 7/6	Age er	discordance	Final206_204	Final206_204_Int2SE	Approx_U_PPM	Approx_Th_PPM	Approx_Pb_PPM	Final_U_Th_Ratio
discordant	A5-9	2.141328	0.1879966	2470	168	0.23	0.036	3052	231	19	0.0	0.0	16	996	163.1	0.0141
	Zircon															
Notes CLK	ID	Final238_206	Final238_206_Prop2SE	Age 6/8	Age er	Final207_206	Final207_206_Prop2SE	Age 7/6	Age er	discordance	Final206_204	Final206_204_Int2SE	Approx_U_PPM	Approx_Th_PPM	Approx_Pb_PPM	Final_U_Th_Ratio
i	A9-9	1.926782	0.0742498	2695	82	0.1808	0.009	2660	80	-1	110000.0	180000.0	68.7	71.2	87.9	0.92
i	A9-13	2.024291	0.07785737	2588	79	0.1837	0.0099	2687	86	4	310000.0	390000.0	49.5	20.5	30	2.5
i	A9-20	1.968504	0.08137516	2648	87	0.1839	0.0095	2688	83	1	-160000.0	260000.0	79.8	53.2	80.9	1.5
i	A9-4	2.087683	0.07845154	2523	76	0.1849	0.0094	2697	82	6	580000.0	690000.0	88.5	70.9	89.2	1.257
i	A9-8	1.851852	0.05144033	2783	61	0.1882	0.0087	2726	74	-2	-900000.0	1000000.0	149.3	133	206	1.192
i	A9-2	1.801802	0.07466926	2846	92	0.1901	0.01	2743	84	-4	28000.0	47000.0	54.6	26.2	34.8	2.06
i	A9-21	2.04918	0.0839828	2562	84	0.1903	0.01	2745	84	7	-290000.0	630000.0	87.7	51.4	79	1.75
i	A9-19	1.788909	0.1056064	2862	130	0.1904	0.01	2746	84	-4	230000.0	350000.0	51.2	32	47	1.539
i	A9-5	1.964637	0.1119341	2652	118	0.1911	0.011	2752	92	4	-700000.0	130000.0	51	75	75	0.76
i	A9-12	1.937984	0.1014062	2682	110	0.1913	0.01	2753	83	3	-310000.0	480000.0	65.1	30.9	41.1	2.13
discordant	A9-22	2.298851	0.073986	2328	61	0.1918	0.01	2758	83	16	-520000.0	510000.0	106	127	152	0.818
i	A9-6	2.008032	0.07661167	2605	79	0.1921	0.0098	2760	81	6	130000.0	120000.0	100	100	117.6	1.02
inherited?	A9-17	1.694915	0.1694915	2989	221	0.194	0.02	2776	160	-8	110000.0	370000.0	27.9	20	31.3	1.46
inherited?	A9-23	1.831502	0.1543024	2809	179	0.209	0.02	2898	147	3	590000.0	870000.0	27.3	71	49.1	0.463
discordant	A9-10	1.923077	0.06656805	2699	74	0.262	0.015	3259	87	17	113000.0	15000.0	161	110.4	385	1.429
discordant	A9-15	1.848429	0.1674178	2788	191	0.265	0.018	3277	103	15	170000.0	190000.0	31	24.2	57.3	1.3
inherited?	A9-16	1.388889	0.2121914	3496	368	0.267	0.031	3288	171	-6	300000.0	330000.0	10.9	8.5	25.6	1.37
discordant	A9-14	1.636661	0.117861	3074	166	0.333	0.028	3631	123	15	159000.0	40000.0	135.2	41.3	500	3.27
discordant	A9-3	1.862197	0.1213723	2771	139	0.359	0.029	3746	118	26	16900.0	7600.0	17.8	9.14	58.8	1.96
discordant	A9-18	0.5617978	0.2714304	6591	1508	0.614	0.074	4541	164	-45	-37000.0	5100.0	80.9	44.9	2.30E+03	1.81

Appendix 4. Rock Descriptions and Location of Samples for Figure 5.5

The sample identifier, location, rock types, associations and MGA 51 co-ordinates of the thirty-five samples described by Kositcin et al (2008) are provided in Table A4.1.

The sample ID and ages of these samples are shown in Figure 5.5.

Table 2
Rock descriptions and locations of sample sites

Sample	Rock type	Location	Unit/association	MGA_mE	MGA_mN	Mount no. (UWA)
Kalgoorlie Terrane						
E265	Rhyolite porphyry clast	Black Swan (BSD117, 146m)	Karnabald Sequence	370801	6636858	99-53A
E356	Volcanogenic conglomerate	Black Swan (95BSD18, 267.7-271.7 m)	Karnabald Sequence	370801	6636858	A80C
E357	Volcanogenic conglomerate	Black Swan (95BSD18, 581.9-585 m)	Karnabald Sequence	370801	6636858	A80D
E203	Metamorphosed sandstone	Widgenoomoola, Lake Lefroy	Kalgoorlie Sequence	362977	6519360	98-100A
E321	Volcaniclastic sandstone	Emigna (EN99-15, 162.5 m)	Kalgoorlie Sequence	363137	6566157	99-72A
E322	Volcaniclastic sandstone	Emigna (EN99-15, 153.6 m)	Kalgoorlie Sequence	363137	6566157	99-68B
E320	Quartz-rich volcaniclastic sandstone	Kanowna	Gravadam Grit – Kalgoorlie Sequence	367137	6615457	99-72C
E396	Volcaniclastic sandstone	Lawlers (LARCD1028, 344 m)	Vivien Sequence, Agnew Domain	270732	6893159	C16B
E385	Polymict volcanic breccia	Jundee (JBCD 5985, 631.6-632.4 m)	Middle Greenstone Sequence, Yandal Belt	260240	7080975	B80
E387	Volcanogenic sandstone	Jundee (JBCD 5985, 277.7-278.1 m)	Middle Greenstone Sequence, Yandal Belt	260240	7080975	B91A
Gindalbie Terrane						
E225	Porphyritic rhyolite	Spring Well, Yandal Belt	Calc-alkalic andesite/rhyolite	318245	6912790	99-58B
E227	Porphyritic andesite dike	Spring Well, Yandal Belt	Calc-alkalic andesite/rhyolite	319756	6913854	99-58D
E349	Tuff intraclast in rhyolite breccia	Wild Dog Dam, Gindalbie	Felsic volcanic rocks	386781	6655445	A60B
E350	Bedded volcanogenic sandstone	Maggies Dam, Gindalbie	Felsic volcanic rocks	391713	6642173	A66A
E353	Coarse-grained feldspathic sandstone	Bulong	Felsic volcanic rocks	387814	6594545	A80A
E359	Feldspathic sandstone	Mt Monger	Gindalbie Terrane (Bulong)	402950	6570331	B12A
E360	Rhyolite clast	Mt Monger	Gindalbie Terrane (Bulong)	402956	6570304	B13C
E229	Quartzofeldspathic sandstone	Yandal Station	Yandal Sequence	322405	6941809	99-11B
Kurnalpi Terrane						
E214	Andesite-derived sandstone	Welcome Well, Minerie	Association 2 andesite	375689	6808958	99-11C
E047	Rhyolitic volcaniclastic	Bore Well	Association 2 andesite	429221	6759741	96-9A
E258	Dacitic porphyry	Ida Hill	Association 2 dacite	449988	6820243	99-53B
E367	Rhyolite	Liberty Bore	Ejuidina Domain	475071	6635878	B12C
E324	Andesite-derived sandstone	Sunrise Dam (Cleo pit)	Ejuidina Domain	442737	6782858	A47C
E380	Felsic volcaniclastic	Murphy Hills (MURCD163, 133.5 m)	Ejuidina Domain	426394	6911968	B22A
E382	Quartz-feldspar porphyry intrusive	Murphy Hills (MURCD236, 124.1 m)	Ejuidina Domain	426213	6911937	B22B
E337	Sandstone horizon in conglomerate	Yilgange, Ejuidina	Middle Yilgange Sequence	419279	6707098	A60C
E314	Quartzofeldspathic sandstone	Twin Peaks, Yilgange (JDDH1, 106m)	Base Yilgange Sequence	432017	6674994	99-58A
E319	Sandstone horizon in conglomerate	Wallaby (WBAD29, 358m)	Wallaby Conglomerate	432238	6808358	99-68A
E313	Sandstone horizon in conglomerate	Lancefield	Lancefield Conglomerate	436521	6838386	99-68C
E401	Polymict breccia	Granny Smith (GSDD175, 457.7-458.7 m)	Granny Smith Mine Sequence	443681	6814134	C33A
E407	Med- to fine-grained sandstone and shale	Royal (RYRBB002, 225.8-226.5 m)	Royal Sandstone	452608	6829558	C33C
E408	Med- to fine-grained sandstone and shale	Royal (RYRBB002, 386.4-386.9 m)	Royal Sandstone	452608	6829558	C48C
Laverton Terrane						
E392	Fine-grained sandstone	Windarra (PSD19, 533-534.85 m)	Association 1 turbidites (BIF)	429364	6833977	B91B
Duketon Terrane						
E374	Intermediate/felsic volcaniclastic	Famous Blue (FABCD10, 283 m)	Duketon Belt sequence	408648	6950804	B12B
E375	Intermediate porphyritic intrusion	Famous Blue (FABCD10, 205 m)	Duketon Belt sequence	408648	6950804	B13A

Appendix 5. Short Wave Infrared Data Sample

A total of 5600 samples were collected from wall chip samples and diamond drill core. The SWIR data was collected at the Jaguar/Bentley mine site using an ASD Terra Spec 2 spectral scanner. The spectral samples were processed using TSG (The Spectral Geologist) software. Only selected results are provided here.

Drillhole Trace	From	To	w2200	hq2200	w2250	hq2250	hq2250/hq2200
08SWDD03	620	620.1	2196.13	0.284	NULL	NULL	Null
08SWDD03	625	625.1	2197.16	0.234	NULL	NULL	Null
08SWDD03	630	630.1	2196.58	0.285	NULL	NULL	Null
08SWDD03	635	635.1	2196.35	0.375	NULL	NULL	Null
08SWDD03	640	640.1	2196.66	0.284	NULL	NULL	Null
08SWDD03	645	645.1	2196.65	0.185	NULL	NULL	Null
08SWDD03	650	650.1	2197.42	0.296	NULL	NULL	Null
08SWDD03	655	655.1	2197.25	0.279	NULL	NULL	Null
08SWDD03	659.9	660	2195.91	0.294	NULL	NULL	Null
08swdd05	568	568.1	2195.82	0.222	2252.31	0.0755	0.34
08swdd05	585	585.1	2195.45	0.271	2252.7	0.0409	0.15
08swdd05	660	660.1	2196.89	0.355	2253.48	0.216	0.61
08swdd05	640	640.1	2195.48	0.313	2254.04	0.221	0.71
08swdd05	647	647.1	2196.25	0.247	2254.22	0.215	0.87
08swdd05	670	670.1	2196.33	0.341	2254.24	0.204	0.6
08swdd05	665	665.1	2196.2	0.294	2254.33	0.233	0.79
08swdd05	675	675.1	2195.65	0.307	2254.36	0.172	0.56
08swdd05	620	620.1	2195.51	0.362	2254.42	0.207	0.57
08swdd05	645	645.1	2195.68	0.312	2254.43	0.259	0.83
08swdd05	650	650.1	2195.5	0.351	2254.43	0.197	0.56
08swdd05	570	570.1	2195.97	0.137	2254.52	0.0455	0.33
08swdd05	655	655.1	2196.52	0.306	2254.65	0.264	0.86
08swdd05	560	560.1	2196.31	0.241	2254.66	0.087	0.36
08swdd05	679.9	680	2196	0.32	2254.72	0.233	0.73
08swdd05	520	520.1	2194.79	0.311	2254.73	0.0784	0.25
08swdd05	565	565.1	2196.04	0.266	2254.77	0.0906	0.34
08swdd05	610	610.1	2195.93	0.286	2255	0.192	0.67
08swdd05	595	595.1	2195.66	0.335	2255.09	0.158	0.47
08swdd05	630	630.1	2195.37	0.428	2255.19	0.237	0.55
08swdd05	575	575.1	2195.61	0.226	2255.53	0.0559	0.25
08swdd05	605	605.1	2195.77	0.375	2255.7	0.197	0.53
08swdd05	600	600.1	2195.52	0.301	2255.75	0.192	0.64
08swdd05	635	635.1	2195.34	0.233	2255.78	0.201	0.86
08swdd05	625	625.1	2195.69	0.305	2255.88	0.199	0.65
08swdd05	615	615.1	2195.81	0.349	2256.14	0.271	0.78
08swdd05	580	580.1	2196.25	0.265	2256.76	0.0976	0.37
08swdd05	590	590.1	2195.66	0.288	2257.57	0.124	0.43
08swdd05	509	509.1	2195.01	0.201	NULL	NULL	Null
08swdd05	510	510.1	2194.87	0.256	NULL	NULL	Null
08swdd05	512	512.1	2194.65	0.139	NULL	NULL	Null
08swdd05	514	514.1	2194.99	0.149	NULL	NULL	Null
08swdd05	516	516.1	2195.01	0.215	NULL	NULL	Null
08swdd05	518	518.1	2195.2	0.285	NULL	NULL	Null
08swdd05	525	525.1	2196.32	0.283	NULL	NULL	Null
08swdd05	530	530.1	2195.99	0.339	NULL	NULL	Null

08swdd05	535	535.1	2195.63	0.4	NULL	NULL	Null
08swdd05	540	540.1	2196.63	0.157	NULL	NULL	Null
08swdd05	545	545.1	2195.55	0.143	NULL	NULL	Null
08swdd05	550	550.1	2195.55	0.38	NULL	NULL	Null
08swdd05	555	555.1	2195.6	0.365	NULL	NULL	Null
09BTDD001	632	632.1	2192.87	0.0765	2249.81	0.0274	0.36
09BTDD001	644.9	645	2195.8	0.191	2254.48	0.0479	0.25
09BTDD001	650	650.1	2200.88	0.116	2256.34	0.0843	0.73
09BTDD001	640	640.1	2194.8	0.14	2256.83	0.0563	0.4
09BTDD001	634	634.1	2196.28	0.116	2258.04	0.0689	0.59
09BTDD001	638	638.1	2194.77	0.0963	NULL	0.0462	0.48
09BTDD001-W1	592	592.1	2192.23	0.169	2242.49	0.0159	0.09
09BTDD001-W1	586	586.1	2193.44	0.132	2245.63	0.0845	0.64
09BTDD001-W1	596	596.1	2195.15	0.123	2247.37	0.051	0.41
09BTDD001-W1	630	630.1	2194.87	0.395	2252.54	0.115	0.29
09BTDD001-W1	608	608.1	2195.04	0.449	2252.8	0.119	0.27
09BTDD001-W1	620	620.1	2194.94	0.32	2254.02	0.0878	0.27
09BTDD001-W1	642.9	643	2195.76	0.403	2254.34	0.175	0.43
09BTDD001-W1	598	598.1	2195.37	0.12	2254.53	0.057	0.48
09BTDD001-W1	635	635.1	2195.56	0.344	2254.66	0.188	0.55
09BTDD001-W1	640	640.1	2195.41	0.37	2254.74	0.193	0.52
09BTDD001-W1	606	606.1	2195.64	0.307	2254.77	0.145	0.47
09BTDD001-W1	602	602.1	2195.29	0.322	2255.02	0.12	0.37
09BTDD001-W1	604	604.1	2195.11	0.279	2255.74	0.179	0.64
09BTDD001-W1	615	615.1	2195.36	0.209	2255.85	0.0958	0.46
09BTDD001-W1	590	590.1	2191.1	0.154	2256.4	0.0635	0.41
09BTDD001-W1	584	584.1	2196.97	0.166	2256.67	0.0976	0.59
09BTDD001-W1	580	580.1	2198.68	0.195	2258.21	0.211	1.08
09BTDD001-W1	582	582.1	2197.23	0.0917	2258.55	0.044	0.48
09BTDD001-W1	594	594.1	2193.85	0.118	2259.71	0.041	0.35
09BTDD001-W1	588	588.1	2192.52	0.163	NULL	NULL	Null
09BTDD001-W1	600	600.1	2193.47	0.556	NULL	NULL	Null
09BTDD001-W1	610	610.1	2195.38	0.343	NULL	NULL	Null
09BTDD001-W1	625	625.1	2194.77	0.394	NULL	NULL	Null
09BTDD003	594	594.1	2195.7	0.222	2251.06	0.0373	0.17
09BTDD003	600	600.1	2196.39	0.183	2251.66	0.0431	0.24
09BTDD003	598	598.1	2195.26	0.308	2252.7	0.0525	0.17
09BTDD003	558	558.1	2194.81	0.141	2253.26	0.0249	0.18

09BTDD003	608	608.1	2195.76	0.326	2254.01	0.0536	0.16
09BTDD003	602	602.1	2195.96	0.306	2254.08	0.0963	0.31
09BTDD003	610	610.1	2195.45	0.345	2254.38	0.0766	0.22
09BTDD003	588	588.1	2195.81	0.174	2254.42	0.0425	0.24
09BTDD003	620	620.1	2195.56	0.316	2254.45	0.0924	0.29
09BTDD003	629.9	630	2195.42	0.233	2254.92	0.107	0.46
09BTDD003	556	556.1	2194.82	0.181	NULL	NULL	Null
09BTDD003	560	560.1	2194.94	0.172	NULL	NULL	Null
09BTDD003	562	562.1	2194.1	0.348	NULL	NULL	Null
09BTDD003	564	564.1	2193.78	0.443	NULL	NULL	Null
09BTDD003	566	566.1	2194.16	0.422	NULL	NULL	Null
09BTDD003	568	568.1	2194.07	0.284	NULL	NULL	Null
09BTDD003	570	570.1	2193.69	0.418	NULL	NULL	Null
09BTDD003	575	575.1	2193.34	0.376	NULL	NULL	Null
09BTDD003	580	580.1	2193.83	0.294	NULL	NULL	Null
09BTDD003	585	585.1	2196.24	0.303	NULL	NULL	Null
09BTDD003	590	590.1	2195.39	0.222	NULL	NULL	Null
09BTDD003	592	592.1	2195.36	0.275	NULL	NULL	Null
09BTDD003	596	596.1	2195.86	0.256	NULL	NULL	Null
09BTDD003	604	604.1	2195.49	0.34	NULL	NULL	Null
09BTDD003	606	606.1	2195.84	0.219	NULL	NULL	Null
09BTDD003	615	615.1	2195.87	0.411	NULL	NULL	Null
09BTDD003	625	625.1	2195.59	0.386	NULL	NULL	Null
09BTDD006	414	414.1	2196.24	0.265	2251.92	0.0571	0.22
09BTDD006	416	416.1	2196.16	0.31	2252.18	0.0746	0.24
09BTDD006	430	430.1	2195.41	0.428	2252.26	0.102	0.24
09BTDD006	445	445.1	2196	0.317	2252.39	0.0632	0.2
09BTDD006	440	440.1	2195.68	0.341	2252.69	0.0547	0.16
09BTDD006	435	435.1	2195.86	0.392	2253.26	0.0957	0.24
09BTDD006	449.9	450	2196.2	0.402	2254.99	0.236	0.59
09BTDD006	420	420.1	2196.15	0.255	2255	0.113	0.44
09BTDD006	404	404.1	2196.7	0.106	NULL	NULL	Null
09BTDD006	406	406.1	2195.78	0.27	NULL	NULL	Null
09BTDD006	408	408.1	2195.57	0.344	NULL	NULL	Null
09BTDD006	410	410.1	2195.85	0.25	NULL	NULL	Null
09BTDD006	412	412.1	2196.21	0.319	NULL	NULL	Null
09BTDD006	418	418.1	2196.17	0.437	NULL	NULL	Null
09BTDD006	425	425.1	2196.1	0.363	NULL	NULL	Null
09BTDD007	366	366.1	2196.34	0.235	2242.26	0.0652	0.28
09BTDD007	382	382.1	2196.12	0.298	2251.94	0.0682	0.23
09BTDD007	356	356.1	2195.84	0.393	2253.25	0.0848	0.22
09BTDD007	374	374.1	2195.67	0.364	2253.25	0.123	0.34
09BTDD007	416	416.1	2196.56	0.377	2253.49	0.101	0.27
09BTDD007	364	364.1	2195.5	0.301	2253.71	0.125	0.42
09BTDD007	370	370.1	2196.41	0.27	2254	0.141	0.52
09BTDD007	400	400.1	2196.88	0.346	2254.02	0.149	0.43
09BTDD007	417.5	417.6	2196.66	0.297	2254.35	0.136	0.46

09BTDD007	390	390.1	2196.54	0.403	2254.47	0.212	0.53
09BTDD007	408	408.1	2197.15	0.272	2254.53	0.181	0.67
09BTDD007	362	362.1	2195.36	0.278	2254.66	0.14	0.5
09BTDD007	380	380.1	2196.07	0.21	2254.69	0.0798	0.38
09BTDD007	414	414.1	2197.18	0.22	2254.69	0.138	0.63
09BTDD007	376	376.1	2196.57	0.378	2254.78	0.122	0.32
09BTDD007	388	388.1	2196.16	0.39	2254.9	0.17	0.44
09BTDD007	412	412.1	2196.68	0.184	2254.91	0.123	0.67
09BTDD007	405	405.1	2197.02	0.328	2254.93	0.238	0.73
09BTDD007	384	384.1	2196.4	0.21	2255.05	0.113	0.54
09BTDD007	386	386.1	2195.9	0.227	2255.1	0.192	0.85
09BTDD007	372	372.1	2195.93	0.329	2255.2	0.148	0.45
09BTDD007	410	410.1	2197.46	0.209	2255.21	0.213	1.02
09BTDD007	395	395.1	2196.94	0.187	2255.45	0.18	0.96
09BTDD007	360	360.1	2195.28	0.384	2255.47	0.151	0.39
09BTDD007	378	378.1	2196.09	0.377	2255.49	0.154	0.41
09BTDD007	358	358.1	2195.72	0.35	2255.72	0.138	0.39
09BTDD007	368	368.1	2196.73	0.0925	2255.98	0.0872	0.94
09BTDD007	348	348.1	2194.46	0.0946	null	0.0858	0.91
09BTDD007	354	354.1	2195.88	0.292	NULL	NULL	Null
09BTDD009	641.9	642	2195.43	0.34	2253.28	0.0756	0.22
09BTDD009	620	620.1	2195.54	0.296	2254.29	0.0994	0.34
09BTDD009	572	572.1	2196.78	0.315	2254.41	0.0665	0.21
09BTDD009	635	635.1	2194.14	0.435	2254.78	0.139	0.32
09BTDD009	630	630.1	2194	0.463	2254.88	0.187	0.4
09BTDD009	640	640.1	2194.1	0.308	2255.62	0.111	0.36
09BTDD009	580	580.1	2196.34	0.327	2255.77	0.0727	0.22
09BTDD009	618	618.1	2195.04	0.265	2259.45	0.0783	0.3
09BTDD009	574	574.1	2196.41	0.298	NULL	NULL	Null
09BTDD009	576	576.1	2196.02	0.32	NULL	NULL	Null
09BTDD009	578	578.1	2196	0.449	NULL	NULL	Null
09BTDD009	585	585.1	2196.44	0.442	NULL	NULL	Null
09BTDD009	590	590.1	2196.18	0.261	NULL	NULL	Null
09BTDD009	595	595.1	2196.55	0.211	NULL	NULL	Null
09BTDD009	600	600.1	2196.5	0.473	NULL	NULL	Null
09BTDD009	605	605.1	2195.77	0.47	NULL	NULL	Null
09BTDD009	610	610.1	2195.73	0.501	NULL	NULL	Null
09BTDD009	615	615.1	2195.12	0.292	NULL	NULL	Null
09BTDD009	625	625.1	2194.92	0.35	NULL	NULL	Null
09BTDD011	450	450.1	2195.54	0.248	2252.02	0.0594	0.24
09BTDD011	480	480.1	2196.15	0.341	2257.9	0.18	0.53
09BTDD011	446	446.1	2197.58	0.282	NULL	NULL	Null
09BTDD011	448	448.1	2196.43	0.128	NULL	NULL	Null
09BTDD011	452	452.1	2196.02	0.17	NULL	NULL	Null
09BTDD011	454	454.1	2196.07	0.232	NULL	NULL	Null
09BTDD011	456	456.1	2194.3	0.288	NULL	NULL	Null
09BTDD011	458	458.1	2194.62	0.171	NULL	NULL	Null

09BTDD011	460	460.1	2194.24	0.265	NULL	NULL	Null
09BTDD011	465	465.1	2195.44	0.257	NULL	NULL	Null
09BTDD011	470	470.1	2195.11	0.468	NULL	NULL	Null
09BTDD011	474	474.1	2195.56	0.398	NULL	NULL	Null
09BTDD011	485	485.1	2195.82	0.432	NULL	NULL	Null
09BTDD011	490	490.1	2196.73	0.316	NULL	NULL	Null
09BTDD011	495	495.1	2196.55	0.336	NULL	NULL	Null
09BTDD011	500	500.1	2195.48	0.442	NULL	NULL	Null
09BTDD011	504.9	505	2195.79	0.237	NULL	NULL	Null
09BTDD021	390	390.1	2195	0.375	2254.57	0.119	0.32
09BTDD021	392	392.1	2196.04	0.177	2251.72	0.0634	0.36
09BTDD021	394	394.1	2194.48	0.269	NULL	NULL	Null
09BTDD021	396	396.1	2196.4	0.305	2252.57	0.0802	0.26
09BTDD021	398	398.1	2194.5	0.481	NULL	NULL	Null
09BTDD021	400	400.1	2195.63	0.395	NULL	NULL	Null
09BTDD021	402	402.1	2194.88	0.404	NULL	NULL	Null
09BTDD021	404	404.1	2194.92	0.438	2254.21	0.0587	0.13
09BTDD021	406	406.1	2194.67	0.412	NULL	NULL	Null
09BTDD021	408	408.1	2195.29	0.425	NULL	NULL	Null
09BTDD021	409.9	410	2196.94	0.197	NULL	NULL	Null
09BTDD023	575	575.1	2196.82	0.203	2257.66	0.0548	0.27
09BTDD023	551	551.1	2198.22	0.0883	2258.4	0.124	1.4

Every reasonable effort has been made to acknowledge the owners of copyright material. I would be pleased to hear from any copyright owner who has been omitted or incorrectly acknowledged.